



**HAL**  
open science

# Enhancing the performance of a self-oscillating fluidic heat engine (SOFHE) through thermodynamic cycle and phase change characterization

Nooshin Karami

## ► To cite this version:

Nooshin Karami. Enhancing the performance of a self-oscillating fluidic heat engine (SOFHE) through thermodynamic cycle and phase change characterization. Engineering Sciences [physics]. Université de Sherbrooke, 2023. English. NNT : . tel-04545377

**HAL Id: tel-04545377**

**<https://hal.science/tel-04545377>**

Submitted on 13 Apr 2024

**HAL** is a multi-disciplinary open access archive for the deposit and dissemination of scientific research documents, whether they are published or not. The documents may come from teaching and research institutions in France or abroad, or from public or private research centers.

L'archive ouverte pluridisciplinaire **HAL**, est destinée au dépôt et à la diffusion de documents scientifiques de niveau recherche, publiés ou non, émanant des établissements d'enseignement et de recherche français ou étrangers, des laboratoires publics ou privés.

UNIVERSITÉ de SHERBROOKE

Faculté de génie

Département de génie mécanique

Amélioration des performances d'un moteur thermique à  
fluide auto-oscillant par la caractérisation du cycle  
thermodynamique et du changement de phase

Enhancing the Performance of a Self-Oscillating Fluidic Heat Engine  
(SOFHE) through Thermodynamic Cycle and Phase Change  
Characterization

Thèse de doctorat

Spécialité: génie mécanique

Nooshin Karami

Sherbrook (Québec) CANADA

October 2023



# JURY MEMBERS

Luc. G. Fréchette  
Supervisor

Julien Sylvestre  
Examiner

Leyla Amiri  
Examiner

Sauro Filippeschi  
Examiner



## RÉSUMÉ

L'objectif de cette thèse est de mieux comprendre les principes de fonctionnement d'un moteur thermique fluide auto-oscillant (SOFHE) récemment découvert, en caractérisant le cycle thermodynamique (diagramme P-V) et le changement de phase (évaporation-condensation). Le SOFHE est proposé pour la récolte d'énergie thermique, couplé à un transducteur électromécanique, pour alimenter des capteurs sans fil utilisés dans l'Internet des objets (IoT). Le SOFHE est une bulle de vapeur piégée par un bouchon liquide (agissant comme un piston) dans un tube de petit diamètre. Cette bulle de vapeur-bouchon liquide est mise en oscillation par une évaporation-condensation cyclique d'une film liquide mince formée par une fibre de mèche. La première démonstration expérimentale du SOFHE a montré une faible puissance électrique de  $1 \mu\text{W}$ . Cependant, on ne savait toujours pas comment le cycle thermodynamique inconnu de la SOFHE se comporte sous une charge et quelle densité de puissance mécanique la SOFHE peut générer. Pour répondre à cette question, le cycle thermodynamique et la densité de puissance de la SOFHE sont caractérisés expérimentalement pour la première fois sous une charge mécanique variable. La principale contribution de cette caractérisation est de fournir une base de référence pour l'adaptation de l'impédance qui est cruciale pour la conception d'une charge compatible pour la SOFHE. Il est également démontré que la densité de puissance mécanique de la SOFHE est de l'ordre de  $0.5 \text{ milliwatts/cm}^3$ , ce qui en fait une solution prometteuse pour l'alimentation d'une gamme de capteurs sans fil dont la puissance requise est de l'ordre de  $10\text{s microwatt}$ . Nous avons également étudié l'effet de la température de fonctionnement de la source de chaleur et de deux paramètres de conception, notamment la longueur de la fibre de mèche et la longueur du bouchon liquide, sur la puissance de la SOFHE. L'augmentation significative de la puissance en augmentant la longueur de la fibre a été la force motrice de la deuxième phase de notre étude dans laquelle nous avons caractérisé le profil de changement de phase complexe et inconnu (évaporation-condensation) de la SOFHE. Un nouveau dispositif a été conçu pour visualiser la variation du film mince autour de la fibre lorsque nous avons joué sur sa longueur à l'intérieur de la zone de vapeur. Les observations ont prouvé notre hypothèse de la formation de coins capillaires entre la fibre et la paroi interne du tube qui pompent le liquide du liquide vers la zone de vapeur. Cela conduit à la formation d'un film mince avec une très faible résistance thermique qui alimente l'évaporation. Le taux de variation de la masse de vapeur, appelé taux de changement de phase, est également mesuré. Il est démontré que pour maximiser l'amplitude de l'oscillation et, par conséquent, la puissance du SOFHE, l'amplitude du taux de changement de phase doit augmenter et être complètement déphasée par rapport à la position. Un nombre sans dimension est également proposé pour évaluer l'efficacité du profil du taux de changement de phase. Enfin, pour mieux contrôler le changement de phase, une nouvelle conception de la SOFHE est proposée et démontrée dans laquelle nous pouvons intégrer des structures de mèche sur mesure pour imiter l'effet de la fibre insérée. Le dispositif est un microcanal à section carrée avec des angles aigus et un chemin capillaire gravé sur la paroi inférieure qui est fabriqué par un procédé standard de microfabrication. Il est démontré que l'amplitude et, par conséquent, la puissance de la SOFHE augmente (multiplication par cinq de  $30 \text{ à } 150 \mu\text{w/cm}^3$ ) avec l'ajout d'un chemin capillaire. Cela ouvre une nouvelle voie vers l'ingénierie du changement de phase de la SOFHE en concevant différentes structures de mèche pour améliorer les performances de la SOFHE.

**Mots clés:** micromoteur thermique, auto-oscillation, récupérateur thermique, évaporation-condensation, capillaire, cycle thermodynamique, microfabrication

## ABSTRACT

The aim of this thesis is to better understand the working principles of a recently discovered self-oscillating fluidic heat engine (SOFHE) by characterizing the thermodynamic cycle (P-V diagram) and phase change (evaporation-condensation). The SOFHE is proposed for thermal energy harvesting, coupled with an electromechanical transducer, for powering wireless sensors used in the Internet of Things (IoT). The SOFHE is a vapor bubble trapped by a liquid plug (acting as a piston) in a small diameter tube. This vapor bubble-liquid plug is set in oscillations by a cyclic evaporation-condensation of a thin liquid film formed by a wicking fiber. The first experimental demonstration of the SOFHE showed a low electrical power of  $1 \mu\text{W}$ . However, it is still unclear how the unknown thermodynamic cycle of the SOFHE behaves under a load and how much mechanical power density the SOFHE can generate. To address this question, the thermodynamic cycle and power density of the SOFHE are experimentally characterized for the first time under a varying mechanical load. The main contribution of this characterization is to provide a baseline for impedance matching that is crucial for designing a compatible load for the SOFHE. It is also shown that the mechanical power density of the SOFHE is in the range of milliwatts/cm<sup>3</sup> (maximum  $0.5 \text{ mW/cm}^3$ ) which makes it a promising solution to power a range of wireless sensors with a power requirement of tens of microwatt. We also studied the effect of the operating heat source temperature and two design parameters, including the length of the wicking fiber and the length of the liquid plug on the power of SOFHE. The significant increase of the power by increasing the fiber length was the driving force behind the second phase of our study in which we characterized the complex and unknown phase change profile (evaporation-condensation) of the SOFHE. A new setup was designed to visualize the variation of the thin film around the fiber as we played with its length inside the vapor zone. The observations proved our hypothesis of forming capillary corners between the fiber and the inner wall of the tube that pumps liquid from the liquid plug toward the vapor zone. This leads to the formation of a thin film with a very small thermal resistance that feeds evaporation. The rate of change of mass of vapor, the so-called phase change rate, is also measured. It is shown that to maximize the amplitude of the oscillation and consequently the power of the SOFHE, the amplitude of the phase change rate should increase and be completely out of phase with the position. A dimensionless number is also proposed to evaluate the effectiveness of the phase change rate profile. Finally, to better control the phase change, a new design of the SOFHE is proposed in which we can integrate tailored wicking structures to mimic the effect of the inserted fiber. The device is a square cross-section microchannel with sharp corners as well as an etched capillary path on the bottom wall that is fabricated by a standard microfabrication process. It is shown that the amplitude and consequently the power of SOFHE increase (a fivefold increase from  $30$  to  $150 \mu\text{W/cm}^3$ ) as we add a capillary path. This opens a new path towards engineering the phase change of the SOFHE by designing different wicking structures to improve its performance.

**Keywords:** micro heat engine, self-oscillation, thermal harvester, evaporation-condensation, capillary, thermodynamic cycle, microfabrication



## ACKNOWLEDGEMENTS

I have completed an incredible PhD journey, which would have undoubtedly been impossible without the invaluable guidance and supervision of Prof. Fréchette. His profound knowledge, insightful feedback, and encouragement have been paramount in shaping the direction of my research. Prof. Fréchette's unique signature lies in fostering an environment of intellectual curiosity, which has made a profound and indispensable impact on both my academic and personal growth.

I would also like to express my gratitude to the esteemed members of the jury who dedicated their time and expertise to evaluate my PhD thesis. Their valuable insights, constructive feedback, and rigorous examination have undoubtedly enriched the quality of my research.

I would also like to extend my heartfelt thanks to my colleagues, Albert Tessier-Poirier and Étienne Léveillé whose collaboration and camaraderie have been invaluable throughout this endeavor. Their support, discussions, and constructive feedback have contributed significantly to the quality and depth of my work. I am also grateful to Amrid Amnache for his support that made my entry into the microfabrication world an incredibly smooth and enriching experience. Thanks also to Alihossein Nikkhah for his participation in our productive discussion.

Additionally, I extend my appreciation to the 3IT staff and LN2 members, whose expertise and assistance have been vital throughout my research journey. Their guidance and resources have facilitated the smooth progression of my studies.

Furthermore, I would like to express my gratitude to my friends, my parents, and my sisters for their encouragement and understanding. I would like to keep my last and special thanks to my best friend ever, my husband Hazhir, who has been a great source of motivation and inspiration throughout my PhD. Your unwavering support and faith in my abilities have meant everything to me. With you by my side, I know there are no limits to what I can accomplish.

Completing this PhD thesis has been an incredibly rewarding and transformative experience, and I am indebted to all those who have been part of this journey. Their contributions and support have been immeasurable, and I am truly fortunate to have had such exceptional individuals by my side.

# TABLE OF CONTENTS

1	Introduction .....	1
1.1.	Context.....	1
1.2.	Problem Statement and Objectives .....	3
1.3.	Thesis plan and original contributions.....	3
2	State-of-the-art.....	5
2.1	Thermoelectric generators .....	5
2.2	MEMS-based Micro heat engines.....	7
2.3	Pulsating heat pipes (PHP).....	10
2.4	Single-branch PHP (SB-PHP).....	11
2.4.1.	Start-up of oscillation .....	13
2.4.2.	Resonator .....	15
2.4.3.	Phasing between variables.....	16
2.4.4.	Saturation of oscillation amplitude.....	18
2.4.5.	Role of phase change .....	19
2.5	Thin film phase change.....	19
2.5.1.	How thin film forms in oscillatory flow.....	20
2.5.2.	Thin film evaporation fundamentals.....	20
2.5.3.	Phase change enhancement .....	21
2.6	Transducer.....	24
2.6.1.	Electromagnetic transducer .....	24
2.6.2.	Electrostatic transducer.....	25
2.6.3.	Piezoelectric transducer .....	26
2.7	Impedance matching .....	26
2.7.1	Influential parameters on impedance of the SOFHE.....	28
2.8	Conclusion .....	29
3	What is the potential of the SOFHE? .....	31
3.1	Introduction.....	33
3.2	Methodology .....	37
3.2.1	Experimental set-up.....	37
3.2.2	Experimental procedure.....	38
3.2.3	Analytical calculation procedure .....	38

3.3	Results.....	40
3.3.1	Thermodynamic cycle .....	40
3.3.2	Generated work and power density of SOFHE .....	42
3.3.3	Efficiency.....	43
3.3.4	Effect of operating and design parameters .....	44
3.4	Discussion .....	48
3.5	Conclusion .....	49
4	How phase-change mechanism affects the SOFHE performance?.....	52
4.1	Introduction.....	54
4.2	Methodology .....	55
4.2.1	Experimental set-up.....	55
4.3	Results.....	57
4.3.1	Thin film phase change: beating oscillations .....	57
4.3.2	Modified phase change by wicking fiber: a method for stable oscillations .....	59
4.3.3	Phase change profile.....	61
4.4	Discussion .....	62
4.4.1	Phase change force and work .....	62
4.4.2	Ideal phasing.....	63
4.4.3	Effectiveness of phase change .....	64
4.5	Conclusion .....	66
5	How to improve design of the SOFHE? .....	68
5.1	Introduction.....	69
5.2	Methodology .....	72
5.2.1	Device.....	72
5.2.2	Test setup.....	74
5.2.3	Test procedure .....	74
5.3	Results.....	75
5.4	Discussion .....	79
5.6	Conclusion .....	82
6	Discussion .....	84
6.1	SOFHE vs TEGs and micro heat engines .....	84
6.2	How to design a better SOFHE.....	85
6.3	Potential of the SOFHE for electrical power generation .....	86
6.4	Impedance matching: coupling SOFHE .....	88

6.5	Miniaturization of the SOFHE.....	89
6.6	SOFHE for pumping application.....	90
7	Conclusion.....	92
7.1.	Contributions.....	92
7.2.	Deliverables.....	93
7.3.	Other scientific contributions.....	94
7.4.	Future research.....	94
8	Conclusion française.....	97
8.1.	Contributions.....	97
8.2.	Deliverables.....	99
8.3.	Autres contributions scientifiques.....	99
8.4.	Recherches futures.....	99
	Appendix A.....	102
	A. Details on the role of the wicking fiber.....	102
	A.1. Amplitude of the phase change rate.....	102
	A.2. Oscillation amplitude.....	103
	A.3. Phasing of the phase change rate.....	103
	Appendix B.....	105
	B. Effect of phasing on SOFHE efficiency.....	105
	Appendix C.....	106
	C. Effect of the adiabatic distance on phase change.....	106
	Appendix D.....	107
	D. Effect of vapor length.....	107
	D.1. Experiments.....	107
	D.2. Results.....	107
	D.2.1. Amplitude and Frequency.....	107
	D.2.2. Net Evaporation Rate.....	108
	D.2.3. Work and power.....	108
	References.....	111

## LIST OF FIGURES

Figure 1-1 Ambient sources' power densities before conversion [2].....	1
Figure 1-2 application of the SOFHE as a thermal energy harvester to power sensors when coupled to an electromechanical transduce [2].....	2
Figure 1-3 The first demonstration of the SOFHE coupled with a piezoelectric membrane [4].	3
Figure 2-1 Generation of electric current by a TEG module exposed to a thermal gradient [5].	6
Figure 2-2 Figure-of-merit ( $zT$ ) of commercial or state-of-the art material developed by NASA for thermal energy harvesting [5]. .....	6
Figure 2-3 Schematic of the $P^3$ microcapillary driven heat engine enhanced with thermal switch and added mass on the expander membrane [15]. .....	7
Figure 2-4 the wicking structure integrated to the evaporator membrane in $P^3$ micro heat engine [9][10] to pump liquid into the evaporator. ....	8
Figure 2-5 Thermodynamic cycle (P-V diagram) of the $P^3$ micro heat engine at resonance [15]. .....	8
Figure 2-6 The cross-section view of the phase change based micro heat engine developed by IMTEK research group during expansion (left) and compression (right) [17]. ....	9
Figure 2-7 Idealized thermodynamic cycle (pressure versus volume diagram) of the cavity micro heat engine developed by IMTEK [17]. .....	9
Figure 2-8 Different conversion steps of thermal energy into electrical by a bimetallic micro heat engine coupled with a piezoelectric membrane [26]. ....	10
Figure 2-9 Schematic of the bimetallic heat engine during heating (a) and (b) cooling [29]. ..	10
Figure 2-10 Schematic of a pulsating heat pipe in contact with heat source (evaporator) and a heat sink (condenser) with the vapor bubbles and liquid plugs distributed over the length [38]. .....	11
Figure 2-11 Schematic illustration of a complete cycle of oscillation in a single-branch PHP.	12
Figure 2-12 (a) The defined control volumes, and (b) the applied forces on the liquid plug in the model by Tessier-Poirier [48]. Figure is reproduced with the authorization of APS. ....	13
Figure 2-13 (a) The wall axial temperature profile and (b) the thermal resistance model to represent the phase change model proposed by Tessier-Poirier [48]. Figure is reproduced with the authorization of APS. ....	14
Figure 2-14 The equilibrium state of SBPHP system modeled by Tessier-Poirier [48]: for $II < 1$ the system is stable (friction is greater than phase change) while for $II > 1$ the system is unstable and any perturbations leads to oscillations. Figure is reproduced with the authorization of APS. ....	15
Figure 2-15 The evolution of variables and their phasor representation over a cycle in the system modeled by Tessier-Poirier [48]: a) meniscus position and velocity, b) forces from change of pressure (spring force opposite to position and feedback force in phase with velocity), c) the phase change rate that is opposite to position generating a force that is in phase with velocity. Figure is reproduced with the authorization of APS. ....	17
Figure 2-16 The evolution of the variables measured experimentally by Tessier-Poirier [48] during the startup: the dotted lines in the phasor graphs represent the position and velocity. Figure is reproduced with the authorization of APS. ....	18
Figure 2-17 The experimental measurement of the oscillation amplitude during startup in the SBPHP studied by Tessier-Poirier [59]. .....	19

Figure 2-18 The sources that introduces nonlinearities to the system (SBPHP) studied by Tessier-Poirier [59]: a) nonlinear wall temperature profile that leads to a nonlinear phase change profile, b) the pressure of the gas defined by ideal gas law. ....	19
Figure 2-19 Different regions in the evaporator of the SBPHP forming due to receding of the liquid plug studied by Fourgeaud [44]. ....	20
Figure 2-20 Schematic of different regions in thin film evaporation [63]. ....	21
Figure 2-21 Cross-sectional view of surface pillars (a) liquid wicking and evaporation, (b) heat flow from the walls to the liquid-vapor interface [75]. ....	22
Figure 2-22 Schematic view of the microfabrication process for microstructures to improve thin film evaporation. ....	23
Figure 2-23 Schematic of the capillary pumped liquid through corners of a square cross-sectional capillary tube [81]. ....	23
Figure 2-24 SEM images of the local cross-section (top) and inner surfaces (bottom) of the micro-grooved tube to improve PHP performance [82]. ....	24
Figure 2-25 The ultra-sharp corner added to the PHP (top) and the SEM images of the grooved profile (bottom) [83]. ....	24
Figure 2-26 Piezoelectric spiral membrane attached to the SOFHE [4]. ....	26
Figure 2-27 Schematic of the transduction mechanisms involved in our thermal energy harvester .....	27
Figure 3-1 SOFHE application, harvesting waste heat to power wireless sensors. ....	35
Figure 3-2 Schematic view of SOFHE operating cycle (left) and the corresponding Sankey diagram (right). ....	36
Figure 3-3 Schematic of SOFHE experimental set-up for cycle characterization [109]. ....	38
Figure 3-4 Measured P-V cycle of SOFHE: a) without load, b) under different loads at $T_H=110$ °C and fiber length at 4.5 cm. ....	41
Figure 3-5 Phase comparison between the measured position, velocity and pressure change with and without the load at $T_H=110$ °C. ....	42
Figure 3-6 Measured $W_{friction}$ and $W_{net}$ (stacked area), along with the available mechanical power density (line graph) under different amounts of load at $T_H=110$ °C. ....	43
Figure 3-7 P-V cycle of SOFHE at different heat source temperatures $T_H$ without load. ....	44
Figure 3-8 Available mechanical power density (volume= 3 cm <sup>3</sup> ) as a function of the load coefficient at different $T_H$ and loads. Dashed curves are fits to the data using the Tessier-Poirier et al. [112] model. ....	45
Figure 3-9 P-V cycles at different fiber lengths inside the evaporator ( $L_{fiber}$ ) at $T_H=110$ °C at a fixed load. The phase change rate corresponding to each cycle as a function of time is shown in the insert. ....	46
Figure 3-10 Work (friction and net) and power density at different fiber lengths inside the evaporator ( $L_{fiber}$ ) under a fixed load at $T_H=110$ °C. ....	47
Figure 3-11 Schematic view of the inserted fiber acting as a wicking structure inside the evaporator. ....	47
Figure 3-12 The measured thermodynamic cycle of the SOFHE showing evaporation and condensation processes (left) and the corresponding phase diagram (right): measured phasing (top) and ideal phasing for maximum $W_{net}$ (bottom). ....	49
Figure 4-1 PHP's application to cool a hot surface and its equivalent Sankey diagram (left), SOFHE's application as a thermal energy harvester and its Sankey diagram (right) [120]. ....	54
Figure 4-2 The test setup to measure phase change rate (evaporation-condensation) in a	

thermally self-induced oscillatory flow inside a capillary tube: a) exploded view, b) real top view. ....	57
Figure 4-3 Meniscus displacement and phase change rate for water showing periodic oscillations resulting from dryout of the thin liquid film left behind the meniscus.....	58
Figure 4-4 The measured pressure at two different evaporator temperatures, with a magnified inset showing higher pressure amplitude at lower temperature resulting from longer depth of meniscus penetration inside the evaporator.....	59
Figure 4-5 A frame of the recorded video during oscillations presenting: a) top view of the vapor, liquid, oscillating meniscus, fiber, and the thin film b) magnification of the thin liquid film around the fiber (the zone specified with white dashed lines) c) the cross-section schematic of the thin film formed by capillary action through the corners between the inner wall of the glass tube and the fiber.....	59
Figure 4-6 Meniscus displacement and phase change rate as a function of time in the presence of the wicking fiber for a) water b) ethanol.....	60
Figure 4-7 The phase change profile (evaporation-condensation rate as a function of displacement) with an inset indicating the corresponding cycles for beating oscillations with water. ....	61
Figure 4-8 The phase change profile in the presence of the fiber for water and ethanol. The gray bands represent the measurement uncertainty. ....	62
Figure 4-9 Applied forces on the liquid plug. ....	62
Figure 4-10 The velocity and phase change force (top) and their product (bottom) as a function of time with a,b) for the real phase angle, and c,d) for the ideal phase. Water in the presence of the fiber. ....	64
Figure 4-11 The velocity and phase change force (a) and their product (b) as a function of time showing an ideal phase angle between phase change force and the velocity. Ethanol in the presence of the fiber.....	64
Figure 4-12 The phase change effectiveness, $\phi$ , as a function of phase shift between the phase change force and the velocity for water and ethanol. An ideal phase corresponds to $\phi = 1$ . ....	65
Figure 5-1 SOFHE application, harvesting waste heat to power wireless sensors [116]. ....	70
Figure 5-2 The complete expansion-compression cycle of the vapor bubble for producing work (real cycle) [116]. ....	71
Figure 5-3 Cross-section of the microfabricated channel using anodic bonding of Si and grooved glass wafers, shown from the open end. The dashed line is the representative of the etched capillary trench included in some configurations [116].....	73
Figure 5-4 Microfabrication process flow. ....	73
Figure 5-5 The experimental test rig to measure the oscillation amplitude and to visualize the oscillating meniscus a) schematic exploded view, b) real setup with the device on top [116].....	75
Figure 5-6 a) 2-D top view recorded by high-speed camera showing the oscillating meniscus that leaves a thin film behind (the shadow covering the top wall) as well as the wicked liquid through corner capillaries (the dark edges ending with triple points) [116], b) 3-D schematic to better show the lines of triple points that have main contribution to the evaporation due to their low thermal resistance. ....	76
Figure 5-7 Meniscus displacement as a function of time at evaporator temperature of 120 °C for the device without an etched capillary path [116] ....	77
Figure 5-8 Meniscus displacement as a function of time at four different evaporator temperatures	

for the device without an etched capillary path [116].	77
Figure 5-9 Increase of the oscillation amplitude because of amplifying wicking action by adding an etched capillary path on the bottom wall with the depth of 100 $\mu\text{m}$ at two different widths of 25 $\mu\text{m}$ and 50 $\mu\text{m}$ at evaporator temperature of 150 $^{\circ}\text{C}$ .	78
Figure 5-10 The forces applied on the liquid plug.	79
Figure 5-11 The applied forces on the liquid plug, including friction, inertia, and pressure force as a function of time for the device with no etched capillary path at evaporator temperature 120 $^{\circ}\text{C}$ .	80
Figure 5-12 Thermodynamic (P-V) cycle of micro SOFHE at four different evaporator temperatures.	81
Figure 5-13 The normalized power as a function of evaporator temperature at micro and mesoscale SOFHE showing an increasing trend for both.	81
Figure 6-1 The second law efficiency of TEGs (theoretical) at different effective figure-of-merit ( $zT$ ) compared to that of the SOFHE (experimental).	85
Figure 6-2 Two different shapes of coils moving towards a constant magnetic field [134].	86
Figure 6-3 Electrical representation of the electromagnetic transducer [134].	87
Figure 6-4 Electrical power as a function of the electromagnetic transduction factor ( $k_t=NBl$ ) calculated by matching the real impedance of the SOFHE with an idealized electromagnetic transducer.	88
Figure 6-5 Cross-section view of the proposed ejector for the SOFHE for pumping application.	90

## LIST OF TABLES

Table 2-1 Comparison of power density by published electromagnetic vibration driven harvesters .....	25
Table 2-2 Comparison of power density for electret-free electrostatic vibration driven harvesters .....	26
Table 2-3 Electrical equivalent of mechanical component .....	27
Table 2-4 Influential parameters on mechanical impedance of the SOFHE and the transducer .....	28
Table 3-1 Amplitude and phase change rate at different heat source temperatures $T_H$ .....	44
Table 3-2 Maximum power density at different heat source temperatures $T_H$ .....	45
Table 3-3 Comparison of cycle work, friction loss, and net work at two different lengths of the liquid plug .....	48
Table 5-1 The power, and power density of the three tested microscale SOFHEs and the mesoscale SOFHE showing an increase by adding a capillary path. ....	82
Table 6-1 Comparison of mechanical power density of the SOFHE with the literature .....	85
Table 6-2 Summarized effects of the parameters on the SOFHE performance to be used as a baseline for impedance matching. ....	89

# Chapter 1

## Introduction

### 1.1. Context

We are living in a constantly changing world evolving towards making everyday devices smart enough to interact and communicate with each other through the internet that is called Internet of Thing (IoT). By 2025, about 22 billion IoT devices will be connected to the Internet. We are making significant progress in such a field thanks to the presence of wireless sensors that facilitates interacting with our surroundings even from distance. As the number of IoT devices proliferate, so does the number of batteries to power their sensors. Despite the ease of use and cost-effectiveness of batteries, they have major drawbacks that are the need of replacement and disposal. Besides, certain applications cannot rely on batteries as the sole source of power, including industrial sensors continually operating in harsh environments such as turbine, blast furnaces, roasting operations, distillation columns, evaporation chambers. To tackle this issue, researchers have been attracted to utilizing self-power systems like energy harvesters that recycle ambient energy and continually replenish the energy consumed by the system [1]. We can benefit from a variety of ambient energy sources with different power densities as shown in Figure 1-1. These ambient energy sources can be used either as a direct replacement or to augment the battery.

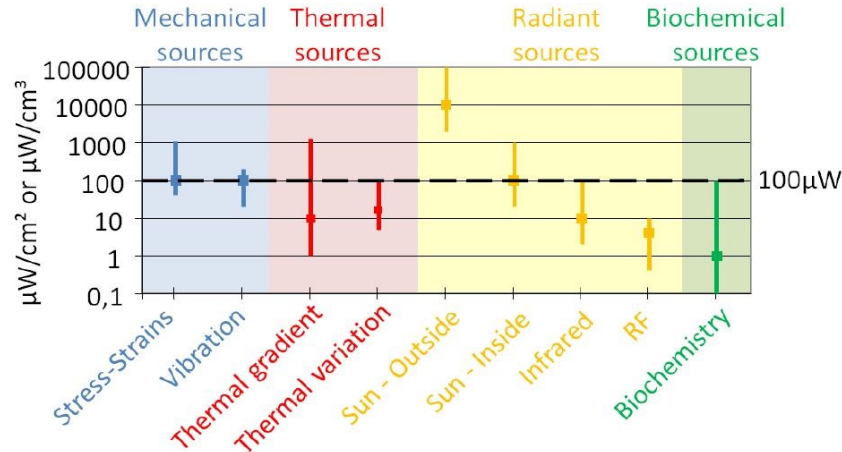


Figure 1-1 Ambient sources' power densities before conversion [2].

The power consumption of typical sensor nodes used in the Internet of Things can vary depending on the specific application and functionality. However, sensor nodes in IoT applications are generally designed to operate with low power consumption to maximize battery life and enable long-term deployment. On average, typical sensor nodes used in IoT applications consume power in the range of microwatts ( $\mu\text{W}$ ) to milliwatts ( $\text{mW}$ ). The power consumption is typically optimized through various techniques such as power management, duty cycling, and efficient communication protocols. These nodes are often designed to operate in a low-power sleep state when not actively sensing or transmitting data, reducing power consumption during idle periods. To evaluate the potential of harvesting energy from different ambient sources, a

typical sensor node's power consumption can be reviewed as follows [2]:

- 1-5  $\mu\text{W}$ : standby mode of power consumption
- 500  $\mu\text{W}$ : active mode of power consumption
- 50 mW: transmission power peak
- 50-500  $\mu\text{W}$ : the total amount of energy needed to perform a complete measurement and its wireless transmission

Therefore, an energy harvester has to be capable of generating at least 5  $\mu\text{W}$  to compensate the standby mode's energy consumption plus some more (50-500  $\mu\text{J}$ ) to be stored and used for the following measurement cycle. As shown in Figure 1-1, thermal gradient offers a wide range of power density that makes it a good source for harvesting. Thermoelectric generators (TEGs), which convert thermal energy into electricity based on Seebeck effect, are successfully utilized in wireless sensors [3]. A new type of thermal energy harvesters have emerged that are micro-electro-mechanical systems MEMS-based heat engines coupled with an electromechanical transducer. The focus of this research is on a newly discovered thermal energy harvester that is based on a Self-Oscillating Fluidic micro Heat Engine (SOFHE). Figure 1-2 shows a schematic of the SOFHE coupled to an electromechanical transducer proposed to power a wireless sensor. As shown, the SOFHE is a vapor bubble trapped by an oscillating liquid plug (acting as a piston) in a millimeter or micrometer channel. The vapor bubble-liquid plug is set in motion through the evaporation-condensation of a thin film in the vapor bubble. By doing so, the SOFHE converts thermal energy into mechanical energy through oscillations. This mechanical energy is then converted into electrical energy by coupling the SOFHE with an electromechanical transducer that can be a capacitor, a magnet-coil system, or a piezoelectric membrane. The first demonstration of the SOFHE (Figure 1-3), which was a millimeter-scale glass tube, coupled with a piezoelectric spiral membrane [4] generated power of 1  $\mu\text{W}$ . However, it was not clear if the low reported power is due to the poor performance of the SOFHE, the inefficient transducer architecture, or the weak coupling between the two. This arises the need for a component level study that is carried hereby on the SOFHE itself.

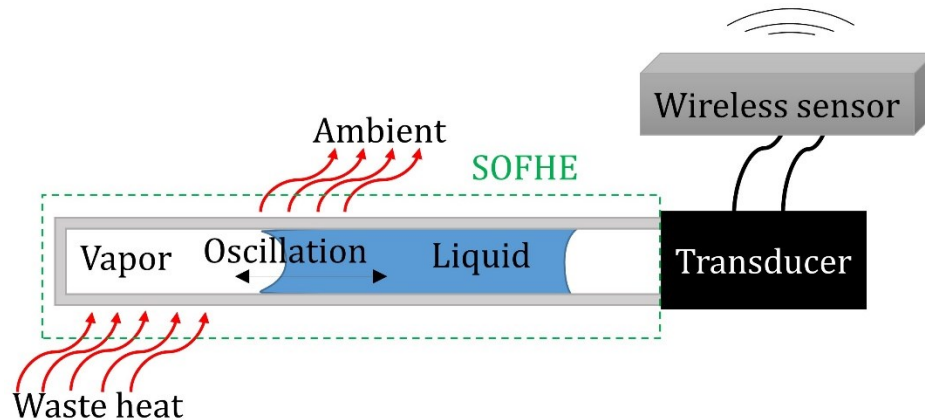


Figure 1-2 application of the SOFHE as a thermal energy harvester to power sensors when coupled to an electromechanical transduce [2].

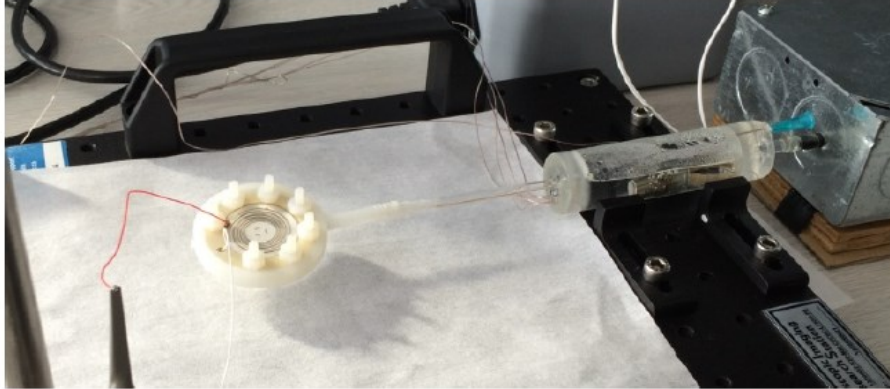


Figure 1-3 The first demonstration of the SOFHE coupled with a piezoelectric membrane [4].

## 1.2. Problem Statement and Objectives

The primary objective of this thesis is to enhance the design of the SOFHE by comprehending its behavior under varying load conditions. In addition, we seek to explore the potential of the SOFHE and investigate how different operating and design parameters influence its performance. This analysis will establish a foundation for optimizing the impedance matching between the SOFHE and the transducer, thereby maximizing power transfer efficiency. To fulfill these objectives, we must address the following key research questions:

- What is the potential of the SOFHE?
- How does power of the SOFHE vary as we start harvesting energy from it?
- How do design and operating parameters affect the SOFHE power?
- How to improve the design of the SOFHE?

## 1.3. Thesis plan and original contributions

The thesis plan is based on articles. Initially, the state-of-the-art (chapter 2) discusses various existing methods for harnessing low-grade thermal energy. This analysis serves as a foundation for comparing the efficacy of the SOFHE once we address the primary research question (mentioned in section 2.1) in chapter 3. A thorough discussion of this comparison, design enhancements, and potential for pumping applications is also presented in chapter 6.

Continuing with the state-of-the-art, an analytical model is developed to gain a deeper understanding of the underlying physics governing the SOFHE. This model forms the basis for our analytical calculations throughout the thesis. While the model provides qualitative insights into the dynamics of the SOFHE, it falls short in quantifying its behavior due to an inadequate representation of the phase change (evaporation-condensation) occurring in the SOFHE. To overcome this limitation, an experimental approach, complemented by analytical analysis, is employed in chapter 4 to better describe the effectiveness of the phase change and quantify its impact on the SOFHE's performance.

Furthermore, the state-of-the-art section highlights various approaches aimed at enhancing the phase change through tailored microstructures. These approaches lay the groundwork for the development of our novel design for the SOFHE, which is elaborated upon in chapter 5.

Chapter 3, 4, and 5 comprise my research efforts in addressing the research questions outlined in section 1.2. The findings from these chapters, which have been published or submitted to scientific journals, are summarized below.

**Chapter 3. What is the potential of the SOFHE? How do the thermodynamic cycle and power of the SOFHE behave under load? How do the design and operating parameters affect SOFHE power?** This chapter focuses on the decoupling of the SOFHE from the transducer by introducing a variable mechanical load. The experimental characterization of the SOFHE thermodynamic cycle, work, and mechanical power density is conducted with respect to the load coefficient. Furthermore, the impact of specific operating and design parameters, such as the evaporator temperature, length of the liquid plug, and phase change mechanism, on the power output of the SOFHE is thoroughly investigated. Notably, the findings resulting from this research have been published in the peer-reviewed journal of “*Energy Conversion and Management*”.

**Chapter 4. How does the phase-change mechanism affect the SOFHE performance?** In this chapter, our focus centers on investigating the intricate mechanism of the phase change within the SOFHE. Through experimentation, we measure and analyze the phase change profile. To evaluate the efficiency of the phase change mechanism, we introduce a novel approach that investigate the phasing between the force from the phase change and the velocity by proposing a dimensionless number. This method enables us to quantitatively assess the effectiveness of the phase change process. The findings from this research endeavor have been published in a highly esteemed, peer-reviewed journal titled: “*International Journal of Heat and Mass transfer*”.

**Chapter 5. How to control the phase change to optimize the SOFHE performance?** In this chapter, we embark on the design, fabrication, and characterization of a phase change enhanced SOFHE using capillary wicking. This innovative approach allows for an improved performance of the device, ensuring its reliable operation. The thorough analysis and evaluation of the device's performance yield promising results. These findings have been submitted to a prestigious publication for consideration to “*Journal of Micromechanics and Microengineering*”. It has been accepted for publication with minor revision.

# Chapter 2

## State-of-the-art

This chapter focuses on available approaches for harvesting low-grade thermal energy, including thermoelectric generators (2.1), micro heat engines (2.2), and pulsating heat pipes (PHP) (2.3). This discussion provides a basis for understanding the current state of the field and serves as a reference point for comparing the SOFHE effectiveness in energy harvesting.

Following that, Single branch pulsating heat pipes (SB-PHP) are introduced in section (2.4) showcasing their similarities with the SOFHE in underlying physics and highlighting the key distinctions that set them apart. This section delves into an analytical model that aims to better comprehend the physics underlying the SOFHE, including the startup mechanism, the existence of the resonator, saturation of the amplitude, and finally the role of the phase change (evaporation-condensation). This model forms the basis for analytical calculations throughout the thesis. However, it is acknowledged that the current model falls short in quantifying the behavior of the SOFHE accurately, particularly regarding the phase change (evaporation-condensation) process. This limitation prompts the need for an experimental approach to complement the analytical analysis and provide a more comprehensive understanding of the phase change dynamics and its impact on the SOFHE performance.

Additionally, the state-of-the-art chapter explores different approaches to augment the phase change process through tailored microstructures. These approaches are crucial in informing the development of a new design for the SOFHE, aiming to optimize its performance.

Overall, this chapter sets the stage for the subsequent chapters of the thesis, providing the necessary background and knowledge to address the research questions and advance the understanding and design of the SOFHE.

### 2.1 Thermoelectric generators

Thermoelectric Generators (TEGs) are the well-known solid-state thermal energy harvesters that work based on Seebeck effect. TEGs are composed of two semiconductor bars doped with n and p carriers. Exposing this structure to a thermal gradient leads to the generation of an electric current (Figure 2-1). The maximum efficiency of TEGs working between a heat sink ( $T_C$ ) and a heat source ( $T_H$ ) is defined as [5]:

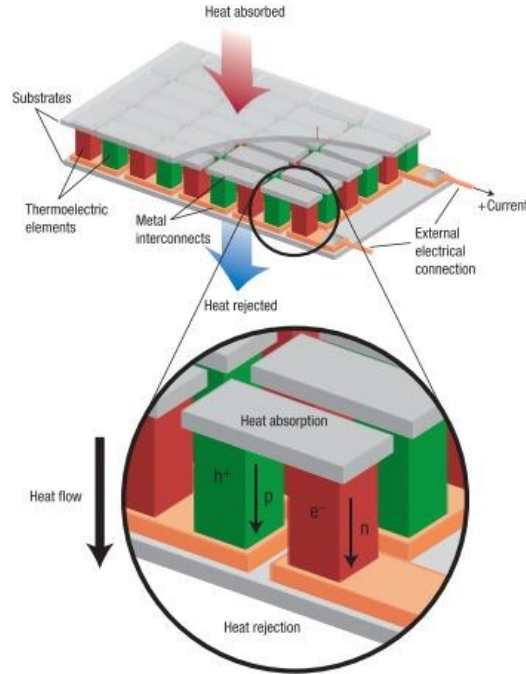


Figure 2-1 Generation of electric current by a TEG module exposed to a thermal gradient [5].

$$\eta = \frac{\Delta T}{T_H} \times \frac{\sqrt{1 + ZT} - 1}{\sqrt{1 + ZT} + \frac{T_C}{T_H}} \quad (2-1)$$

The  $ZT$  parameter is the effective device figure-of-merit that combines the effect of thermal and electrical conductivity as well as the Seebeck coefficient. To optimize it, the figure of merit of the material ( $zT$ ) must be enhanced. This requires optimizing conflicting properties: high electrical conductivity and low thermal conductivity. Figure 2-2 shows  $zT$  of the state-of-the-art materials as a function of temperature that are complex alloyed with dopants. The maximum  $zT$  of the material suitable for low-grade thermal energy ( $T < 200^\circ\text{C}$ ) is 1 for bismuth telluride ( $\text{Bi}_2\text{Te}_3$ ) that is the common commercialized material for TEGs. However, the effective device figure of merit ( $ZT$ ) is lower as all the material properties are a function of temperature. For example, the effective device  $ZT$  for  $\text{Bi}_2\text{Te}_3$  is only 0.7.

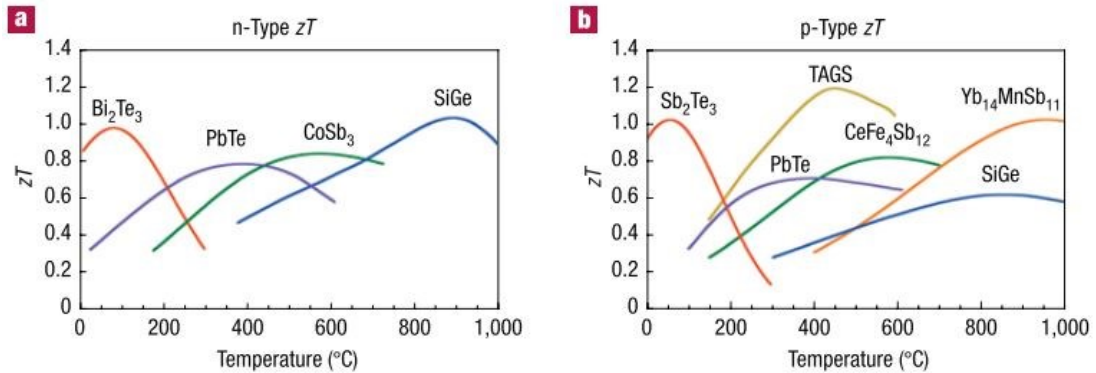


Figure 2-2 Figure-of-merit ( $zT$ ) of commercial or state-of-the art material developed by NASA for thermal energy harvesting [5].

Despite the design simplicity of TEGs, there are some disadvantages relating to them [6]:

- The good thermoelectric materials such as tellurium are rare and toxic.
- The available and safe materials like SiGe do not show high thermoelectric properties unless working at a very high temperature (Figure 2-2).
- Reducing thermal conductivity requires developing materials with complex chemical composition increasing the cost of production.
- Maintaining a sufficient thermal gradient over TEGs requires having a heat sink that increases the footprint of the device.

These inconveniences relating to TEGs encouraged researchers to look for more flexible and less expensive alternatives.

## 2.2 MEMS-based Micro heat engines

MEMS-based micro heat engines are fabricated through standard microfabrication process. There are examples of micro heat engines working based on phase change of a fluid. A micro heat engine named P<sup>3</sup> [7] [8], that is an external combustion engine, was first designed as a cavity bounded by thin membranes to seal in a saturated two-phase working fluid (Figure 2-3). The electric generator is a thin film piezoelectric integrated with the top membrane. The efficiency and operating speed of the engine is then improved by integrating microcapillary wicking structures [9][10] that continuously pump liquid to the heat addition zone (Figure 2-4). To maximize the power output and mechanical efficiency, a thermal switch [11][12][13] is integrated to the engine to control the heat transfer into and out of the engine. Finally, the engine is optimized in terms of the mass of the expander (top) membrane to decrease the resonant frequency (by adding mass as shown in Figure 2-3). This helped to operate the engine at resonant frequency that leads to increased power output [14].

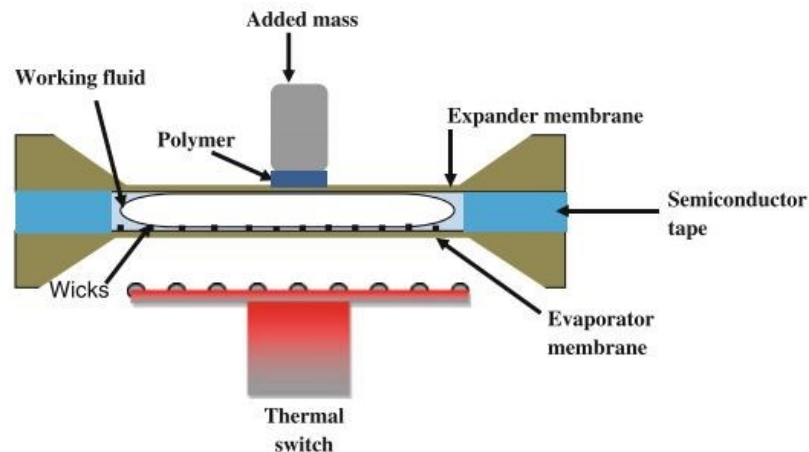


Figure 2-3 Schematic of the P<sup>3</sup> microcapillary driven heat engine enhanced with thermal switch and added mass on the expander membrane [15].

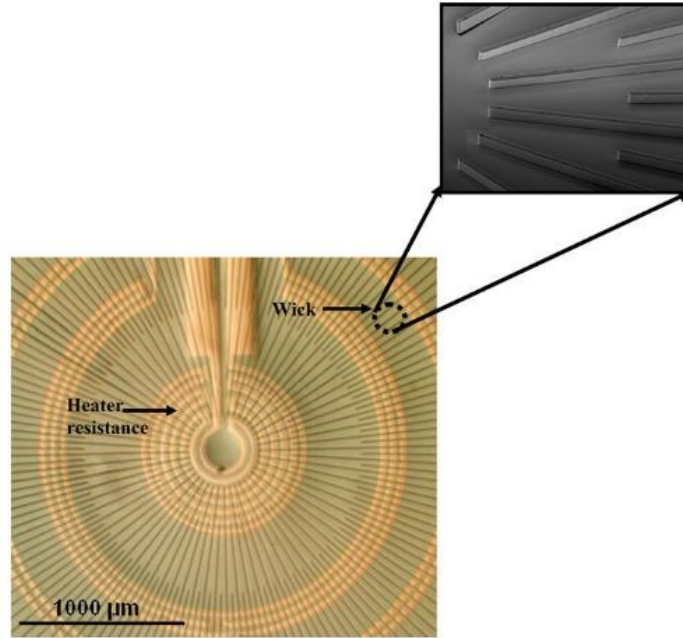


Figure 2-4 the wicking structure integrated to the evaporator membrane in P<sup>3</sup> micro heat engine [9][10] to pump liquid into the evaporator.

The thermodynamic cycle of the optimized engine (Figure 2-5) shows an approximation of the Carnot cycle (consisting of two constant temperature processes and two constant volume processes) [16][15]. This micro heat engine offers a mechanical power density of 10 mW cm<sup>-2</sup> with an operating temperature gradient of 30 K. The thermal to mechanical and the second law efficiency of the engine are 0.2% and 16%, respectively. The electrical peak power of 0.8 μW at a load resistance of 14 kΩ is achieved. The engine has a total volume of 0.6 mm<sup>3</sup>. A main drawback of this heat engine is the requirement of an external power supply and a pulse circuit to derive the engine.

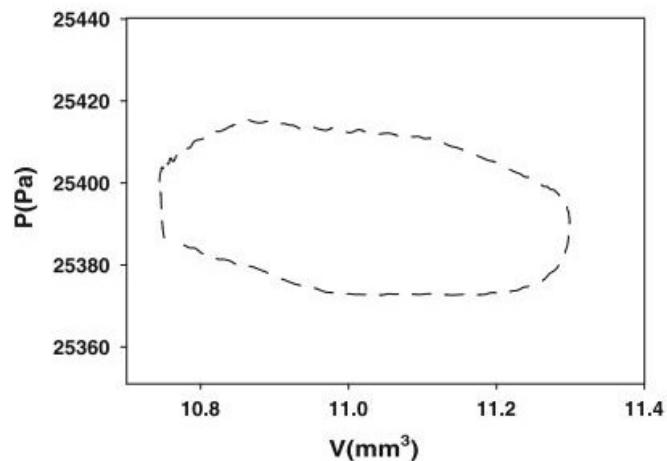


Figure 2-5 Thermodynamic cycle (P-V diagram) of the P<sup>3</sup> micro heat engine at resonance [15].

IMTEK research group developed a micro heat engine based on a cavity filled with a liquid-gas phase-change working fluid (Figure 2-6) that is coupled with a bistable buckling membrane

[17][18]. As shown in P-V diagram in Figure 2-7, the working fluid (HFE7100) expands (from 1 to 2) when the device is in contact with the heat source. This makes the membrane to deflect and snap into the heat sink where the heat is rejected (2-3) and the pressure inside the cavity drops. When the pressure is below a certain threshold the membrane will deflect downwards (3-4) and meet the heat source (4-1) and the cycle repeats. For a thermal gradient of 37 K, the reported mechanical power of the engine is  $1.29 \mu\text{W}$  with the thermodynamic cycle efficiency and second law efficiency of 0.3% and 1.7%, respectively. The size of the engine chamber is  $9 \times 9 \text{ mm}^2$ . The major drawback of this heat engine is the complex microfabrication process.

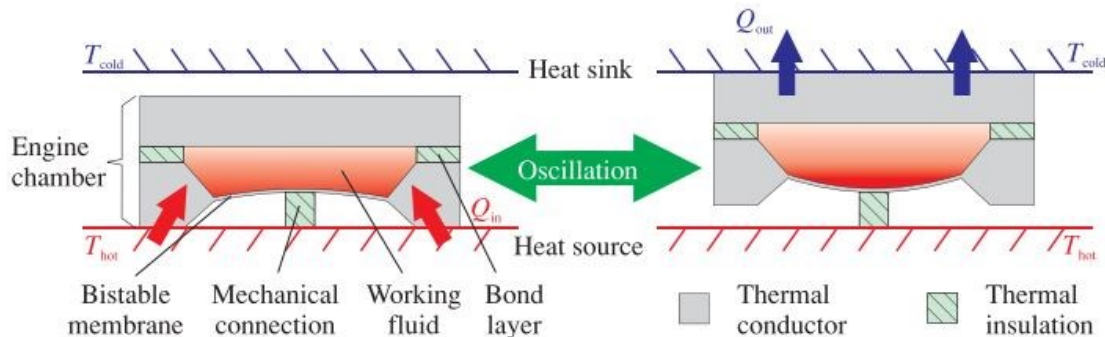


Figure 2-6 The cross-section view of the phase change based micro heat engine developed by IMTEK research group during expansion (left) and compression (right) [17].

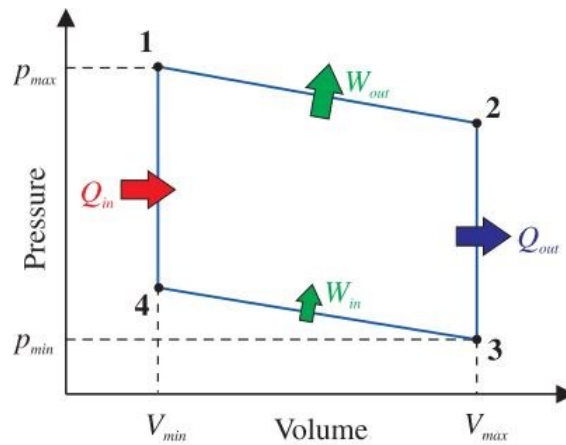


Figure 2-7 Idealized thermodynamic cycle (pressure versus volume diagram) of the cavity micro heat engine developed by IMTEK [17].

There are micro gas turbines [19–21] and micro steam turbines [22–24] that implement Brayton and Rankine thermodynamic cycle, respectively. They offer W-scale power, that is three orders of magnitude higher than the SOFHE, at 1–10% efficiency [25]. However, they have the complexity of requiring high-speed rotating parts. There are also examples of micro heat engines with no moving parts such as bimetallic strip heat engine (HEATec) [26][27][28]. The working principles of the bimetallic engine is shown in Figure 2-8. As can be seen, during the heating, the strip buckles owing to the mismatch of the thermal expansion coefficient of the bimet. This in turn deflects the piezoelectric membrane generating electricity. There is no working fluid in this micro heat engine. A mechanical power density of  $2.7 \text{ mW/cm}^2$  is reported for this micro heat engine. Coupled with the optimized piezoelectric generator, a maximum electrical power

of 10 nW is generated from a 60 K temperature difference (using ambient air as the cold temperature). Unlike TEGs, there is no need for a bulky heat sink in HEATec heat engine.

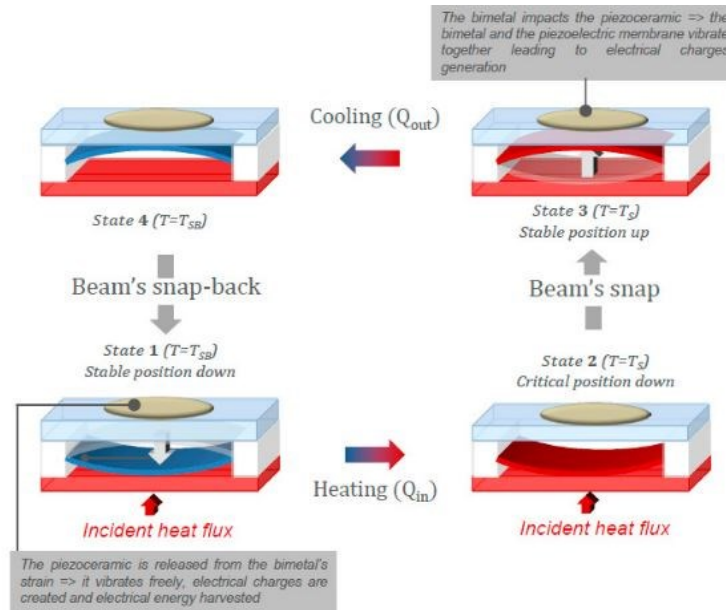


Figure 2-8 Different conversion steps of thermal energy into electrical by a bimetallic micro heat engine coupled with a piezoelectric membrane [26].

A variant of bimetallic heat engine (Figure 2-9) coupled with pyroelectric generators [29][30] is capable of generating 4.4  $\mu\text{W}$  electrical power from 96 K thermal gradient. This power is improved by an order of magnitude (40.4  $\mu\text{W}$ ) by coupling the engine with an electrostatic generator [31] at a temperature difference of 85 K.

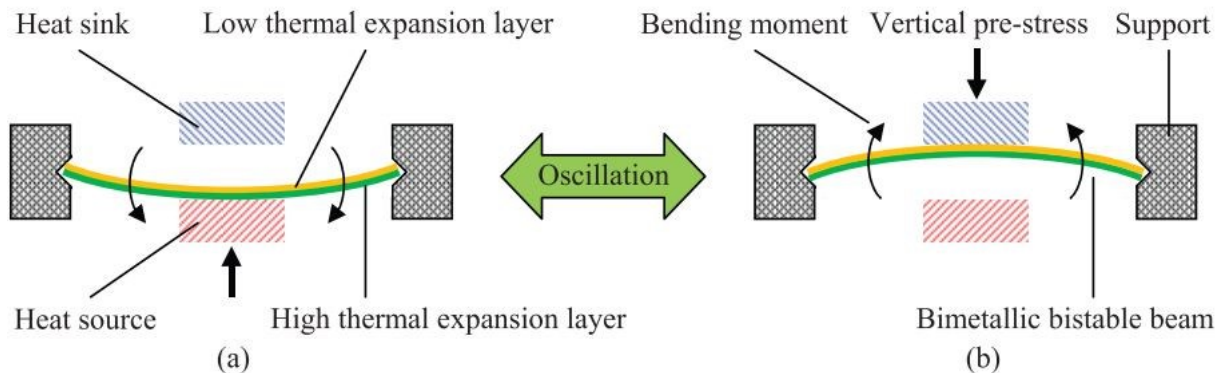


Figure 2-9 Schematic of the bimetallic heat engine during heating (a) and (b) cooling [29].

### 2.3 Pulsating heat pipes (PHP)

There were a couple of attempts in the literature on harvesting energy by PHPs with a primary application of heat transfer. They coupled PHPs with different types of transducers, including a piezoelectric membrane [32], solenoid with ferromagnetic working fluid [33] or magnet [34], electrical double layer junction [35], and pyroelectric transducer [36]. PHPs are meandering tubes (Figure 2-10) with a millimeter-scale inner diameter that have a heated zone (evaporator)

separated from a cooled zone (condenser) by a distance (adiabatic zone). Owing to capillarity, a slug-plug flow (also known as Taylor bubble flow) forms inside the tube in which the bubbles are separated from the liquid plugs with a meniscus. To form such a flow, capillary forces must be dominant compared to the gravity forces which leads to defining a critical value for the internal diameter ( $d_{cr}$ ) [37][38]:

$$d < d_{cr} = 2 \sqrt{\frac{\sigma}{g(\rho_l - \rho_v)}} \quad (2-2)$$

where  $\sigma$  is surface tension,  $\rho_l$  and  $\rho_v$  are the density of liquid and vapor, respectively. When the appropriate conditions are set (for example, temperature difference in the PHP exceeds a certain threshold) the vapor bubble-liquid plugs start to spontaneously move back and forth. These oscillations create a mechanical force than can be utilized to drive an electro-mechanical transducer. Despite the fact that PHPs have a simple design, they have complex operating principles. This makes it a challenge to model and predict the behavior of PHPs particularly their start-up and the amplitude of the oscillation. To better understand the underlying physics, Single-Branch PHPs are used in the literature [39–43] that are a simpler representative of the PHPs with only one vapor bubble and one liquid plug.

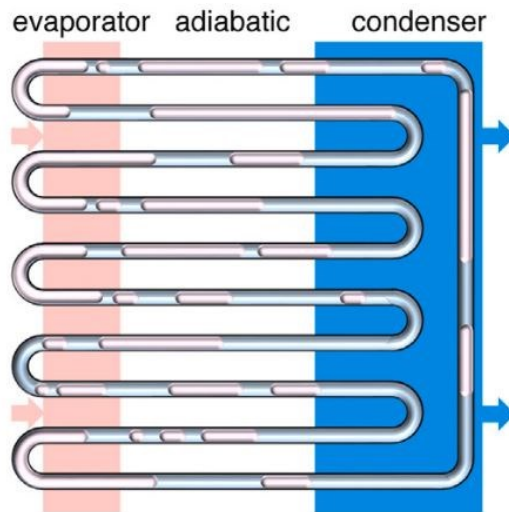


Figure 2-10 Schematic of a pulsating heat pipe in contact with heat source (evaporator) and a heat sink (condenser) with the vapor bubbles and liquid plugs distributed over the length [38].

## 2.4 Single-branch PHP (SB-PHP)

As shown in Figure 2-11, a single-branch pulsating heat pipe is a millimeter-scale tube filled with a working fluid that is heated from a closed end (evaporator) and cooled at the opposite end (condenser) separated by an adiabatic distance. As the temperature of the evaporator increases, a vapor bubble forms and grow lengthwise until it reaches an equilibrium point. Perturbing the equilibrium, for example increasing the temperature of the heat source or decreasing the external pressure, leads to oscillations. The vapor bubble expands and pressure rises until it reaches to the cold section where the bubble begins condensing due to the heat exchange with the cold wall. Then, the pressure in the liquid plug will be more than that of the vapor bubble and pushes the vapor back towards the evaporator part. As the vapor bubble

expands, the meniscus at the interface of the vapor bubble and the liquid plug extends to form a thin liquid film, which is believed to be responsible for the instability and sustaining the oscillations [39–43]. This thin film (with a very low thermal resistance) [44] makes the main contribution to the evaporation-condensation. SB-PHPs share similar physics with the SOFHE, but their applications differ. SB-PHPs focus on efficient heat transfer, primarily used for cooling purposes, while SOFHEs are designed for energy harvesting, achieving maximum work output with minimal heat transfer. This distinction is better explained with a Sankey diagram provided in Chapter 3, Figure 3.2.

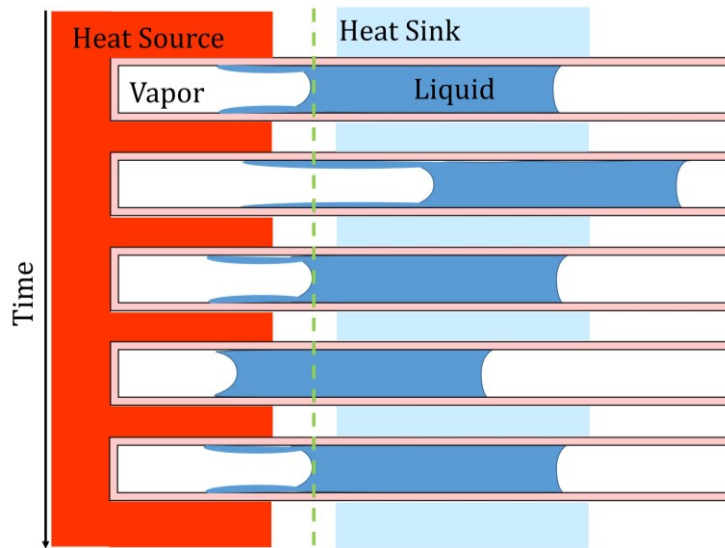


Figure 2-11 Schematic illustration of a complete cycle of oscillation in a single-branch PHP.

There are different approaches in the literature to explain this self-oscillation that are compared in a thesis by Tessier-Poirier [45]. We discuss a summary of the comparison hereby. The proposed models to predict the oscillatory behavior of SB-PHP revealed the existence of a spring (vapor bubble)-mass (liquid plug)-damper (friction) system [39,46–51]. These models, however, do not properly include the role of the thin film. The Film Evaporation-Condensation (FEC) model proposed by Das et al. [52], which is based on previous models by Dobson [50,51], and Zhang and Faghri [39], includes the phase change from the thin film for the variation of mass of vapor. However, the model for the phase change (step function for thermal gradient at the wall) made linearization impossible and thus an analytical solution and instability analysis of the system were not achieved. To address this issue, Nikolayev [53] carried out an analytical study of the FEC model using an averaging method. They also modified the model by considering axial heat conduction in the wall that yields a continuous wall temperature profile rather than step function [54]. An instability criterion was proposed which shows a minimum thermal gradient at equilibrium is required for the startup of oscillation. However, the piecewise model for the phase change made the instability analysis complicated since no classical linear stability analysis could be applied. The approach is discussed in details by Nikolayev and Marengo [55] and Nikolayev [38]. In a recent attempt by Tessier-Poirier et al. [48], a simplified continuous phase change model is proposed that allows linearization of the system and yields an analytical solution. Their model is highly valuable as it describes the instability mechanism and an analytical formula to predict startup is proposed. Their approach will be explained in more details in the followings.

### 2.4.1. Start-up of oscillation

Similar to previous approaches [39,52], the model starts with momentum balance on the liquid plug (Eqn. 2-3) and energy conservation on the vapor bubble (Eqn. 2-4) as shown in the model geometry in Figure 2-12 [48]:

$$\ddot{x}_i = \frac{1}{m_l} (P_g A - \hat{P}_e A - F_f) \quad (2-3)$$

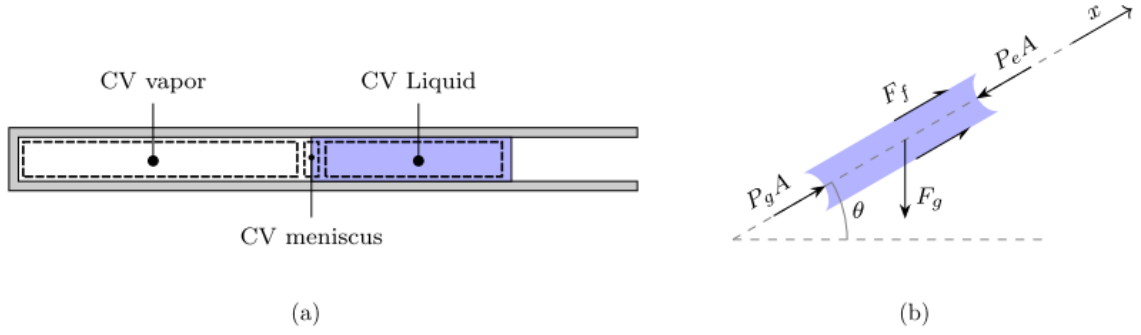


Figure 2-12 (a) The defined control volumes, and (b) the applied forces on the liquid plug in the model by Tessier-Poirier [48]. Figure is reproduced with the authorization of APS.

where  $x_i$  is the displacement of the meniscus with respect to the equilibrium,  $\dot{x}_i$ ,  $\ddot{x}_i$  are the velocity and the acceleration of the liquid plug, respectively,  $m_l$  is the liquid mass, and  $A$  is the surface perpendicular to the flow. The forces applied on the liquid plug are produced by the vapor pressure  $P_g$ , the external pressure  $\hat{P}_e$ , and the friction force  $F_f$  between the liquid plug and wall. The capillary forces on both meniscus are assumed to cancel out (to be opposite and equal).

For the energy balance in the vapor bubble, the energy from compression-expansion, the phase change, and the heat transfer from the wall ( $\dot{Q}_g$ ) are considered. The energy balance on the vapor bubble becomes [48]:

$$\dot{T}_g = \frac{1}{c_v m_g} [\dot{m}_g (c_p T_{g,sat} - c_v T_g) - P_g A \dot{x}_i + \dot{Q}_g] \quad (2-4)$$

where  $T_g$  is the average temperature of the vapor bubble,  $m_g$  is the mass of vapor and  $\dot{m}_g$  is the net evaporation rate. The saturation conditions is considered at the meniscus  $T_{g,sat}$ . The vapor pressure  $P_g$  in Eqn. (2-3) and (2-4) is defined by the ideal gas law [48]:

$$P_g = \frac{m_g R_g T_g}{V_g} = \frac{m_g R_g T_g}{(x_i + L_{g,0}) A} \quad (2-5)$$

with  $R_g$  the specific gas constant. Now, a phase change model is proposed to describe the change of mass of vapor due to evaporation-condensation. The phase change is defined as a thermal resistance model shown in Figure 2-13b. Therefore, the heat transfer rate ( $\dot{Q}$ ) that contributes to the net evaporation rate is defined using energy balance on the meniscus control volume [48]:

$$\dot{m}_g = \frac{\dot{Q}}{H_v} = \frac{T_w(x_i) - T_{g,sat}}{H_v R_{th}} \quad (2-6)$$

where  $T_w(x_i)$  is the wall temperature at the meniscus position that follows an arctangent profile (see Figure 2-13a),  $H_v$  is the vaporization enthalpy, and  $R_{th}$  is considered as the phase-change thermal resistance.

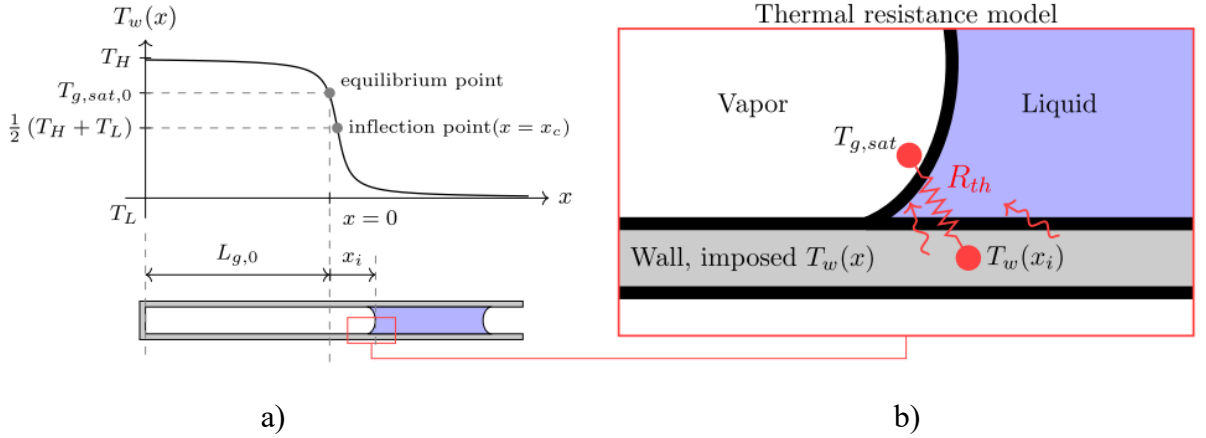


Figure 2-13 (a) The wall axial temperature profile and (b) the thermal resistance model to represent the phase change model proposed by Tessier-Poirier [48]. Figure is reproduced with the authorization of APS.

The remaining terms in Eqn. (2-3) is the friction force experienced by the liquid plug. The flow behavior is defined by the kinetic Reynolds number ( $Re_\omega \equiv \omega R^2/\nu$ ). In an oscillatory flow for  $Re_\omega \ll 4$ , the velocity profile can be estimated by a quasistatic Poiseuille flow:

$$F_f = -8\pi\mu_l L_l \dot{x}_i = c\dot{x}_i \quad (2-7a)$$

where  $\mu_l$  is the liquid viscosity. However, for laminar flow  $Re_\omega > 4$ , the flow deviates from a Poiseuille parabolic velocity profile. Tessier-Poirier et al. [48] derived an expression for the friction force from the velocity profile in a pulsatile flow given by White [56]:

$$F_f \approx -\sqrt{\frac{2}{Re_\omega}} \Delta P_g A + \left( \sqrt{\frac{2}{Re_\omega}} - \frac{1}{Re_\omega} \right) \frac{\Delta \dot{P}_g A}{\omega} \quad (2-7c)$$

Now variables are substituted with their change with respect to the equilibrium and then the set of equations are made dimensionless using the quantities at equilibrium (e.g.,  $\widetilde{\Delta P}_g = \Delta P_g/P_{g,0}$ ,  $\widetilde{x}_i = x_i/L_{g,0}$ ,  $\widetilde{\Delta m}_g = \Delta m_g/m_{g,0}$ ). By doing so, we reach nonlinear dimensionless differential equations as follows [48]:

$$\ddot{\widetilde{x}}_i = \widetilde{\Delta P}_g + \widetilde{F}_f = -\underbrace{\left( \frac{1}{1 + \widetilde{x}_i} \right)}_{\widetilde{F}_v} \widetilde{x}_i + \underbrace{\left( \frac{1}{1 + \widetilde{x}_i} \right)}_{\widetilde{F}_m} \widetilde{\Delta m}_g - \underbrace{2\zeta_f}_{\widetilde{F}_f} \dot{\widetilde{x}}_i \quad (2-8a)$$

$$\dot{\widetilde{m}}_g = \widetilde{T}_{HL} \arctan[-|\widetilde{T}'_{wc}|(\widetilde{x}_i - \widetilde{x}_c)] + \widetilde{C}_{th} \quad (2-8b)$$

The first two terms in the right side of the Eqn. (2-8a) are the force produced by the pressure change. The first term is the force due to the volume change  $F_v$  (in phase with position acting as a spring) and the second one is the force due to the phase change  $F_m$  (in phase with velocity acting as a negative damping). To perform an instability analysis, the system of equations are linearized as follows [48]:

$$\ddot{\widetilde{x}}_i \approx -\underbrace{\widetilde{x}_i}_{\widetilde{F}_v} + \underbrace{\widetilde{\Delta m}_g}_{\widetilde{F}_m} - \underbrace{2\zeta_f}_{\widetilde{F}_f} \dot{\widetilde{x}}_i \quad (2-9a)$$

$$\dot{\widetilde{m}}_g \approx 2\tilde{\sigma} \dot{\widetilde{x}}_i \quad (2-9b)$$

where  $\tilde{\sigma}$  represents the phase change coefficient. The linearized solution for position gives a

sinusoidal motion:

$$\bar{x}_l(\tau) = \underbrace{a_1 e^{\lambda_1 \tau}}_{\text{mean value growth}} + \underbrace{a_2 e^{\bar{\alpha} \tau} \sin(\bar{\omega} \tau + \varphi)}_{\text{oscillations}} \quad (2-10)$$

where the constants  $a_1$ ,  $a_2$ ,  $\varphi$  are calculated from initial conditions and the variables are approximated for small  $\bar{\sigma}$  and  $\zeta_f$  as follows [48]:

$$\bar{\alpha} \approx \bar{\sigma} - \zeta_f = \zeta_f(\Pi - 1) \quad (2-10a)$$

$$\Pi \equiv \frac{\bar{\sigma}}{\zeta_f} = \frac{\rho_l R_g T_{g,0} |T'_{w,0}|}{8\pi\mu_l H_v R_{th} \hat{P}_e} \quad (2-10b)$$

The exponential term  $e^{\bar{\alpha}\tau}$  determines whether the oscillations grow or decay. The instability number  $\Pi$ , which is the ratio of the phase change coefficient to the friction force coefficient, defines the threshold ( $\Pi > 1$ ) at which the system becomes unstable and oscillations starts (see Figure 2-14). The  $\Pi$  number proposes different mechanisms to boost the instability, including the increase of the thermal gradient at the equilibrium position  $|T'_{w,0}|$ , the decrease of the external pressure  $\hat{P}_e$ , or the decrease of the phase change thermal resistance (by improving the net evaporation).

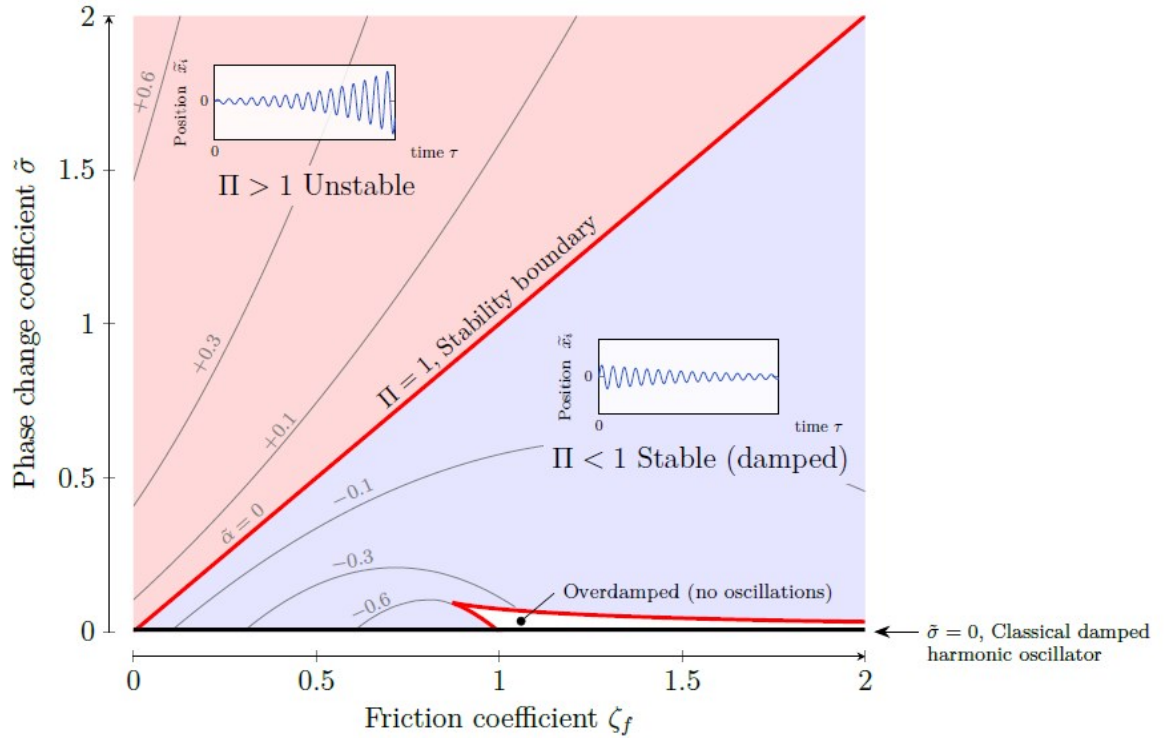


Figure 2-14 The equilibrium state of SBPHP system modeled by Tessier-Poirier [48]: for  $\Pi < 1$  the system is stable (friction is greater than phase change) while for  $\Pi > 1$  the system is unstable and any perturbations leads to oscillations. Figure is reproduced with the authorization of APS.

## 2.4.2. Resonator

Compression-expansion of the vapor bubble generates a spring force coupled with the inertia of the liquid plug creates a resonator that its existence has been already shown by Das et al. [52] and Ma et al. [57]. The natural frequency of this spring-mass system is defined as:

$$\omega_n = \sqrt{\frac{k}{m_l}} = \sqrt{\frac{P_{g,0}}{\rho_l L_l L_{g,0}}} \quad (2-11)$$

The expression for  $\omega_n$  was experimentally validated by Monin et. al [58]. From an energy perspective, when there is no friction and phase change, the energy of the resonator is conserved and thus the energy is only exchanged between the kinetic and potential over a cycle. As proposed by Tessier-Poirier [48], obtained from linearization for small  $\tilde{\sigma}$  and  $\zeta_f$ , the total energy of the resonator is:

$$E_{res} = K_{res} + U_{res} \approx \frac{1}{2} r^2(\tau_i) \quad (2-12)$$

with  $r(\tau) \equiv a_2 e^{\bar{\alpha}\tau}$ . This shows that the total energy of the resonator is directly linked to the oscillation amplitude ( $r$ ). Therefore, an increase (decrease) of the total energy of the resonator leads to an increase (decrease) of the oscillation amplitude.

### 2.4.3. Phasing between variables

The solution of the linearized equation for the instability number of 1.01 and  $\zeta_f=0.04$  at  $\tau=\pi/4$  is presented in Figure 2-15. The evolution of the meniscus position, velocity, and forces from pressure change over a cycle reveal that the spring force is opposite to the position while the feedback force (from phase change) is in phase with velocity. The phase change force is produced from the phase change rate that is opposite to the meniscus position [48].

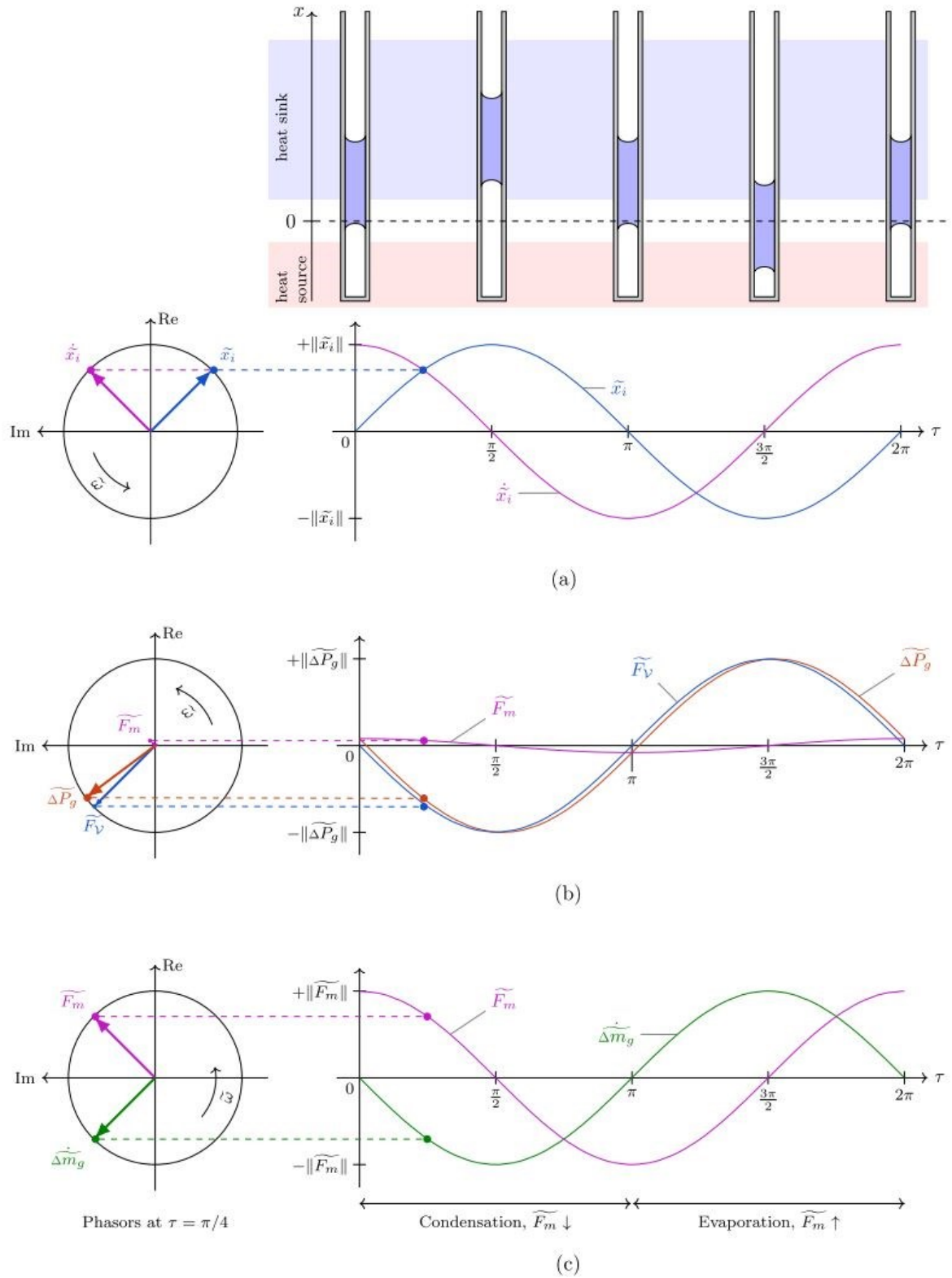


Figure 2-15 The evolution of variables and their phasor representation over a cycle in the system modeled by Tessier-Poirier [48]: a) meniscus position and velocity, b) forces from change of pressure (spring force opposite to position and feedback force in phase with velocity), c) the phase change rate that is opposite to position generating a force that is in phase with velocity. Figure is reproduced with the authorization of APS.

The model is validated with experimental measurements of the variables during the start-up (Figure 2-16). At the beginning of the start-up (the zoom-in box), the dynamics are linear and the variables evolve as a sinusoidal function. As the amplitude increases, nonlinearities become more significant which leads to the appearance of harmonics in the variables and finally brings system to a steady state. The phasing relationship between the variables are agreement with the model. The friction is opposite to velocity (acts as dissipation) while the mass of vapor is in phase with velocity (acts as positive feedback, injects energy into the system).

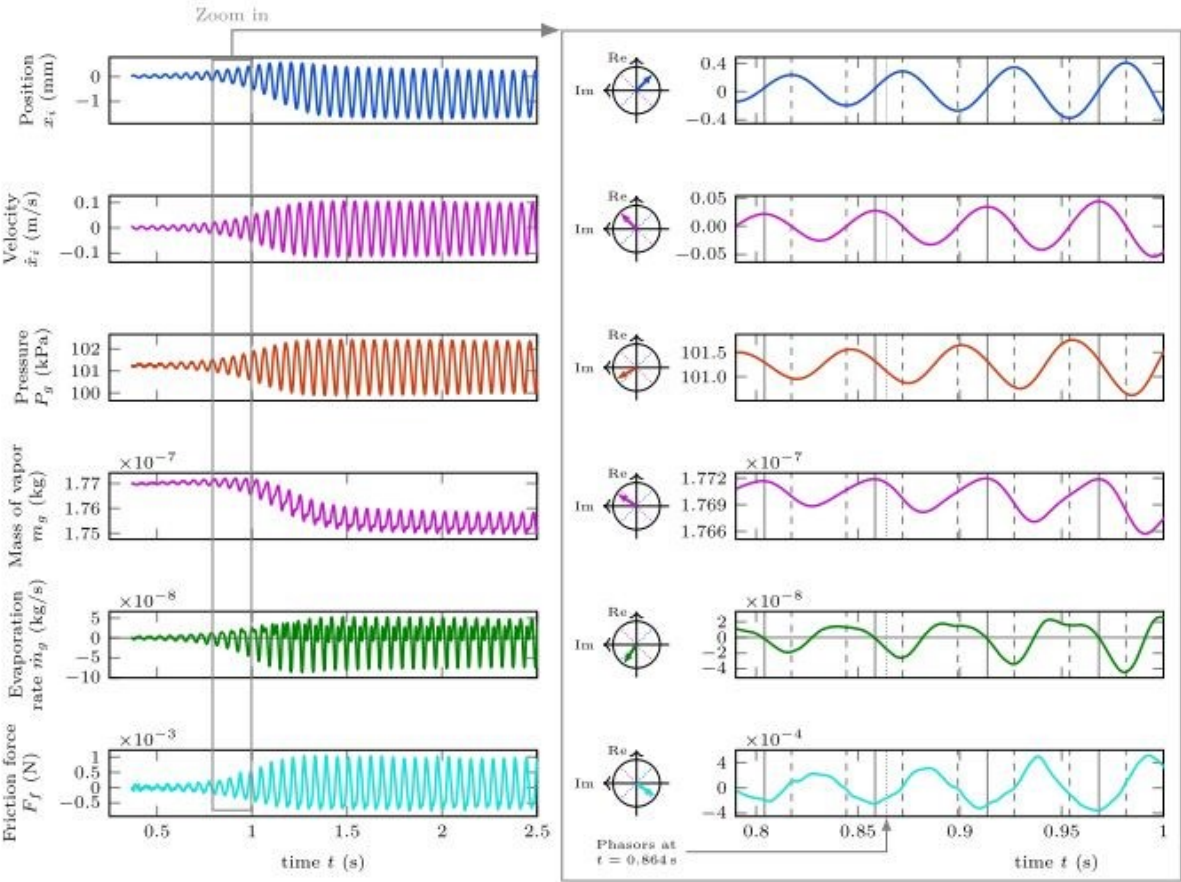


Figure 2-16 The evolution of the variables measured experimentally by Tessier-Poirier [48] during the startup: the dotted lines in the phasor graphs represent the position and velocity. Figure is reproduced with the authorization of APS.

**2.4.4. Saturation of oscillation amplitude**

The linearization of the equations revealed the instability mechanisms; however, it does not explain why the amplitude of the oscillation saturates as shown in Figure 2-17 (that is the oscillation amplitude in a SBPHP during startup). Tessier-Poirier et al. achieved an approximate analytical solution of the nonlinear system by applying center manifold reduction techniques followed by normal reduction techniques [59]. As shown in Figure 2-18, the sources of nonlinearity are the pressure described by the ideal gas law and the phase change mechanism (limited thermal gradient for example). The solution showed that the saturation of the oscillation amplitude is because of the nonlinearities that will consequently bring the system into a steady state.

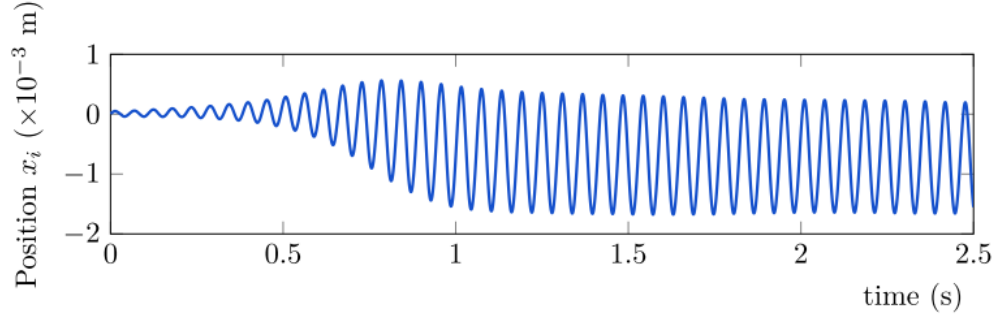


Figure 2-17 The experimental measurement of the oscillation amplitude during startup in the SBPHP studied by Tessier-Poirier [59].

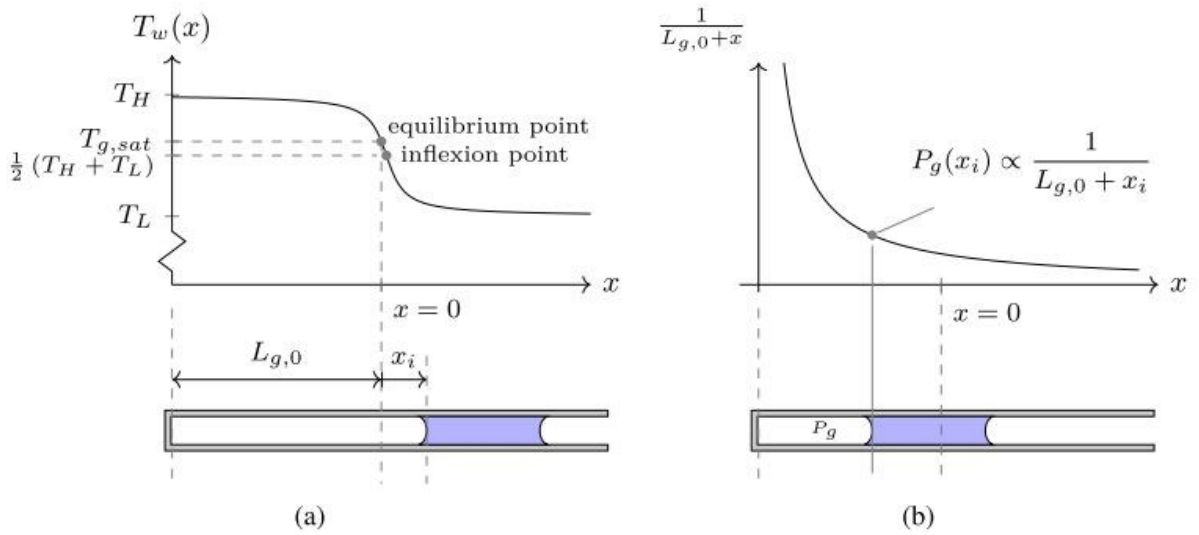


Figure 2-18 The sources that introduces nonlinearities to the system (SBPHP) studied by Tessier-Poirier [59]: a) nonlinear wall temperature profile that leads to a nonlinear phase change profile, b) the pressure of the gas defined by ideal gas law.

### 2.4.5. Role of phase change

The instability analysis provides valuable insights into enhancing the oscillation amplitude of the system. It is observed that increasing the phase change coefficient contributes to amplifying the oscillation amplitude, while reducing the impact of nonlinearities arising from the phase change leads to similar outcomes. Hence, the key to increasing the oscillation amplitude lies in simultaneously promoting instability while mitigating nonlinear effects.

Furthermore, the phasor diagram demonstrates the significance of attaining a phase change profile that creates a force, which is perfectly in phase with velocity. This finding highlights the crucial role of the phase change mechanism in facilitating the growth of oscillations. Given the pivotal role played by the phase change, the subsequent section of this chapter will delve into a detailed exploration of the mechanism of phase change from thin film.

## 2.5 Thin film phase change

As discussed, the oscillation amplitude in SOFHE is highly dependent on the phase change

(evaporation-condensation). Therefore, it becomes crucial to understand the key parameters that influence the net evaporation rate and how they can be manipulated. In this section, we embark on elucidating the formation of the thin film within the context of oscillatory slug-plug flow in SB-PHP. Subsequently, we shift our focus to reviewing the fundamentals of evaporation from the thin liquid film. Moreover, we explore various approaches that have been proposed to enhance the phase change from the thin film.

### 2.5.1. How thin film forms in oscillatory flow

Nikolayev [38] provides an extensive review on the dynamics of the liquid film in PHP. They offer valuable insights into the behavior and characteristics of the liquid film within this context. Notably, Rao et al. [41] and Das et al. [52] conducted pioneering work in visualizing the thin film in SB-PHP. Their experiments confirmed the presence of a thin liquid film on the tube walls, left behind by the trailing edge of the liquid plug as it moves towards the condenser. These studies highlighted the significance of the thin liquid film in facilitating heat and mass transfer processes within the system.

The formation of the thin film can be attributed to hydrodynamic factors. It is governed by the interplay of two opposing forces: the viscous friction force and the surface tension force. As the liquid plug recedes, the friction force hinders the flow and retains the liquid near the wall, while the surface tension force strives to keep the liquid contained within the plug [60][61][62]. This delicate balance of forces gives rise to the formation and maintenance of the thin liquid film. To describe this counteractive effect, the concept of the capillary number is often employed. The capillary number represents the ratio the viscous friction force to the surface tension force, providing a quantitative measure of the interfacial dynamics and the stability of the thin film:

$$Ca = \frac{\mu U}{\sigma} \quad (2-13)$$

where  $\mu$  is viscosity,  $\sigma$  is surface tension, and  $U$  is velocity. The thin film, which is left behind in the evaporator, gives rise to distinct regions within the system, as illustrated in Figure 2-19. The thin film in the evaporator region was observed to possess a nearly flat shape, with a noticeable ridge at its end. Notably, the contact line, characterized by minimal thermal resistance, was found to have a significant influence on the net evaporation rate compared to the remaining portion of the thin film [44].

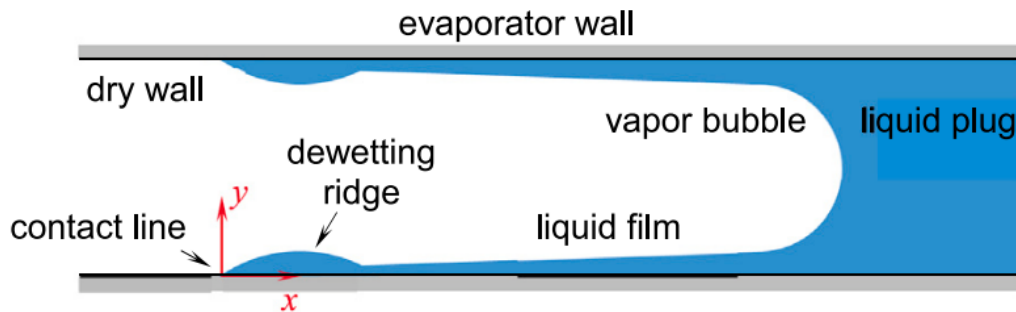


Figure 2-19 Different regions in the evaporator of the SBPHP forming due to receding of the liquid plug studied by Fourgeaud [44].

### 2.5.2. Thin film evaporation fundamentals

An insightful study by Plawsky et al. [63] offers fundamental explanations of phase-change transport in thin films. In their work, Plawsky et al. present three hypothetical regions (as

depicted in Figure 2-20) to elucidate the evaporation process from a thin liquid film. Region 1 represents a region with an almost infinite thermal resistance, where evaporation is hindered by the combined effects of attractive forces between the solid and the liquid. Transitioning to Region 2, the attractive forces weaken, leading to active evaporation and resulting in thickness and curvature gradients in the liquid-vapor interface. In this region, the thermal resistance reaches a minimum due to the relatively thin liquid film thickness, which presents a moderate conduction resistance that can overcome the interfacial resistance. Moving further, Region 3 encompasses the bulk fluid with a thicker liquid film, which acts as a reservoir facilitating liquid flow via capillary forces.

In addition to heat transfer resistances, various hydrodynamic resistances impose fundamental limitations on the evaporation rate. These include factors such as vapor pressure, capillary limits, and friction force. These phenomena have been observed experimentally [64–66] and simulated numerically by several researchers [67–69].

To optimize phase-change processes in thin films, it is essential to maximize the region with reduced overall heat transfer resistance while simultaneously minimizing hydrodynamic resistances associated with liquid and vapor pumping. Achieving this objective requires altering the surface energy of the solid through surface patterns created via chemical or physical modifications. These modifications play a crucial role in enhancing the phase-change dynamics and will be further explored in the subsequent sections

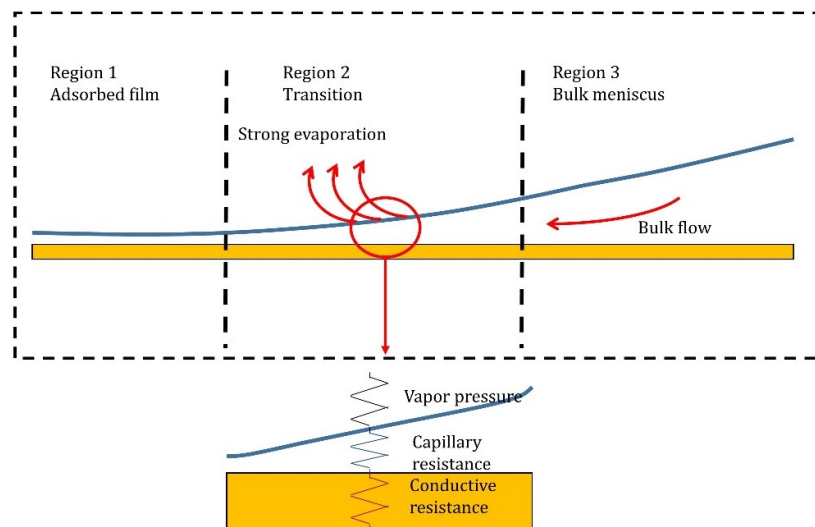


Figure 2-20 Schematic of different regions in thin film evaporation [63].

### 2.5.3. Phase change enhancement

Chemical modifications involve altering the surface chemistry of the material. One approach is to introduce polar molecules onto the surface, which imparts hydrophilic properties. These polar molecules have the ability to form hydrogen bonds with water molecules, resulting in increased surface wettability. Techniques such as oxygen plasma treatment have been employed to create surface hydroxyl (-OH) groups, facilitating hydrogen bonding [70–72]. Additionally, the deposition of films with tailored surface functional groups can be utilized to enhance surface chemistry [73]. These modifications effectively promote capillary action and enhance the interaction between the surface and the surrounding liquid.

Physical modifications like sub-micrometer or nano-sized surface patterns have been studied by numerous researchers to enhance the evaporation rate in the thin liquid film [63,74–77]. The motivation behind using such structures is to reduce the three limitations that determines the evaporation rate in thin film. As presented in Figure 2-20, there are three resistances in series, which are the conductive resistance through the solid, the capillary resistance, and the resistance created by vapor pressure.

Reducing each of these resistances leads to an increase in evaporation rate that can be achieved by microstructures. The effect of microstructures can be summarized as follows:

- To reduce conductive thermal resistance by providing more surface solid-liquid interface area facilitating the transfer of heat to the active zone of the evaporation
- To change the shape (increase the curvature) of the liquid-vapor interface that leads to higher capillary pressure and thus more liquid can be injected to the active zone by capillary action
- To create more perimeter at which we can have the evaporation active zone

Figure 2-21 qualitatively depicts the effect of microstructures on thin film evaporation. In a study by Bigham et al. [75], they showed that a liquid film formed on a textured surface takes a longer time to evaporate compared to a liquid film formed on the plain surface. They observed that the capillary wicking effect induces micro-inflows within the pillars during the thin film evaporation process leading to a longer drying time scale.

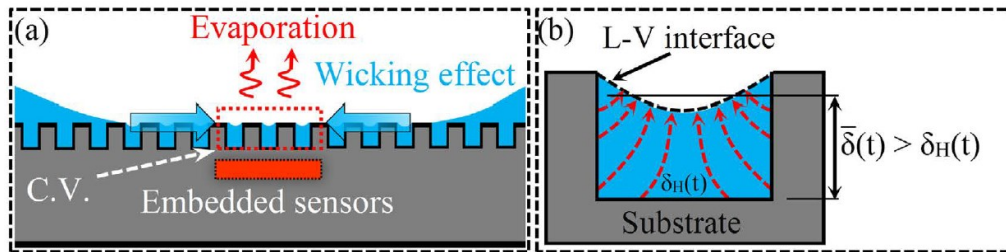


Figure 2-21 Cross-sectional view of surface pillars (a) liquid wicking and evaporation, (b) heat flow from the walls to the liquid-vapor interface [75].

Through conventional microfabrication processes, we can develop a rational direction for the development of micro/nanostructures for thin-film evaporation. The optimal dimensions of features in the micro/ nanostructures from the literature reviews vary between 2-36  $\mu\text{m}$  for height, 0.5-20  $\mu\text{m}$  for diameter and 0.5-15  $\mu\text{m}$  for spacing [75,77–79]. Figure 2-22 presents the process flow for the microfabrication of such microstructures.

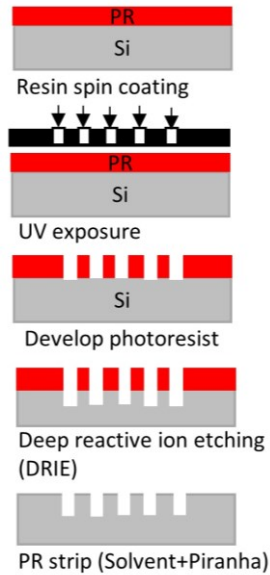


Figure 2-22 Schematic view of the microfabrication process for microstructures to improve thin film evaporation.

In addition to microstructure, the inclusion of capillary paths, such as sharp corners shown in Figure 2-23, can also contribute to enhancing phase change dynamics [80,81]. The presence of sharp corners facilitates the formation of thin films as the liquid is drawn through capillary pumping mechanisms. This capillary action allows for efficient liquid transport and helps optimize the phase-change process. By strategically incorporating these capillary paths, the overall performance of phase-change systems can be improved, leading to enhanced heat transfer and operational efficiency.

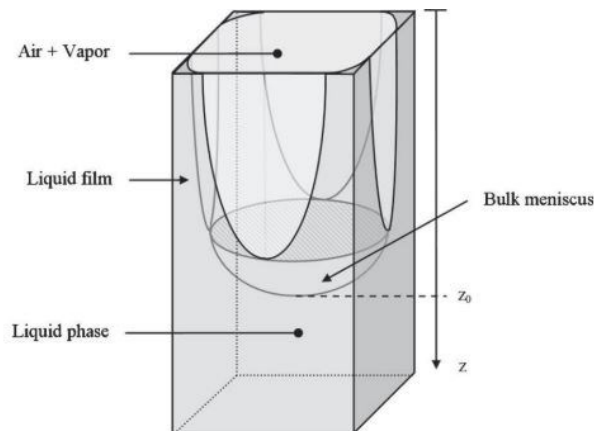


Figure 2-23 Schematic of the capillary pumped liquid through corners of a square cross-sectional capillary tube [81].

The literature highlights various attempts to enhance phase change performance in PHPs by incorporating wicking structures such as micro grooves [82] and ultra-sharp grooves [83], as depicted in Figure 2-24 and Figure 2-25, respectively. Researchers have primarily assessed the impact of these modifications by measuring thermal resistance, which has shown improvements in PHP performance.

However, it is worth noting that there is limited measurement or visualization of how these structural modifications specifically influence the net evaporation rate and contribute to the oscillation amplitude within the PHP. Furthermore, the effectiveness of different phase change profiles resulting from these modifications in an oscillatory flow has yet to be evaluated.

While improvements in thermal resistance provide valuable insights into the overall heat transfer characteristics, further research is needed to understand how these wicking structure modifications affect the specific aspects of phase change dynamics, including the net evaporation rate and their influence on the oscillation amplitude. Such investigations will provide a more comprehensive understanding of the effectiveness of these modifications in enhancing PHP and the SOFHE performance.

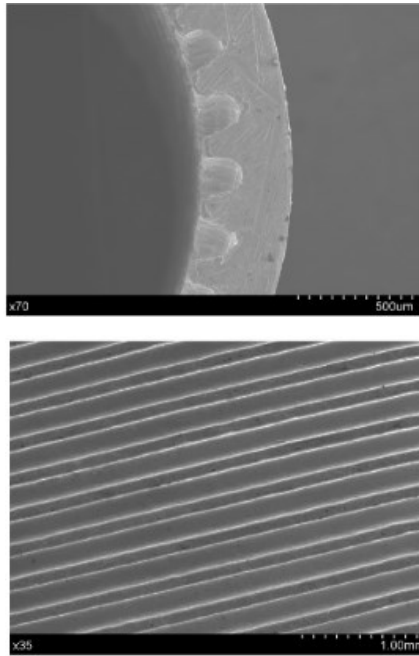


Figure 2-24 SEM images of the local cross-section (top) and inner surfaces (bottom) of the micro-grooved tube to improve PHP performance [82].

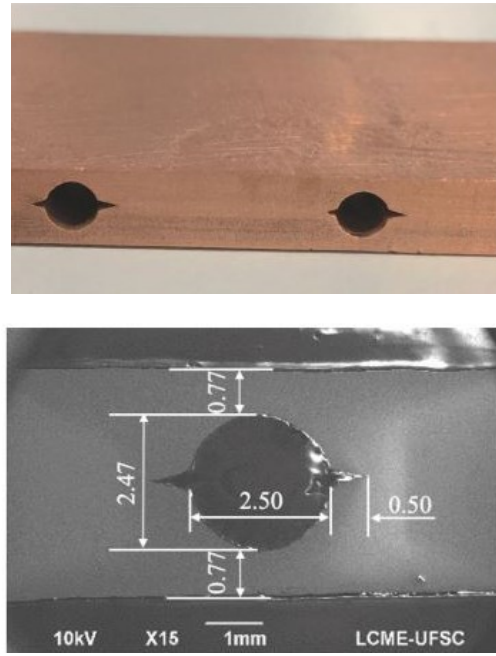


Figure 2-25 The ultra-sharp corner added to the PHP (top) and the SEM images of the grooved profile (bottom) [83].

## 2.6 Transducer

To extract energy from the SOFHE, there are three main electro-mechanical transducers including, electro-magnetic, electrostatic, and piezoelectric materials. Each transducer operates based on distinct working principles, which we will delve into to enhance our understanding of their transduction mechanisms.

### 2.6.1. Electromagnetic transducer

In electro-magnetic transducers, energy is extracted by a damper whose force is proportional to velocity with a constant of proportionality. Electromagnetic transducers are typically composed of a moving magnet linking flux with a stationary coil or vice-versa. The operating principle is that voltage is induced in the coil due to the varying flux linkage, with the resultant currents causing forces, which oppose the relative motion between the magnet and coil. Therefore, the induced electromotive force is directly proportional to the change of magnetic flux that highly

depends on the configuration of the magnet-coil and the motion properties (frequency and amplitude). As presented in Table 2-1, most electro-magnetic converters are available at a volume of less than 1 cm<sup>3</sup> capable of producing acceptable range of power density at low frequency. The main drawback of these devices is their low output voltage that requires a rectification (<1 V). The power density generated by these converters equals to around 100 μW/cm<sup>3</sup> at the frequency range of 100 Hz and it depends on the acceleration caused by the vibrations and the movable mass [84]. The comparison presented hereby can show us that the magnitude of the power density we can extract from the SOFHE by electromagnetism as the characteristics of the motion provided by the SOFHE is at low frequency (tens of Hz) with an amplitude range of less than 2 cm. In macro-scale, high-performance bulk magnets and multi-turn coils are readily available while in wafer-scale systems, it is difficult to have an efficient design. This is mainly due to the undesirable properties of planar magnets, limited number of turns achievable with planar coils. The transduction mechanism highly depends on the dimension as the power decreases remarkably at small scales.

Table 2-1 Comparison of power density by published electromagnetic vibration driven harvesters

Input frequency (Hz)	Input amplitude (μm)	Maximum displacement (μm)	Generator volume (cm <sup>3</sup> )	Power density (μW/cm <sup>3</sup> )	Magnet-coil configuration
60-120	200	1000-5000	1	100	Moving magnet-fixed coil [85]
322	13	360	0.84	44	Two moving magnets-fixed coil [86]
322	25	940	0.24	2208	Moving magnet-fixed coil [87]
85	150	7500	7.3	114	Moving magnet-fixed coil [88]
350	0.62	217	0.06	47.5	Moving magnet-fixed coil [89]

### 2.6.2. Electrostatic transducer

Electrostatic converters are capacitive structures made of two plates separated by air, vacuum or any dielectric materials. The charging of the plates by a battery of voltage  $V$  creates equal but opposite charges on the plates,  $Q$ , leading to a storage of the charge when the voltage source is disconnected. To harvest energy from a resonant generator like the SOFHE by electrostatic transducers, there are three approaches, including changing the gap between the electrodes, changing the overlapping area, and changing the permittivity of the capacitor by moving the dielectric materials between the two plates. As shown in Table 2-2, electrostatic transducers show a potential of producing electrical energy from low frequency vibration sources. Unlike the electromagnetic approaches, the electrostatic concept is highly compatible with MEMS. One advantage of such converters is the increase of their energy density by the decrease of the capacitor spacing that is favorable for miniaturization. However, the energy density decreases because of decreasing capacitor surface area. This issue can be compensated thanks to the possible configuration of stacking more capacitor plates on top of each other by decreasing the gap between the plates for the same volume. Depending on which conversion cycle is applied to extract energy (charge-constrained or voltage-constrained), we can reach high or low impedance in the output. However, the disadvantage of electrostatic converters is the requirement of an initial polarization source. To address such a problem, researchers have been attracted to utilizing electrets to provide the initial charge [2].

Table 2-2 Comparison of power density for electret-free electrostatic vibration driven harvesters.

Input frequency (Hz)	Initial charging voltage (V)	Generator volume (cm <sup>3</sup> )	Power density (μW/cm <sup>3</sup> )	Configuration
6	45	15	2.4	Out-of-plane gap closing [90]
50	3	18	58	In-plane gap closing [91]
10	26	1.6	15	Out-of-plane gap closing [92]

### 2.6.3. Piezoelectric transducer

The term ‘piezoelectricity’ is used to describe dielectric materials that can have an electrical field induced across their boundaries when a mechanical stress is applied on them [93]. The main advantage of piezoelectric converters is their structural simplicity converting vibration directly into the output voltage. Another benefit of such converters is their compatibility to micro-engineering processes to deposit piezoelectric films with different thicknesses. However, the performance and lifetime of piezo converters are restricted by the mechanical properties of the materials. The output voltage and impedance of piezo converters are typically high which needs a conditioning circuit. Such a technology has been already tested for the SOFHE by Monin et. al [4]. They designed and fabricated a piezoelectric spiral membrane shown in Figure 2-26. The motivation behind considering spiral shape for the membrane was that it allows the control of the mechanical stiffness to adjust its impedance. However, they observed that the design leads to an inefficient transducer with considerable dissipation of energy. They concluded that the conversion efficiency can be improved if we could match the mechanical impedance of the heat engine with the impedance of the transducer.

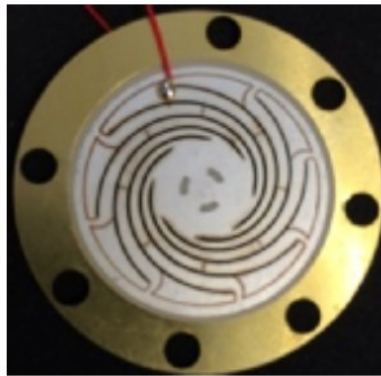


Figure 2-26 Piezoelectric spiral membrane attached to the SOFHE [4].

## 2.7 Impedance matching

Once an efficient design for the heat engine and transducer has been identified, the next crucial step is to efficiently integrate them to achieve maximum power transfer. This integration can be achieved through impedance matching, which requires understanding of the transfer mechanism between the components. By defining the impedance of each part and exploring methods to control their impedances, we can optimize the energy transfer process. Generally, when the force is too high, it can stop the motion, while if the force is too low, the motion will not be impeded, but also no work will be done. Striking the right balance with impedance matching ensures enough counter force to extract energy without halting the motion.

To visualize the overall energy harvester system, we present a schematic representation that captures the integration of the heat engine and transducer (Figure 2-27). This schematic serves as an illustration of the entire system, highlighting the interplay between the various components.

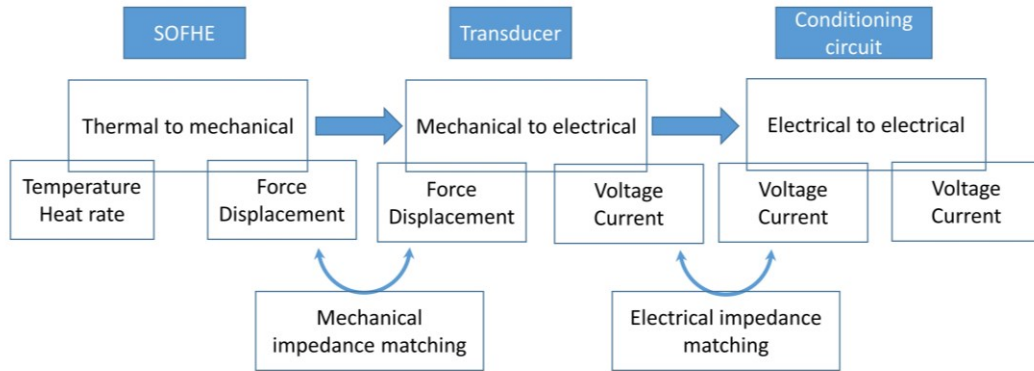


Figure 2-27 Schematic of the transduction mechanisms involved in our thermal energy harvester.

Impedance matching is the practice of adjusting the impedance of the load with the impedance of the corresponding source to transfer the maximum power. This can be proved based on the maximum power transfer theorem [94]. The concept of impedance is mostly used in electrical circuit but by impedance analogy, we can define the mechanical impedance of a system as well. In this analogy, each mechanical element has an electrical equivalent presented in Table 2-3.

Table 2-3 Electrical equivalent of mechanical component.

Mechanical quantity	Electrical quantity
Force, $f$	Voltage, $V$
Velocity, $v$	Current, $i$
Position, $x$	Charge, $q$
Mass, $m$	Inductance, $L$
Stiffness, $k$	Reciprocal of capacitance, $1/C$
Damping coefficient, $\mu$	Resistance, $R$

Electrical impedance is defined as a measure of the opposition of a circuit to current when a voltage is applied which is the same as the mechanical impedance as it is a measure of how much a system resists motion when subjected to a harmonic force. By this definition, we can understand that the electrical impedance relates voltage with current while the mechanical impedance relates forces with velocities.

$$Z_{elec} = \frac{V}{I} \quad (2-14a)$$

$$Z_{mech} = \frac{F}{v} \quad (2-14b)$$

Mitcheson et al. [95] studied the vibration driven generators based on the damping force by which the transducer generates power. They defined power as:

$$P = -\frac{1}{T} \int_0^T f_t v dt \quad (2-15)$$

where  $v$  is the velocity and  $f_i$  is the damping force extracted by the transducer and  $T$  is period. Therefore, the power generation for a given size of generator is dependent upon the nature of the damping force by which energy is extracted. Generally, we can define two types of resonant generators based on their damping force [95]:

- Velocity-damped resonant generator (VDRG): the damping force is proportional to velocity like electromagnetic transducers.
- Coulomb-damped resonant-generator (CDRG): energy is extracted by a damper that provides a constant force in the direction opposing the motion like electrostatic transducers.

They defined  $f_i$  for different architecture of transducers of electromagnetic and electrostatic vibration driven harvesters and explained how we can maximize power by optimizing the damping versus the vibration amplitude. The damping force approach is useful to improve the performance and to maximize power transfer. However, impedance matching is still a more powerful analytical tool for our purpose since it is a more complete definition. By impedance matching, we can analyze not only the magnitude but also the phase of the forces involved in the transduction mechanism.

### 2.7.1 Influential parameters on impedance of the SOFHE

It is highly important to identify the parameters that affect the mechanical impedance of the SOFHE as well as the transducer. the parameters are summarized in Table 2-4.

Table 2-4 Influential parameters on mechanical impedance of the SOFHE and the transducer.

Component		Parameters of mechanical impedance
SOFHE	Evaporation-condensation rate	Heat source temperature Fluid (latent heat, viscosity, surface tension, wettability) Surface potential (hydrophilicity, surface tailored) Wall temperature profile (Adiabatic zone) Heat sink temperature
	Inertia	Liquid length Diameter (direct relationship)
	Spring force	Equilibrium pressure Vapor length
	Friction force	Angular frequency (vapor length, liquid length, liquid density, external pressure) Diameter (inverse relationship)
Transducer	Electrostatic	Gap Area Initial polarization voltage Configuration Conversion cycle
	Electro-magnetic	Magnet material (magnetic field strength) Number of turns in coil and its area Magnetic flux (magnet size) Configuration of magnet-coil
	Piezoelectric membrane	mass of membrane stiffness of membrane

## 2.8 Conclusion

This chapter provided an overview of the literature on various types of thermal energy harvesters, setting the stage for a comparative analysis of the SOFHE with its competitors. This comparison can be carried out thanks to the findings discussed in chapter 3. Within this chapter, we experimentally characterize the thermodynamic work and mechanical power density of the SOFHE under different operating temperatures, also considering the impact of two design parameters.

Theoretical models highlighting the significance of phase change in influencing instability and oscillation amplitude guide us towards the investigation of phase change phenomena in the SOFHE, the subject of Chapter 4. In this chapter, we experimentally explore two distinct oscillating regimes and propose a novel method to evaluate the efficacy of the phase change profile.

Furthermore, drawing inspiration from techniques discussed in enhancing phase change from thin films, Chapter 5 presents our proposed design for the SOFHE, incorporating integrated wicking structures. This chapter elaborates on the design, fabrication, and testing of three microfabricated SOFHEs, comparing them in terms of oscillation amplitude and power output.



# Chapter 3

## What is the potential of the SOFHE?

**Authors and affiliation:** Nooshin Karami<sup>1,2</sup>, Albert Tessier-Poirier<sup>1,2</sup>, Alihossein Nikkhah<sup>1,2</sup>, Etienne Léveillé<sup>1,2</sup>, Thomas Monin<sup>1,2,3</sup>, Fabien Formosa<sup>3</sup>, Luc G. Fréchette<sup>1,2</sup>

<sup>1</sup>Institut Interdisciplinaire d'Innovation Technologique (3IT), Université de Sherbrooke, Sherbrooke, QC, Canada

<sup>2</sup>Laboratoire Nanotechnologies Nanosystèmes (LN2), CNRS UMI-3463, Université de Sherbrooke, Canada

<sup>3</sup>SYMME, Université Savoie Mont-Blanc, Annecy-le-Vieux, France

**Submission date:** 18-02-2022.

**Acceptance date:** 25-03-2022.

**Publication date:** 01-04-2022.

**Status:** final version is published.

**Journal:** Energy Conversion and Management.

**Reference:** Karami N, Tessier-Poirier A, Nikkhah A, Léveillé E, Monin T, Formosa F, et al. Experimental characterization of the thermodynamic cycle of a self-oscillating fluidic heat engine (SOFHE) for thermal energy harvesting. *Energy Convers Manag* 2022;258:115548. <https://doi.org/10.1016/J.ENCONMAN.2022.115548>.

**Title:** Experimental characterization of the thermodynamic cycle of a self-oscillating fluidic heat engine (SOFHE) for thermal energy harvesting.

**Titre français:** Caractérisation expérimentale du cycle thermodynamique d'un moteur thermique fluidique auto-oscillant pour la collecte d'énergie thermique.

**Contribution statement:** I carried out all the experimental and theoretical work presented in this article. The experimental setup was built by Thomas Monin and Étienne Léveillé. The co-authors provided advice, suggestions, and revision during the research and writing process.

**Abstract:** We experimentally studied the thermodynamic cycle of a single branch pulsating heat pipe (SB-PHP) to show its potential as a Self-Oscillating Fluidic Heat Engine (SOFHE) capable of generating electric power from heat. The engine consists of a vapor bubble trapped by an oscillating liquid plug acting like a piston in a tube of mm-scale diameter. Pressure build-up in the vapor bubble can provide net mechanical work that can then be converted into electrical energy by coupling the liquid plug motion to an electro-mechanical transducer. The transducer can be represented, in a first approach, as a dissipative mechanical load acting on the engine that will tend to reduce the oscillations. Unlike a standard pulsating heat pipe, we aim here at

maximizing the mechanical work produced rather than the heat transfer rate. However, it is still unclear how the unique thermodynamic cycle of the oscillating vapor bubble–liquid plug behaves under a mechanical load and what effects the design parameters have on the generated mechanical power. Thereby, we conducted experiments to measure the pressure, displacement and operating frequency from which the generated mechanical work and power can be evaluated under varying loads. We observed a maximum mechanical power density with a magnitude of  $0.5 \text{ mW/cm}^3$  at an optimal load and a cycle efficiency ratio with respect to Carnot of 30%. We also studied the effect of the heat source operating temperature and two design parameters on the mechanical power density. It was shown that the mechanical power density can be improved by increasing the heat source temperature, adding wicking structures inside the tube as well as decreasing the liquid length. Finally, we found that the mechanical power density of the SOFHE makes it a promising technology to power a wide range of low-power wireless sensors (requiring 10's of microwatts) for the Internet of Things (IoT), if designed with adequate electro-mechanical coupling.

**Keywords:** heat engine, self-oscillation, energy harvesting, thermodynamic cycle

**Résumé français:** Nous avons étudié expérimentalement le cycle thermodynamique d'un caloduc pulsé à branche unique (SB-PHP) pour montrer son potentiel en tant que moteur thermique fluide auto-oscillant (SOFHE) capable de produire de l'énergie électrique à partir de la chaleur. Le moteur se compose d'une bulle de vapeur piégée par un bouchon liquide oscillant agissant comme un piston dans un tube d'un diamètre de l'ordre du millimètre. L'augmentation de la pression dans la bulle de vapeur peut fournir un travail mécanique net qui peut ensuite être converti en énergie électrique en couplant le mouvement du bouchon liquide à un transducteur électromécanique. Le transducteur peut être représenté, dans une première approche, comme une charge mécanique dissipative agissant sur le moteur qui tendra à réduire les oscillations. Contrairement à un caloduc pulsé standard, nous cherchons ici à maximiser le travail mécanique produit plutôt que le taux de transfert de chaleur. Cependant, on ne sait toujours pas comment le cycle thermodynamique unique du bouchon oscillant bulle de vapeur-liquide se comporte sous une charge mécanique et quels sont les effets des paramètres de conception sur la puissance mécanique générée. Nous avons donc mené des expériences pour mesurer la pression, le déplacement et la fréquence de fonctionnement à partir desquels le travail mécanique et la puissance générés peuvent être évalués sous différentes charges. Nous avons observé une densité de puissance mécanique maximale de  $0,5 \text{ mW/cm}^3$  à une charge optimale et un taux d'efficacité du cycle de Carnot de 30 %. Nous avons également étudié l'effet de la température de fonctionnement de la source de chaleur et de deux paramètres de conception sur la densité de puissance mécanique. Il a été démontré que la densité de puissance mécanique peut être améliorée en augmentant la température de la source de chaleur, en ajoutant des structures de mèche à l'intérieur du tube ainsi qu'en diminuant la longueur du liquide. Enfin, nous avons constaté que la densité de puissance mécanique du SOFHE en fait une technologie prometteuse pour alimenter une large gamme de capteurs sans fil de faible puissance (nécessitant des dizaines de microwatts) pour l'internet des objets (IoT), s'il est conçu avec un couplage électromécanique adéquat.

**Mots clés:** moteur thermique, auto-oscillation, récolte d'énergie, cycle thermodynamique

<b>Nomenclature</b>			
$A$	area [m <sup>2</sup> ]	$x$	position [m]
$CF$	correction factor [-]	$\dot{x}$	velocity [m/s]
$D$	diameter [m]	$\ddot{x}$	acceleration [m/s <sup>2</sup> ]
$F$	force [N]	<i>Greek symbols</i>	
$h$	enthalpy [kJ/kg]	$\zeta$	load coefficient [kg/s]
		$\omega$	angular frequency [s <sup>-1</sup> ]
$L$	length [m]	$\nu$	kinematic viscosity [m <sup>2</sup> /s]
$m$	mass [kg]	$\Pi$	instability number [-]
$\dot{m}$	mass rate [kg/s]	<i>Subscripts</i>	
$P$	pressure [kPa]	C	cold
$\dot{P}$	pressure rate [kPa/s]	exp	experimental
$Q$	heat [J]	f	friction
$r$	radius [m]	g	gas
$R$	universal gas constant [J/kgK]	H	hot
$Re_w$	dynamic Reynolds number [-]	l	load
$t$	period [s]	liq	liquid
$T$	temperature [°C]	m	inertia
$V$	volume [m <sup>3</sup> ]	th	theoretical
$W$	work [J]	v	vapor

### 3.1 Introduction

The intelligent world we live in counts on the widespread use of wireless sensing devices that constantly monitor, transport data and provide information. The increasing trend of applying wireless sensors everywhere is growing fast and creating the new vision of an Internet of Things (IoT) [96], where, for example, interconnected and intelligent machines communicate to ensure safety, reduce waste and improve productivity. To be truly wireless, the connected devices must currently be powered by batteries that have a limited lifespan and need to be replaced. Considering the growing needs for distributed and embedded sensors, this state of powering wireless sensors is not practical. Therefore, there has been a notable effort among researchers to find alternative autonomous power supplies that are expected to be small, inexpensive, and highly reliable. This has led to a new field of research: Energy Harvesting. It refers to systems that capture ambient energy and convert it into useful electrical energy to recharge or ultimately replace batteries in wireless devices [97]. An energy harvester has to scavenge at least 5 $\mu$ W to compensate the sensor's standby mode power consumption, and a bit more to accumulate energy (50–500 $\mu$ J) in onboard storage to supply the periodic measurement cycle [2].

Due to the availability and constancy of untapped waste heat almost everywhere, ranging from industrial processes and geothermal sources to thermal management systems, thermal energy harvesters have attracted great attention. There are two main methods of harvesting mid- to low-grade thermal energy, including direct thermal-to-electrical and thermal-to-mechanical-to-electrical conversion. The well-established example of the former is thermoelectric generators (TEG) that work based on the Seebeck effect [3]. TEG conversion performance is mostly limited by the figure of merit of their materials. The low TEG efficiency can only be maximized by using materials with a large electrical conductivity and Seebeck coefficient while having a small

thermal conductivity, which is hard to achieve [98]. The most promising materials tend to have low thermal conductivity, requiring high heat flux and a bulky heat sink to achieve a significant temperature difference across the TEG. The thermal-to-mechanical-to-electrical conversion approach is typically more complex to implement but has the advantage of offering more flexibility in terms of design optimization compared to TEGs due to their various conversion mechanisms available. Miniaturized versions of traditional thermodynamic cycles and engines have been demonstrated, such as micro gas turbines [19–21] and micro steam turbines [22–24] that implement respectively the Brayton and Rankine thermodynamic cycles at microscale using microelectromechanical systems (MEMS) technology. They have the complexity of requiring high-speed rotating parts, but promise W-scale power at 1–10% efficiency [25]. There have also been examples of novel micro heat engines with thermomechanical and electromechanical principles that are not commonly used at macroscale. There are micro heat engines without working fluid, like a bimetallic strip heat engine with a piezoelectric transducer [27] in which the bi-stable bimetal absorbs heat until it reaches a bending threshold and snaps. This in turn impacts or releases the piezoelectric membrane, inducing electric charges. There have also been many examples of micro heat engines working with the phase change of a fluid. A micro capillary driven phase change cavity with a piezoelectric membrane, the so-called P3 heat engine [8], has been demonstrated with a peak power of  $0.8 \mu\text{W}$  at a load resistance of  $14 \text{ k}\Omega$ . A variant also uses a phase change cavity heat engine but bounded by a bi-stable membrane [17,18] that is capable of generating a mechanical power of  $1.3 \mu\text{W}$  with a cycle efficiency of 0.3%. A microfluidic heat engine based on explosive evaporation of a liquid was also demonstrated by Léveillé et al. [99]. They managed to harvest a maximum power density of  $1.6 \mu\text{W}$  for a square piezoelectric membrane of  $1 \text{ cm}^2$ .

Recently, researchers have attempted to harvest energy from multi-branch oscillating or pulsating heat pipes (PHP) coupled with different types of transducers, including a piezoelectric membrane [32], solenoid with ferromagnetic working fluid [33] or magnet [34], electrical double layer junction [35], and pyroelectric transducer [36]. The generated power density reported is in the range of tens of microwatts/ $\text{cm}^3$ . Using a PHP to produce work dates back to the water pump by Dobson et al. [51], in which they mathematically modeled the behavior of an open oscillatory heat pipe to pump water and experimentally measured the amount of water it could pump to a specific height. They experimentally measured the thermal efficiency of the system at 0.00003%, while the mechanical efficiency was not determined since they did not measure directly the work done by the displacement of the liquid plug. Gully et al. [100] studied the thermodynamic state of the vapor in PHP by temperature measurement and showed that the vapor is superheated. However, they did not study the P-V cycle of the PHP. These demonstrations and investigations confirm the interest in thermal energy harvesting using the underlying cycle of the PHP, but do not define the achievable power level or the design guidelines to maximize the power density.

There is also a vast body of literature on modeling multi-branch [101–104] and single pulsating heat pipes (SBPHP), providing insight on the underlying working principle of the self-oscillations, some with experimental validation [38]. The small amplitude oscillations, as modeled by Dobson [50,51], are known as the superheat model, where the meniscus barely penetrates inside the evaporator. For large amplitude oscillations where the meniscus sweeps both the evaporator and the condenser, a film evaporation–condensation (FEC) model was developed by Das et al. [43]. They included the local two-phase equilibrium at the vapor–liquid

interface by introducing time-varying wetting films through which the major part of the heat and mass transfer occurs. These models were then modified by Rao et al. [42] to better illustrate the PHP working principles, considering the thickening of the thin film and shortening of its length due to the evaporation at the triple contact line. A more detailed study of the dynamics of the thin liquid film in SBPHP (both shape and thickness) was carried out by Fourgeaud et al. [44]. The start-up of the SBPHP was also studied in detail [48,53,54]. So far, most of the literature is focused on the heat transfer, phase change from thin liquid films, and the start-up mechanisms in PHPs and there is a lack of knowledge regarding the potential of this technology in terms of producing work.

Taking advantage of the self-oscillating cycle in SBPHPs for a different application, which is producing work rather than transferring heat, triggered us to consider it as a heat engine with a unique thermodynamic cycle that needs to be coupled with an electromechanical transducer to maximize power extraction (Figure 3-1). This idea was first experimentally demonstrated by Monin et al. [105] as a Self-Oscillating Fluidic Heat Engine (SOFHE), in which they applied a piezoelectric membrane to harvest energy from the continuous oscillation of a single liquid plug coupled with a vapor bubble. They managed to generate 1  $\mu\text{W}$  in a 1  $\text{M}\Omega$  electrical load. The reported power, however, was for the first experimental demonstration in which the engine, the transducer and the coupling between the two were not optimized. They also microfabricated an SOFHE in a glass microchip [106]. They concluded that, unlike TEGs, this technology is not restricted by material properties alone and the power achieved has a great potential for further enhancement. However, it was not clear whether the low power output was due to the poor performance of the engine, the mechanical-to-electrical transduction mechanism, or the transducer architecture itself. This raises the need to understand the thermodynamic cycle of the SOFHE and how we can change it to increase its generated mechanical power. Once we understand how the SOFHE (as a basic component of the thermal harvester device) generates work and power, we can optimally combine it with electromechanical transducers (electrostatic, electromagnetic, and piezoelectric) to take full advantage of its heat harvesting capability. Eventually, multiples units could be combined together to increase the total power output according to the needs.

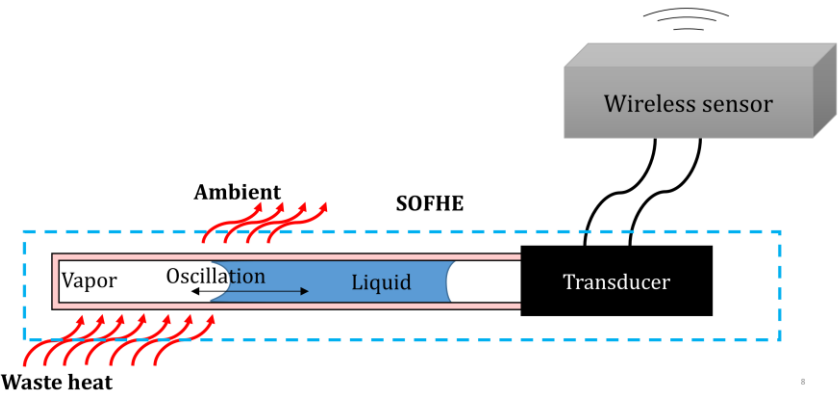


Figure 3-1 SOFHE application, harvesting waste heat to power wireless sensors.

The motion of the liquid plug during the operating cycle of the SOFHE is illustrated in Figure 3-2 (left). The working principle of the SOFHE is akin to an SBPHP, which can be viewed as a mass-spring-damper system with energy injected from the periodic phase change. As described and experimentally validated by Tessier-Poirier et al. [48], the forces responsible for the

presence or absence of self-oscillations are the pressure change ( $\Delta P_g$ ) and friction loss due to the motion of the liquid plug (damping force,  $F_f$ ). The pressure change itself stems from two phenomena: the expansion-compression of the vapor (acting as a spring force,  $F_v$ ) and the change of mass of vapor due to the phase change (acting as a positive feedback or negative damping,  $F_m$ ). The  $F_v$  coupled with the inertia (liquid plug mass) creates a resonator that enables us to explain the oscillatory behavior and to predict the frequency as well [57,107,108]. They concluded that the system becomes unstable when the ratio of  $F_m$  to  $F_f$  becomes greater than one. They called this ratio the instability number ( $II$ ). They also showed that  $F_m$  is responsible for the growth of the amplitude by injecting energy into the system (like a positive feedback). For an engine coupled with a generator, the net work provided by  $F_m$  (beyond overcoming the friction) is available to drive the generator, so for mechanical-to-electrical conversion. As shown in the corresponding Sankey diagram of the SOFHE (Figure 3-2 (right)), a fraction of  $Q_{source}$  is dissipated to the ambient through heat convection from the heat source to the outer wall of the tube and through the heat conduction of the wall thickness. The part of  $Q_{source}$  that finds its way to the engine ( $Q_{in}$ ) is used for the evaporation and expansion that finally leaves the engine by producing mechanical work ( $W_{cycle}$ ) and heat dissipation ( $Q_{out}$ ) through condensation and compression. From a work point of view, a fraction of  $W_{cycle}$  is dissipated through the friction force due to the liquid plug motion ( $W_{friction}$ ) and the rest ( $W_{net}$ ) can be harvested by a transducer.

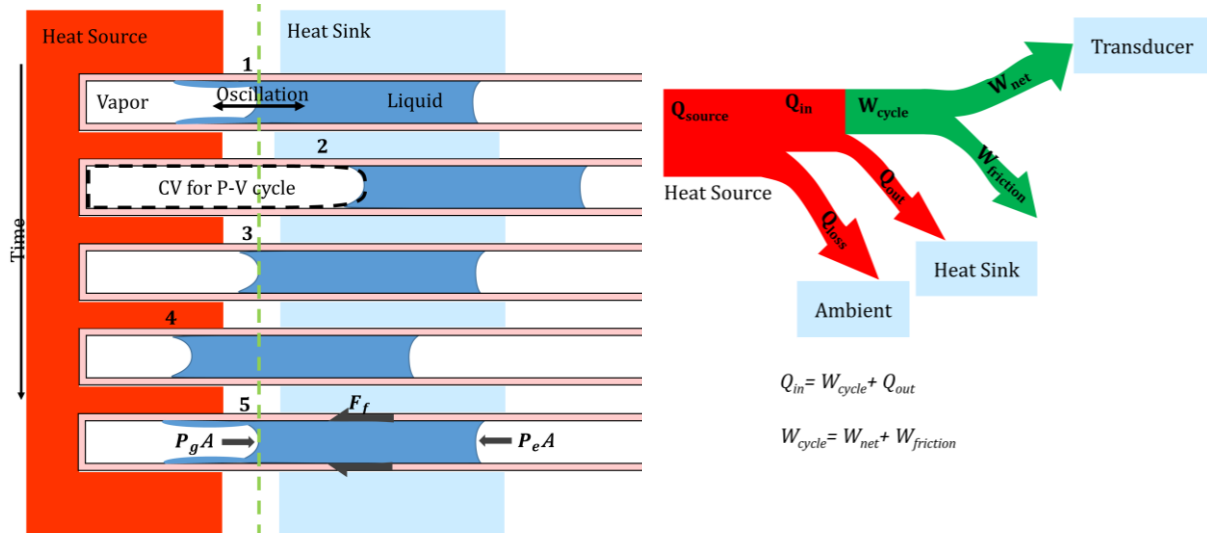


Figure 3-2 Schematic view of SOFHE operating cycle (left) and the corresponding Sankey diagram (right).

In this paper, we experimentally study how one can increase the mechanical power from the engine perspective with a focus on understanding its thermodynamic cycle. We introduced a mechanical damping load on the engine to mimic the impact of a generator, and studied the SOFHE's behavior under different load levels. We then calculated the thermodynamic work (by direct measurement of the pressure and volume) and subtracted the energy loss related to the viscous friction forces (only due to the motion of the liquid plug by an analytical model) to find the available mechanical energy. Finally, we varied the heat source operating temperature ( $T_H$ ), enhanced the evaporation rate by changing the wicking capability inside the evaporator ( $L_{fiber}$ ) and varied the liquid plug length ( $L_{liq}$ ) to explore the potential of the SOFHE in terms of mechanical work and power density. This knowledge will guide the heat engine to maximize the net work and the generator designs for optimal coupling with mechanical-to-electrical

transducers. We will show that the SOFHE could power a wide range of wireless sensors (requiring 10's of  $\mu\text{W}$ ) even with a transducer with low (10%) mechanical-to-electrical conversion efficiency.

## 3.2 Methodology

### 3.2.1 Experimental set-up

The experimental set-up (Figure 3-3) consists of a glass tube filled with deionized water with the inner and outer diameters of 2 mm and 4 mm, respectively. The tube is closed at one end, by connecting it to a pressure sensor (PX26, OMEGA Engineering), and is open at the opposite end. The closed end is inserted into a larger glass container where it is immersed in hot glycerin heated by a cartridge heater. To have a more uniform temperature distribution around the tube, a magnet mixes the glycerin continuously. A thermocouple controls the temperature of this heat source ( $T_H$ ). This constitutes the evaporator section ( $L_{g,0} = 8.5$  cm long), which is separated from the condenser part (7 cm long) by a PDMS plug (0.5 cm) acting as an ideally adiabatic section for the working fluid. In addition, a glass fiber (capillary with closed ends, Polymicro, external diameter of 350  $\mu\text{m}$ ) is inserted inside the tube into the evaporator section to play the role of a wicking structure. It enhances the evaporation rate as will be shown in section 3.4.2. For the condenser, a glass container with coolant circulation surrounds the adjacent portion of the tube. The container is connected to a thermostatic bath providing cold water at  $T_C = 20$  °C. This allows further control of the temperature difference between the heat source and the heat sink. A high-speed camera (PCO) records the position of the meniscus, synchronized with the pressure measurement. We add a deformable plastic junction to the remaining length of the tube out of the condenser and use a micrometer vice to pinch it and to dampen the liquid flow motion by decreasing the inner diameter of the plastic part. This introduces a mechanical damping load to the engine that acts as a viscous damping force, mimicking the damping force that would be provided by an electro-mechanical transducer. When there is no load, the amplitude is maximum. As we start pinching the plastic tube, we exert a damping force by obstructing the liquid plug motion and the amplitude decreases. We continue pinching the liquid plug until the oscillations stop. Each load level corresponds to a specific decrease in the inner diameter of the plastic junction. We can estimate the load coefficient, as will be discussed in section 2.3. For a real electromechanical transducer, there is both a dissipative damping force (resistance) and a spring force (reactance). The former affects the amplitude and the latter changes the frequency of the oscillations. The approach used here is a good way to focus on the effect of the dissipative load, which is the one that generates work in a transducer. We verified the frequency at each load level to ensure not having the reactance. It was observed that the frequency remains almost constant and the load was dominantly dissipative. At the highest amount of load, a small increase of 13% was measured in the frequency.

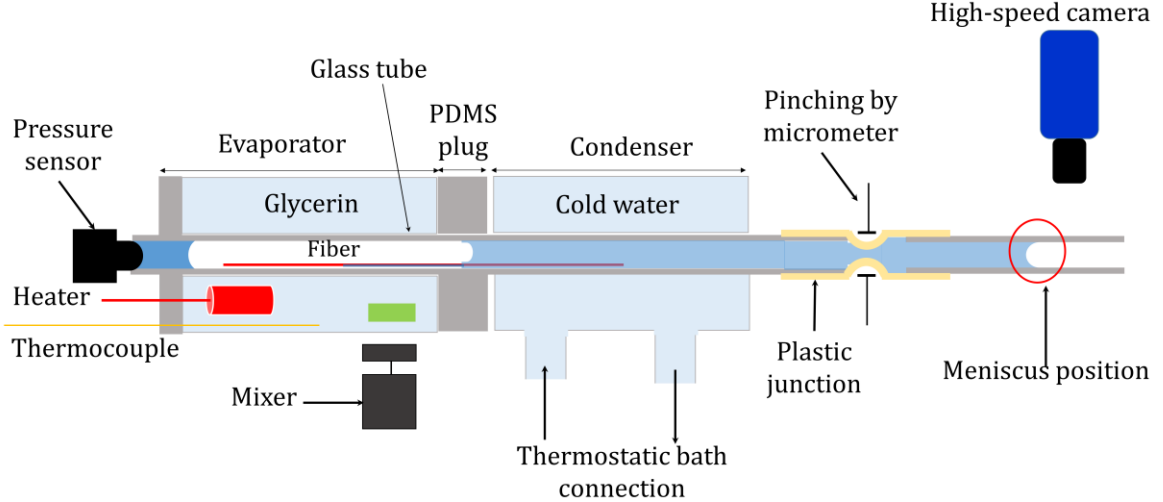


Figure 3-3 Schematic of SOFHE experimental set-up for cycle characterization [109].

### 3.2.2 Experimental procedure

Prior to starting a test, the glass tube is flushed with deionized water and plasma treated (corona discharges in ambient air using a conductive wire inserted in the tube). The plasma treatment creates a hydrophilic surface, which greatly affects the meniscus shape and eventually the evaporation rate [73,110]. The assembly of the set-up starts by inserting the tube inside the evaporator and the condenser. Next, the tube is filled with deionized water. We then connect the pressure sensor to the heated end of the glass tube, the condenser to the thermostatic bath, and the heater to the supply source. The glass fiber is now inserted into the evaporator from the open end to the desired length. To start a test, we gradually increase  $T_H$  to above 100 °C by 5 °C increments until the oscillations are about to happen. Once the oscillations reach a steady state, we start recording the meniscus position with the camera and the pressure variations. The camera images and the pressure data are synchronized using a data acquisition board (KPCI-3110). A Matlab code extracts the meniscus position from the camera images. A calibration is conducted to convert pixels into the length dimension ( $\pm 4\%$ ). A pressure calibration is carried out to convert the pressure data from volts to kilopascals ( $\pm 0.07$  kPa). The propagation of these tolerances to the derived quantities, such as force, work, and power, is calculated based on the relations in the following section and the resulting uncertainties are shown as error bars or shading in all the graphs. We run the test at different mechanical loads by increasing or decreasing the constriction at the plastic junction. We repeat the same procedures at four different heat source temperatures, six fiber lengths, and two liquid lengths.

### 3.2.3 Analytical calculation procedure

Extracting the pressure and the position from the measured signals enables us to draw the P-V diagram and calculate  $W_{cycle}$  by integrating the experimental curve:

$$W_{cycle} = \oint P_g dV_g \quad (3-1)$$

where  $P_g$  and  $V_g$  are the pressure and volume of the vapor bubble, respectively. The volume is calculated as  $(A_{tube} * (L_{g,0} + x_i))$ , where  $x_i$  and  $A_{tube}$  are the position of the meniscus and the cross-section area of the tube, respectively. We then need to subtract the portion of the  $W_{cycle}$  that is dissipated by friction, considering only the viscous dissipation of the liquid plug due to the liquid

motion, excluding the effect of contraction. To do so, we use an analytical expression for friction force in a pulsatile flow [48,56] and then take the integration of that force multiplied by the velocity to calculate the work done by this friction force:

$$F_{f,th} = -\sqrt{\frac{2}{Re_w}} \Delta P_g A_{tube} + \left( \sqrt{\frac{2}{Re_w}} - \frac{1}{Re_w} \right) \frac{\Delta \dot{P}_g A_{tube}}{\omega} \quad (3-2)$$

$$W_{Ff,th} = \oint F_{f,th} \dot{x} dt \quad (3-3)$$

where  $\dot{P}_g$  is the rate of vapor bubble pressure,  $\dot{x}$  is the velocity, and  $\omega$  is the angular frequency. This expression is valid for kinetic Reynolds numbers greater than 4 ( $Re_w \equiv \omega r^2/\vartheta > 4$ , where  $r$  is the tube inner radius and  $\vartheta$  is the kinematic viscosity), which is the case in our tests ( $90 < Re_w < 120$ ). However, this analytical expression is valid for an infinite liquid length without considering the impact of the velocity field near the menisci (end zone) [111]. To take this deviation into account, we define a correction factor ( $CF$ ) by comparing the analytical result with the experimentally measured friction force. The experimental friction force is extracted from the measurements using the momentum balance on the liquid plug at different amplitudes (by changing  $T_H$ ) [48]:

$$\ddot{x} - \frac{1}{m_{liq}} \Delta P_g A_{tube} - \frac{1}{m_{liq}} (F_{f,exp} + F_l) = 0 \quad (3-4)$$

$$W_{Ff,exp} = \oint F_{f,exp} \dot{x} dt \quad (3-5)$$

$$CF = \frac{W_{Ff,exp}}{W_{Ff,th}} \quad (3-6)$$

where  $m_l$  is the liquid mass,  $\ddot{x}$  is the acceleration,  $F_l$  is the mechanical load damping force. When there is no load ( $F_l = 0$ ), all the  $W_{cycle}$  is dissipated through the friction loss. From our measurements, a constant correction factor of  $CF=1.2 \pm 0.1$  is extracted to compensate for the end effects. Using this model, we can distinguish the baseline friction force from the additional one due to contraction, used to mimic the generator. The friction force is therefore the theoretical value multiplied by the correction factor:

$$W_{friction} = CF * W_{Ff,th} \quad (3-7)$$

Now we can calculate the available net work that can be harvested from the SOFHE by subtracting the work that is dissipated through the liquid plug motion from the work done by the cycle:

$$W_{net} = W_{cycle} - W_{friction} \quad (3-8)$$

It is convenient to define a load coefficient,  $\zeta_l$ , from the rate of work produced by the load ( $\dot{W}_l = -\dot{W}_{net}$ ) as a result of a velocity-damped force ( $F_l = -2\zeta_l \dot{x}$ ) as follows:

$$\dot{W}_l = \frac{W_l}{t} = \frac{1}{t} \oint F_l * \dot{x} dt = \frac{1}{t} \oint (-2\zeta_l \dot{x}) * \dot{x} dt \quad (3-9)$$

$$\zeta_t = \frac{-\dot{W}_l}{2\overline{\dot{x}^2}} \quad \text{with} \quad \overline{\dot{x}^2} = \frac{1}{t} \oint \dot{x}^2 dt \quad (3-10)$$

where  $t$  is the period of oscillation.

To estimate the efficiency of the cycle, we need to know how much heat is used for the phase change  $Q_{in}$  (we do not include the heat loss through the device or the sensible heat, as will be explained in more detail in section 3.3). To do so, we calculate the rate of change in the vapor mass ( $\dot{m}_g$ ) using the perfect gas law:

$$P_g V_g = m_g R T_g \quad (3-11)$$

where  $m_g$  is the mass of vapor, and  $T_g$  is the vapor temperature, which is considered to be constant and equal to  $T_H$ . This assumption can be justified as Gully et al. [100] showed that the temperature of the vapor varies by less than  $\pm 1$  °C from the wall temperature. In addition, Rao et al. [40] found that the calculated mass of vapor only changes by  $\pm 3\%$  if the measured temperature varies by  $\pm 10$  °C. Therefore, the calculated mass of vapor with this assumption is still valid. We can now calculate  $Q_{in}$ :

$$Q_{in} = \left( \frac{1}{2} \int_0^T \text{abs}(\dot{m}_g) dt \right) \times h_v \quad (3-12)$$

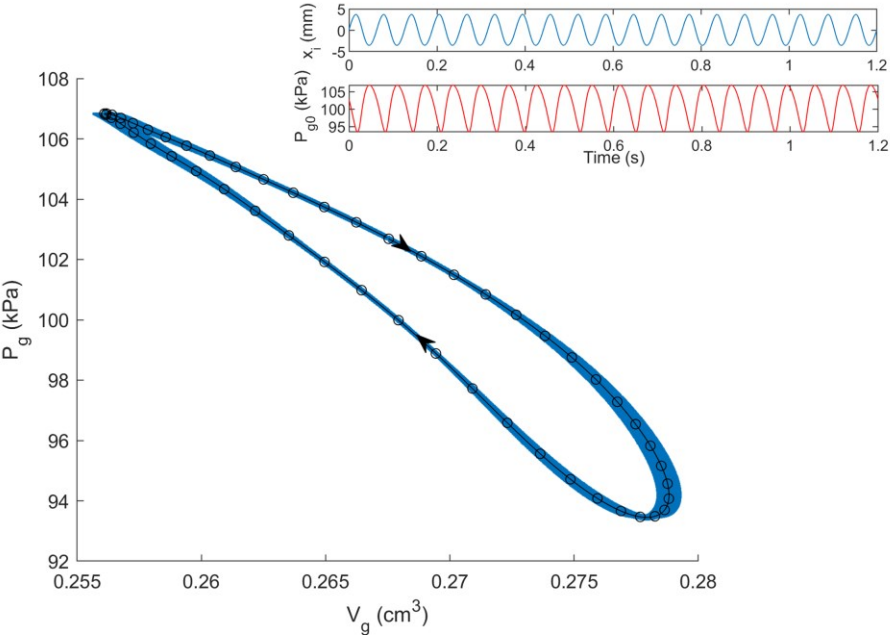
where  $h_v$  is the enthalpy of vaporization, which is considered to be constant since the difference between the enthalpy of vaporization for the SOFHE at the highest pressure (at  $P_{g,max} = 115$  kPa,  $h_v = 2247$  kJ/kg) and that of the lowest pressure (at  $P_{g,min} = 85$  kPa,  $h_v = 2270$  kJ/kg) is negligible. Considering the fact that equal and opposite amounts of heat are exchanged for evaporation and condensation, we divide the average absolute value of the phase change by two.

## 3.3 Results

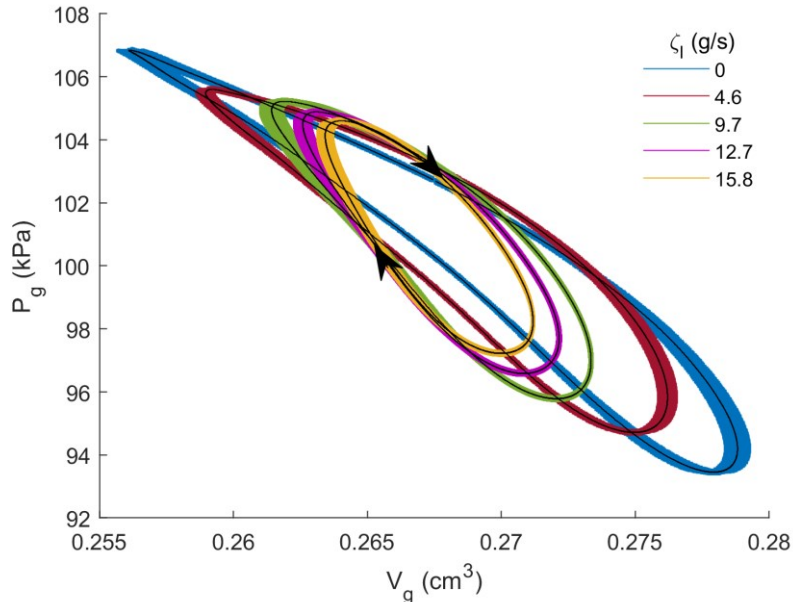
### 3.3.1 Thermodynamic cycle

The SOFHE's P-V cycle is plotted by direct measurement of the vapor bubble pressure and meniscus position at steady state (Figure 3-4a). The recorded oscillation is a periodic motion. Unlike what may be observed in PHPs, there is no chaotic behavior and the thermodynamic cycle does not change from one cycle to another. The  $P_g$  and  $x_i$  signals corresponding to the P-V cycle are shown beside it in Figure 3-4a. The cycle includes four main processes: expansion, evaporation, compression, and condensation. These processes are not discrete, but rather overlap with one another. Expansion starts when the meniscus is in the evaporator and continues until it crosses the equilibrium point ( $x_i=0$ ) and enters the condenser, where the pressure drops due to the condensation and cooling. This pulls the liquid plug back towards the evaporator, which leads to compression of the vapor. Due to the presence of the fiber, the evaporation mechanism is complex and is beyond the scope of this paper. Instead, the evaporation and condensation rates are directly extracted from the measurements, requiring no hypotheses about the phase change, thin film or wicking behavior. However, we will describe the role of the fiber in enhancing the phase change (section 3.3.4.2) and discuss the timing of the evaporation–condensation in the Discussion (section 4). Comparing the SOFHE's P-V cycles without load and with load (Figure 3-4b) shows a decrease in the liquid plug motion amplitude from 7.2 mm

at no load to 2.5 mm for the highest load (beyond this load, the self-oscillations stop). We can also notice a change in the pressure phase with respect to the volume (position), shown by a tilting of the main axis of the cycle's ellipsoidal shape.



a)



b)

Figure 3-4 Measured P-V cycle of SOFHE: a) without load, b) under different loads at  $T_H=110$  °C and fiber length at 4.5 cm.

To better illustrate the phase and its relation to the load, Figure 3-5 shows how the position, velocity and pressure change evolve over time when there is no load (left) and at the highest load (center). We can now see more clearly that in the absence of the load, when the position is at minimum, the pressure is maximum and the velocity is null. Adding load to the cycle reduces the phase difference between the pressure change and the velocity. To calculate the exact phase difference between the pressure change and the motion, we use Fourier decomposition and consider the phase difference for the fundamental component (Figure 3-5, right). When there is no load, the pressure is in quadrature with velocity (nearly completely out of phase with the position); it acts more like a conservative force and produces no work. In the presence of the load, it becomes more in phase with the velocity, which means producing  $W_{net}$ .

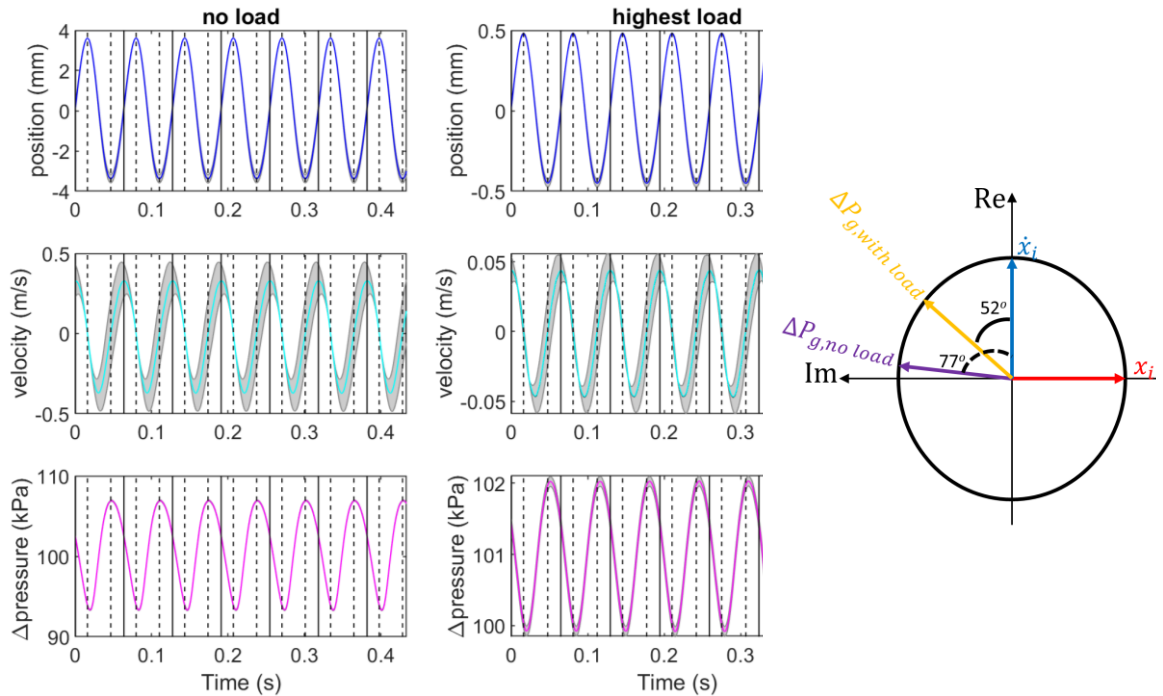


Figure 3-5 Phase comparison between the measured position, velocity and pressure change with and without the load at  $T_H=110\text{ }^\circ\text{C}$ .

### 3.3.2 Generated work and power density of SOFHE

The calculated  $W_{cycle}$ ,  $W_{friction}$ , and  $W_{net}$  are shown in Figure 3-6 as a function of the load coefficient ( $\zeta_l$ ). When there is no load, all the  $W_{cycle}$  (stacked area) is dissipated through friction loss (red area) due to the motion of the liquid plug. As we apply a load to the SOFHE, we start to harvest energy from the cycle (the bottom green area). The multiplication of the available  $W_{net}$  produced per cycle by the engine frequency (15–17 Hz) yields the available mechanical power for harvesting. To have a more realistic evaluation of the power figure regardless of the engine size, the power density is used as a metric rather than the power ( $SOFHE\ volume = \pi * (D_{out}^2/4) * (L_{g0} + L_{liq}) = \pi * (0.4^2/4) * (8.5 + 16) = 3\text{ cm}^3$ ). The bell-shaped curve in Figure 3-6 is the available mechanical power density versus the load coefficient. When there is no load, the available mechanical force is zero, as also are the net work and the power density. As we increase the load, the available mechanical force increases while the amplitude of the motion decreases. This results in an increase of the harvested work until it reaches an optimum point. From that point onwards, the  $W_{net}$  starts to decline since the decrease in the

amplitude overcomes the increase in the available mechanical force from the load. Finally, the maximum load is when the oscillation stops and consequently the work and power drop to zero. The maximum load coefficient ( $\zeta_{l\_max}$ ) is hard to measure experimentally since the amplitude becomes very small and capturing the meniscus position is not feasible. To estimate ( $\zeta_{l\_max}$ ), we fitted the data with a simplified analytical equation for the power versus load coefficient (dashed line). However, it should be noted that the parameters are adjusted to fit, thus there is some uncertainty about  $\zeta_{l\_max}$ .

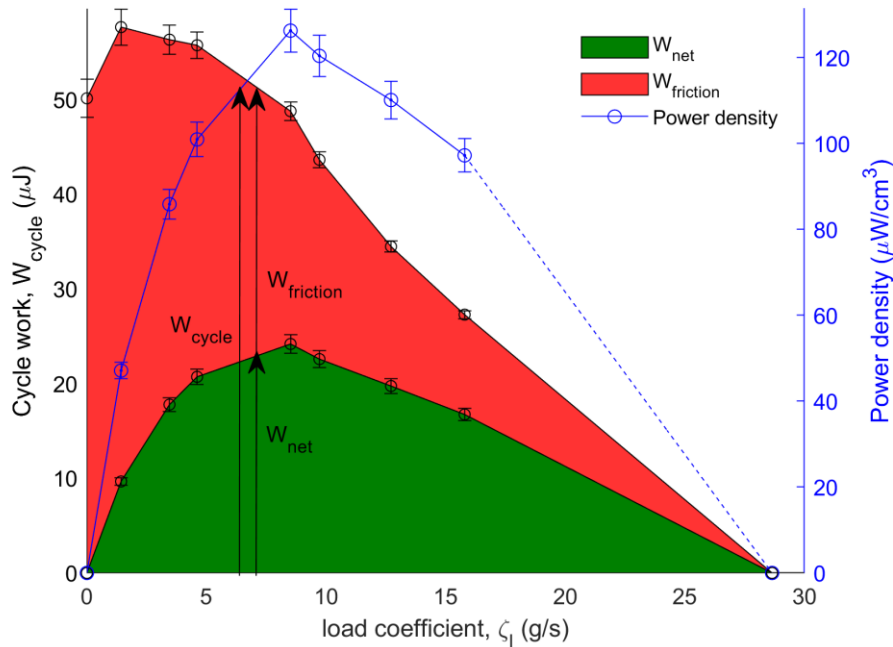


Figure 3-6 Measured  $W_{friction}$  and  $W_{net}$  (stacked area), along with the available mechanical power density (line graph) under different amounts of load at  $T_H = 110$  °C.

### 3.3.3 Efficiency

Considering the application of the SOFHE, which is supplying power to wireless sensors from waste heat, power, size and cost are the most important parameters. The efficiency is typically not of direct relevance for harvesting since the heat source itself is free. However, it is instructive to analyze the SOFHE's efficiency to identify areas of improvement. Here, we consider two types of efficiency: the cycle efficiency ( $W_{cycle}/Q_{in}$ ) and the engine efficiency ( $W_{net}/Q_{in}$ ). For all the operating temperatures tested, the cycle efficiency and the engine efficiency are less than 0.7% and 0.2% respectively. The Carnot efficiency of the cycle is at 2.1% considering  $T_C = 368$  K and  $T_H = 376$  K, which are the saturation temperature corresponding to the lowest and the highest pressure, respectively. The relative efficiency given by the ratio of the engine efficiency and the cycle efficiency to the Carnot efficiency is 10% and 30%, respectively. It should be noted that the real efficiency of the device is less than the engine efficiency presented here, since we neglected heat loss from the device as well as the sensible heat that is required to bring the liquid to the saturation temperature. The former depends on a detailed design of a SOFHE device and is beyond the scope here. The latter is found to be negligible compared to the latent heat of phase change. We can also prove this by idealizing the cycle as a Rankine cycle working between the maximum and minimum pressure equivalent to the real cycle for the SOFHE.

Therefore, the sensible heat and the vaporization enthalpy are equal to 35 kJ/kg and 2243 kJ/kg, respectively (1.6% of the enthalpy of vaporization). Dobson et al. [51] also neglected the sensible heat in the efficiency calculation of their PHP as a water pump.

### 3.3.4 Effect of operating and design parameters

#### 3.3.4.1 Heat source temperature

Figure 3-7 shows the thermodynamic cycles of the SOFHE at four different heat source temperatures,  $T_H$ , without load (at the highest length of the fiber discussed in the next section 3.4.2). We can see that increasing  $T_H$  leads to a broader thermodynamic cycle with a larger liquid plug motion amplitude, as presented in Table 3-1. This increase is due to the rise in the average phase change rate from  $728 \pm 11$  to  $1341 \pm 26$   $\mu\text{g/s}$  at  $T_H = 110$  and  $140$   $^\circ\text{C}$ , respectively. It is interesting to point out that, unlike increasing the load, which leads to a change in the shape of P-V cycles (Figure 3-4b), increasing  $T_H$  does not affect the shape of the cycle and the pressure phase with respect to the velocity. It only changes the amplitude of the cycle.

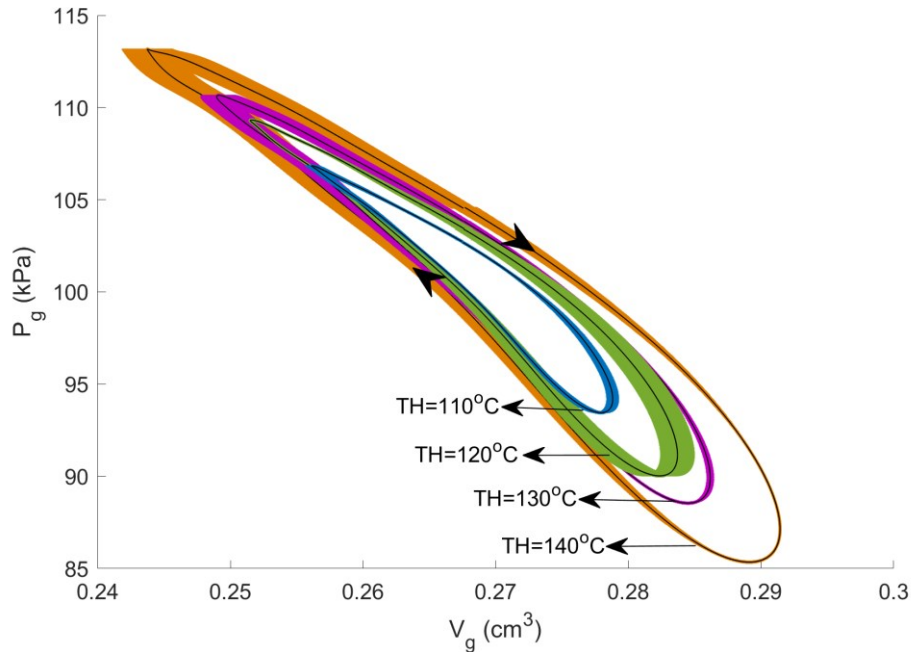


Figure 3-7 P-V cycle of SOFHE at different heat source temperatures  $T_H$  without load.

Table 3-1 Amplitude and phase change rate at different heat source temperatures  $T_H$ .

$T_H$ ( $^\circ\text{C}$ )	Amplitude (mm)
110	$7.2 \pm 0.3$
120	$10.3 \pm 0.4$
130	$11.8 \pm 0.5$
140	$15.1 \pm 0.6$

To see how increasing  $T_H$ , and consequently the P-V cycle, affects the generated mechanical power density, we also studied the system under different levels of the load at each temperature (Figure 3-8 Available mechanical power density (volume=  $3 \text{ cm}^3$ ) as a function of the load

coefficient at different  $T_H$  and loads. Dashed curves are fits to the data using the Tessier-Poirier et al. [112] model.). The data points are the experimental measurements and the dashed lines are the fitting. We fitted the experimental data with an expression for power derived by Tessier-Poirier et al. [112]. We introduced two parameters to fit the amplitude of the curves and the asymmetry to the experimental data. The good agreement between the experimental data and the prediction by the model confirms that the behavior they described is correct: the power follows an asymmetrical bell shape curve that crosses zero at the load of zero and the maximum. They also showed that the amplitude and the asymmetry of the power curves increase as the instability number ( $II$ ) increases. In these graphs, we increased  $T_H$  to increase the instability number. The maximum available mechanical power density at the different  $T_H$  is presented in Table 3-2. We observed a fourfold increase at the maximum available mechanical power density from 126 to 509  $\mu\text{W}/\text{cm}^3$  when going from  $T_H = 110^\circ\text{C}$  to  $140^\circ\text{C}$ .

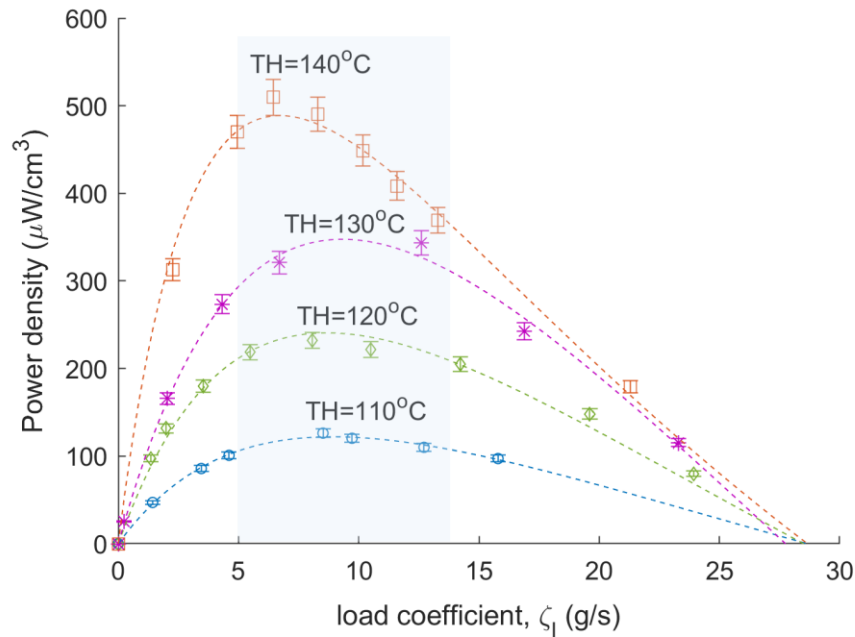


Figure 3-8 Available mechanical power density (volume= 3  $\text{cm}^3$ ) as a function of the load coefficient at different  $T_H$  and loads. Dashed curves are fits to the data using the Tessier-Poirier et al. [112] model.

Table 3-2 Maximum power density at different heat source temperatures  $T_H$ .

$T_H$ ( $^\circ\text{C}$ )	Maximum power density ( $\mu\text{W}/\text{cm}^3$ )
110	$126 \pm 5$
120	$232 \pm 9$
130	$343 \pm 13$
140	$509 \pm 20$

### 3.3.4.2 Phase change enhancement

To explore the potential of the engine, we monitored the engine power density while enhancing the phase change rate by varying the length of the fiber as a wicking structure inside the evaporator ( $L_{fiber}$ ). The shortest length of the fiber corresponds to a threshold below which the oscillations stop (instability number less than 1 [48]), while the longest one leads to a saturation regime where there is no change in the oscillation amplitude with further increase of the fiber

length in the evaporator. This determines an effective range in which we change  $L_{fiber}$ . The P-V cycles and the phase change rate corresponding to each cycle are plotted in Figure 3-9 at  $T_H = 110\text{ }^\circ\text{C}$ . We observed a significant increase in the average phase change rate from 93 to 580  $\mu\text{g/s}$  by varying  $L_{fiber}$  within the effective range (from 1.7 cm to 4.5 cm). This augmentation in the average phase change rate increases the size of the P-V cycles, which means generating more  $W_{net}$ , as shown in Figure 3-10. This in turn augments the available mechanical power density by 30 times from 3  $\mu\text{W/cm}^3$  to 98  $\mu\text{W/cm}^3$ . The reason for the dramatic increase in the slope at the beginning of the graph for power density is the sensitivity of the phase change rate to the presence of the capillary fiber. When  $L_{fiber}$  is less than 1.5 cm, we have no oscillations, while by changing  $L_{fiber}$  by a few millimeters it starts oscillating. At small  $L_{fiber}$ , the phase change rate experiences an increase of 220% for only 23% of increase in  $L_{fiber}$ , while this increase drops to 48% at a 50% increase of  $L_{fiber}$  at higher  $L_{fiber}$  (from 3 to 4.5 cm).

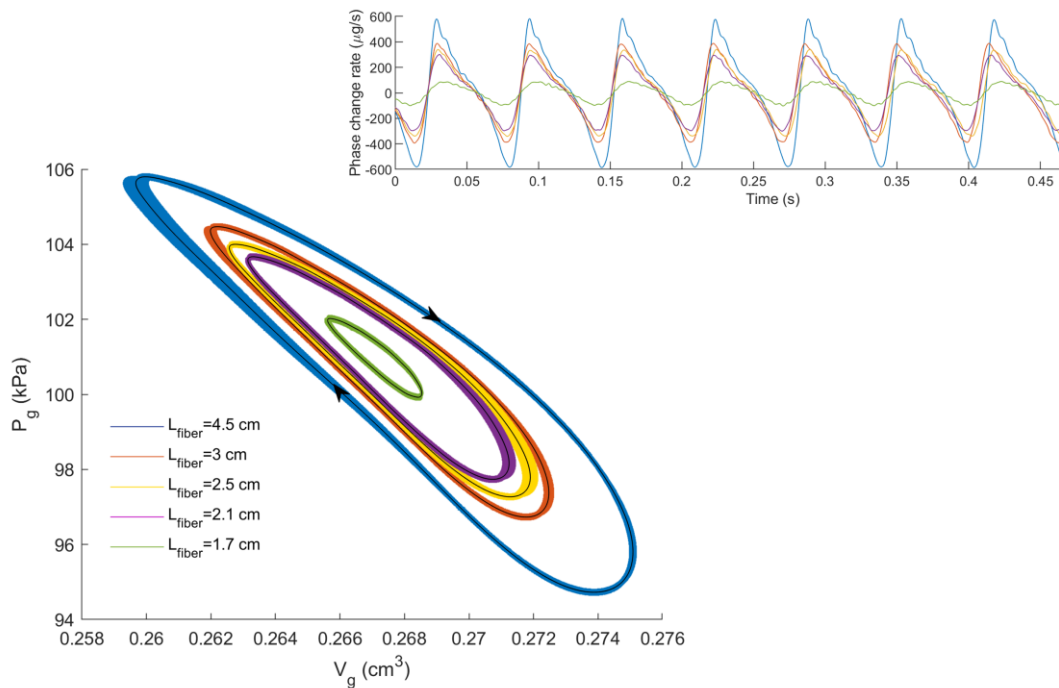


Figure 3-9 P-V cycles at different fiber lengths inside the evaporator ( $L_{fiber}$ ) at  $T_H = 110\text{ }^\circ\text{C}$  at a fixed load. The phase change rate corresponding to each cycle as a function of time is shown in the insert.

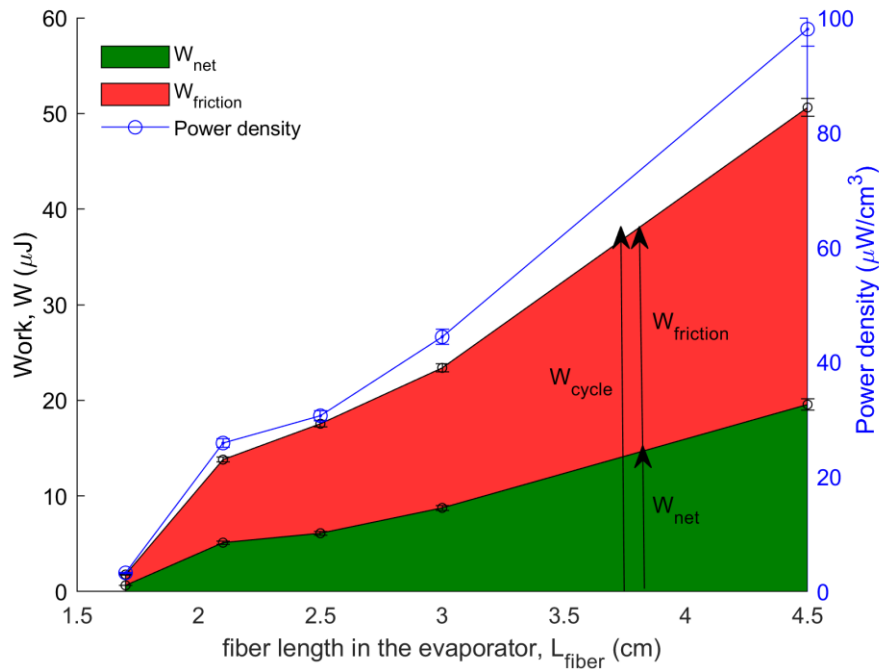


Figure 3-10 Work (friction and net) and power density at different fiber lengths inside the evaporator ( $L_{fiber}$ ) under a fixed load at  $T_H=110$  °C.

Research findings shows that self-oscillations are difficult to achieve with water as the working fluid [42]. To overcome this challenge, one can add wicking structures, including the glass fiber used here [48,105]. Apart from the thin film evaporation behind the meniscus, the presence of the fiber creates two corners with the glass tube (Figure 3-11), acting as angular capillaries pumping liquid from the liquid plug towards the evaporator. A long thin film therefore forms along the fiber, which facilitates the evaporation rate by decreasing the thermal resistance in the liquid film. This allows the oscillations to occur at a lower  $T_H$ . Different types of corners such as the interior corners of a square tube can play a similar role to that of the fiber in the evaporation rate enhancement [80,81], consequently reaching start-up and sustainable oscillation.

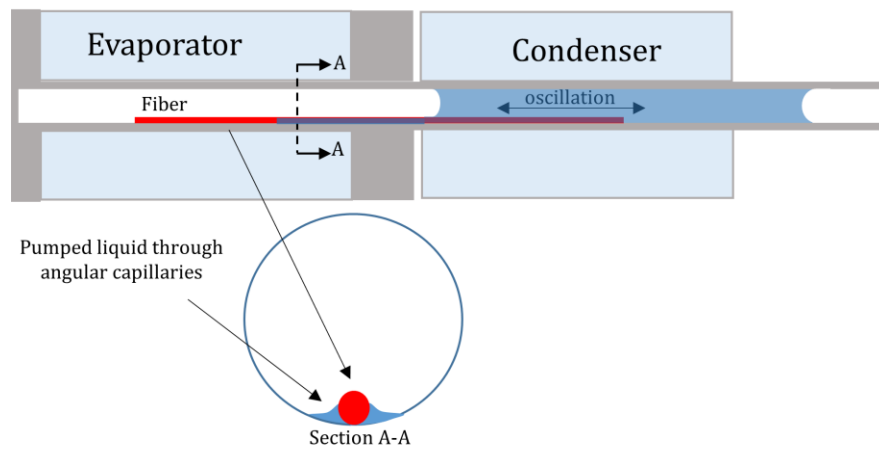


Figure 3-11 Schematic view of the inserted fiber acting as a wicking structure inside the evaporator.

### 3.3.4.3 Liquid length

This section describes the effect of the length of the liquid plug ( $L_{liq}$ ). We set the mechanical load near the optimum amount,  $T_H = 110$  °C,  $L_{fiber} = 4$  cm, and then decreased  $L_{liq}$  from 22 cm to 14 cm (the lowest possible length with respect to the current set-up limitation). Interestingly, there is no change in the  $W_{cycle}$  (Table 3-3), while the friction loss decreases by about 16%. This leads to a rise of 35% in the  $W_{net}$ . Reducing  $L_{liq}$  also has the benefit of increasing the frequency by about 22%. Considering the decrease in the volume, the mechanical power density experienced a twofold increase as a whole.

Table 3-3 Comparison of cycle work, friction loss, and net work at two different lengths of the liquid plug.

$L_{liq}$ (cm)	Amplitude (mm)	Frequency (Hz)	$W_{cycle}$ ( $\mu\text{J}$ )	$W_{friction}$ ( $\mu\text{J}$ )	$W_{net}$ ( $\mu\text{J}$ )	Power density ( $\mu\text{W}/\text{cm}^3$ )
22.0	$7.1 \pm 0.3$	13.2	$91 \pm 4$	$63 \pm 3$	$28 \pm 1$	$97 \pm 3$
14.5	$6.8 \pm 0.3$	16.1	$92 \pm 4$	$53 \pm 2$	$39 \pm 2$	$217 \pm 8$

## 3.4 Discussion

Understanding the SOFHE's thermodynamic cycle helps figure out how to design a more desirable engine. As shown in Figure 3-12 (left), evaporation mostly happens when the cycle is in the compression process, which is not the right timing. As Tessier-Poirier et al. [48] discussed, the maximum work is done when the pressure force from the phase change,  $F_m$ , is perfectly in phase with the velocity, hence when it becomes in quadrature with the position. We can see the phase of  $\dot{m}_g$ , and  $F_m$  with respect to the velocity for the SOFHE in Figure 3-12 (right). Ideally,  $F_m$  would be in phase with the velocity, which is not the case here.  $F_m$  itself is in quadrature with  $\dot{m}_g$  since it is a result of the pressure change from the evaporation–condensation. We can therefore notice that the evaporation–condensation needs to be modified in terms of its phase with respect to the position, to become completely out of phase with the position. This would bring  $F_m$  in phase with the velocity and maximize the available mechanical work. Besides, as discussed in section 3.3.4.2, changing the amplitude of evaporation–condensation has a significant effect on the available mechanical work.

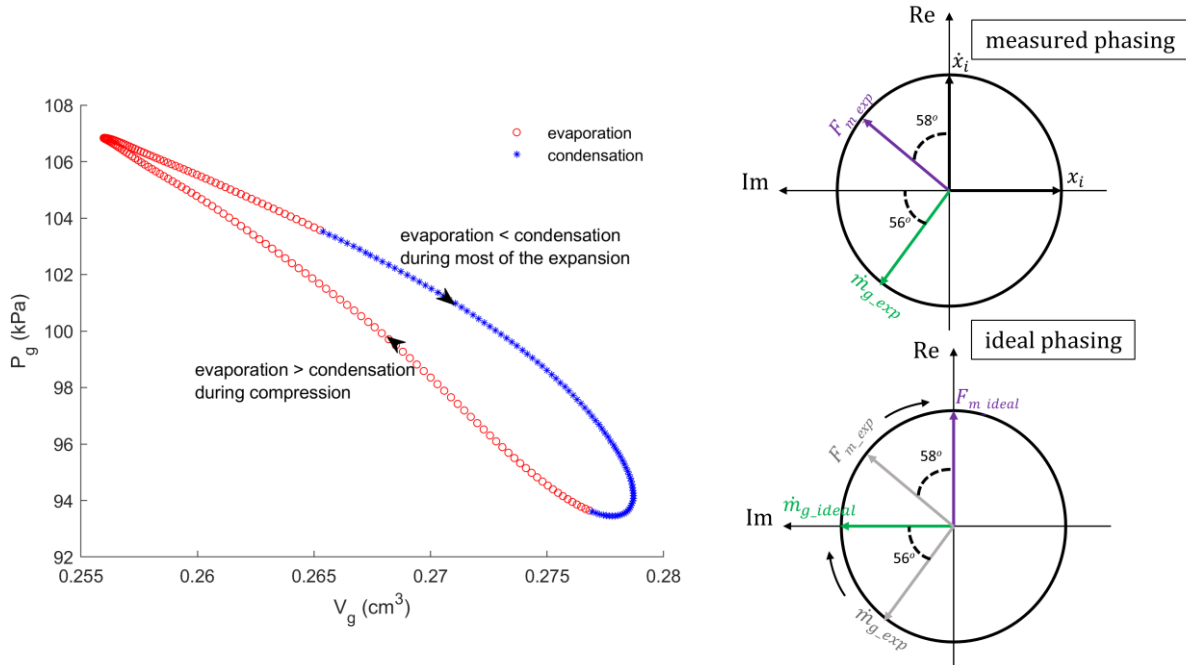


Figure 3-12 The measured thermodynamic cycle of the SOFHE showing evaporation and condensation processes (left) and the corresponding phase diagram (right): measured phasing (top) and ideal phasing for maximum  $W_{net}$  (bottom).

It is interesting that the optimum range of mechanical power density is at the amplitude ratio ( $x_i/x_{i\_max}$ ) of 0.5 to 0.7. This useful observation provides guidance for designing a more compatible transducer for the SOFHE that works more efficiently in the optimum amplitude of the heat engine. By doing so, we can transfer as much energy as possible from the engine to the transducer by matching the impedance between the two. The vertical green band in Figure 3-8 shows the range for an optimum load coefficient for the transducer. One can vary the load coefficient three times (from 5 to 15 g/s) and still remain within  $\pm 10\%$  of the optimum power density as  $T_H$  increases.

We can also conclude from the maximum mechanical power densities (between 100 and 500  $\mu\text{W}/\text{cm}^3$ ) that the SOFHE can power a wide range of wireless sensors (requiring 10's of  $\mu\text{W}$ ) even with a transducer with a 10% mechanical-to-electrical conversion efficiency. In addition, section 3.4.3 showed the positive impact of decreasing the liquid plug length,  $L_{liq}$ , on the mechanical power density by decreasing the friction loss, reducing the volume as well as increasing the frequency. This suggests that miniaturization of the SOFHE is a promising approach, in line with the compact size of power sources required for wireless sensors.

### 3.5 Conclusion

In this paper, we exploited the physics of a SB-PHP in a different concept as a self-oscillating fluidic heat engine (SOFHE) to produce work rather than heat transfer and presented its unique and unknown thermodynamic cycle as well as the generated work. We then took a step further and calculated the work that is dissipated through friction of the liquid plug to determine the net work that the SOFHE can provide to a purely damped electromechanical transducer. To show the potential of this cycle, we experimentally measured the mechanical power density at

different operating temperatures of the heat source. The research findings confirmed that the available mechanical power density by the SOFHE (hundreds of microwatts) is sufficient to fulfill a wide range of wireless sensors with power requirements of tens of microwatts. However, to show that our system still has much room for further enhancement, we varied two main design parameters to see how the mechanical power density varies. The first parameter was the fiber length in the evaporator, which had a critical impact on the average rate of phase change, which consequently increased the mechanical power density by 30 times. Decreasing the length of the liquid plug was the second design modification and improved the mechanical power density by decreasing the friction loss and volume as well as increasing the frequency. Overall, this study reveals that while the SOFHE suffers from a low efficiency, it has a great potential in terms of power density, a key metric for energy harvesting. Paths for further improvement are also proposed, such as controlling the phase change phasing with respect to the motion and miniaturization of the device. This, along with a continuing decrease in the power requirements of wireless sensor nodes, marks the SOFHE as a promising field of research for thermal energy harvesting.

### **Acknowledgements**

We acknowledge financial support from NSERC through the Scholarship and Discovery Programs (Canada). We are also thankful to Alexandre Juneau Fecteau for productive discussions.



## Chapter 4

# How phase-change mechanism affects the SOFHE performance?

**Authors and affiliation:** Nooshin Karami<sup>1,2</sup>, Albert Tessier-Poirier<sup>1,2</sup>, Etienne Léveillé<sup>1,2</sup>, Luc G. Fréchette<sup>1,2</sup>

<sup>1</sup>Institut Interdisciplinaire d'Innovation Technologique (3IT), Université de Sherbrooke, Sherbrooke, QC, Canada

<sup>2</sup>Laboratoire Nanotechnologies Nanosystèmes (LN2), CNRS UMI-3463, Université de Sherbrooke, Canada

**Submission date:** 24-03-2023.

**Acceptance date:** 18-05-2023.

**Publication date:** 25-05-2023.

**Status:** final version is published.

**Journal:** International Journal of Heat and Mass Transfer.

**Reference:** Karami N, Tessier-Poirier A, Léveillé E, Fréchette LG. Importance of phase change timing in a self-sustained oscillatory flow. *Int J Heat Mass Transf* 2023;213:124327. <https://doi.org/10.1016/j.ijheatmasstransfer.2023.124327>.

**Title:** Importance of Phase Change Timing in a Self-Sustained Oscillatory Flow.

**Titre français:** Importance de la synchronisation du changement de phase dans un écoulement oscillatoire auto-entretenu.

**Contribution statement:** I carried out all the experimental and theoretical work presented in this article. The co-authors provided advice, suggestions, and revision during the research and writing process.

**Abstract:** This paper experimentally shows the effect of phase change timing on the oscillation amplitude for a vapor bubble-liquid plug exposed to a thermal gradient in a capillary tube. The case studied is the basic unit of pulsating heat pipes (PHP) and self-oscillating fluidic heat engines (SOFHE), implemented here by heating a tube at its closed end (evaporator) and cooling it at the opposite open end (condenser). A vapor bubble is formed at the closed end, trapped by a liquid plug. Under certain conditions, the liquid plug starts to oscillate due to periodic evaporation-condensation in the vapor bubble. The temperature, pressure, and volume of the vapor bubble are measured to calculate the phase change rate, for two different working fluids (water and ethanol). We first show a regime where the liquid plug's oscillations exhibit a beating phenomenon, where the amplitude periodically increases and dies down due to the slow dryout of the thin film left behind the meniscus. We then use a simple approach to manipulate the phase change using a wicking fiber inserted in the tube. This modification yields stable oscillations with constant amplitude due to a significant increase in the phase change rate. For ethanol, no

oscillations are observed without the fiber. Adding the wicking fiber leads to oscillations with a different phase change profile than with water. To maximize work done by phase change on the liquid plug, the phase change force needs to be optimally in phase with velocity. To evaluate this phase angle, a new tool is proposed that is based on integrating the product of the phase change force and velocity over a cycle at different phase angles. By doing so, the maximum theoretical work at ideal phase angle is calculated. It is used to define Phase Change Effectiveness as a dimensionless number ( $\phi$ ) that equals the ratio of the phase change work to the maximum theoretical work. The phase change profile for water has a  $\phi$  number of 0.56, showing room for further improvement, while ethanol shows an effective phase change profile with a  $\phi$  number of 0.99. For a lower maximum work, a more effective phase change profile yields a higher oscillation amplitude, which is at 10.2mm for ethanol compared to 7.2mm for water. This study opens a new path towards engineering the phase change to optimize the oscillations in pulsating heat pipes and self-oscillating fluidic heat engines.

**Keywords:** self-oscillation, thin film, evaporation-condensation, phase angle, wicking fiber, phase change effectiveness.

**Résumé français:** Cet article montre expérimentalement l'effet de la synchronisation du changement de phase sur l'amplitude de l'oscillation d'un bouchon vapeur-liquide exposé à un gradient thermique dans un tube capillaire. Le cas étudié est l'unité de base des caloducs pulsés (PHP) et des moteurs thermiques fluidiques auto-oscillants, mis en œuvre ici en chauffant un tube à son extrémité fermée (évaporateur) et en le refroidissant à l'extrémité ouverte opposée (condenseur). Une bulle de vapeur se forme à l'extrémité fermée, piégée par un bouchon liquide. Dans certaines conditions, le bouchon liquide commence à osciller en raison de l'évaporation-condensation périodique dans la bulle de vapeur. La température, la pression et le volume de la bulle de vapeur sont mesurés pour calculer le taux de changement de phase, pour deux fluides de travail différents (eau et éthanol). Nous montrons d'abord un régime où les oscillations du bouchon liquide présentent un phénomène de battement, où l'amplitude augmente périodiquement et s'éteint en raison du lent assèchement de la fine pellicule laissée derrière le ménisque. Nous utilisons ensuite une approche simple pour manipuler le changement de phase à l'aide d'une fibre insérée dans le tube. Cette modification produit des oscillations stables d'amplitude constante en raison d'une augmentation significative du taux de changement de phase. Pour l'éthanol, aucune oscillation n'est observée sans la fibre. L'ajout de la fibre entraîne des oscillations avec un profil de changement de phase différent de celui de l'eau. Pour maximiser le travail effectué par le changement de phase sur le bouchon liquide, la force de changement de phase doit être en phase optimale avec la vitesse. Pour évaluer cet angle de phase, un nouvel outil est proposé, basé sur l'intégration du produit de la force de changement de phase et de la vitesse sur un cycle à différents angles de phase. Ce faisant, le travail théorique maximal à l'angle de phase idéal est calculé. Il est utilisé pour définir l'efficacité du changement de phase comme un nombre sans dimension ( $\phi$ ) qui est égal au rapport entre le travail de changement de phase et le travail théorique maximal. Le profil de changement de phase pour l'eau a un nombre  $\phi$  de 0,56, ce qui montre qu'il peut encore être amélioré, tandis que l'éthanol présente un profil de changement de phase efficace avec un nombre  $\phi$  de 0,99. Pour un travail maximal plus faible, un profil de changement de phase plus efficace produit une amplitude d'oscillation plus élevée, qui est de 10,2 mm pour l'éthanol contre 7,2 mm pour l'eau. Cette étude ouvre une nouvelle voie vers l'ingénierie du changement de phase afin d'optimiser les oscillations dans les caloducs pulsés et les moteurs thermiques fluidiques auto-oscillants.

**Mots clés:** auto-oscillation, film mince, évaporation-condensation, angle de phase, mèche, efficacité du changement de phase.

## 4.1 Introduction

The thermally induced oscillatory plug flow is found in pulsating heat pipes (PHPs) for thermal management [38,113,114], in self-oscillating fluidic heat engines (SOFHEs) for thermal energy harvesting [105,109,115,116], and in pumping applications [51,117]. The unit cell of these devices is a vapor bubble-liquid plug enclosed in a capillary tube called single-branch PHP that is exposed to a thermal gradient [40–43,50,51,118,119]. To form this unit cell, we simply need a capillary tube filled with a working fluid that is partially heated at a closed end to form the vapor bubble (evaporator section) and cooled at the opposite end (condenser section) that can be open (atmospheric pressure) or closed by connecting it to a reservoir. By perturbing the equilibrium, by increasing the evaporator temperature or decreasing the external pressure for instance, the system can become unstable and oscillations start. In pulsating heat pipe applications, the oscillating motion is used to carry heat along the tube. In heat engine applications, however, the pressure pulsations are leveraged instead to actuate a transducer for electric power generation or for pumping. Therefore, the working principles of these devices are similar but their application distinguishes them from one another. To optimize PHPs performance (Figure 4-1 left), the output heat has to be maximized while it must be minimized for SOFHEs (Figure 4-1 right) due to efficiency concerns.

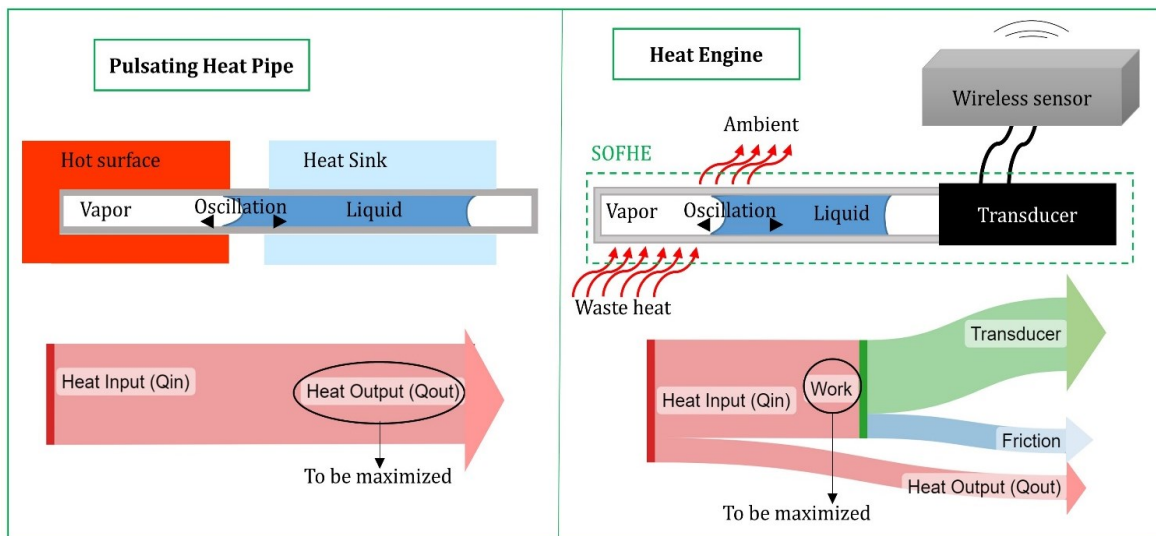


Figure 4-1 PHP's application to cool a hot surface and its equivalent Sankey diagram (left), SOFHE's application as a thermal energy harvester and its Sankey diagram (right) [120].

This vapor bubble coupled with the liquid plug is modeled as a viscous damped spring-mass system [43,57,108,121]. To understand the instability mechanism that leads to oscillations, Tessier-Poirier et al. [48] proposed a dimensionless number called the Instability number that consists of the ratio of phase change force to friction force, deduced from analytical model of the system. For an Instability number greater than one, which is when the phase change force is greater than the viscous losses, the system becomes unstable and oscillations start. The amplitude of oscillation grows due to the phase-change acting as a positive feedback and then stabilizes due to the nonlinearities that exist in the system [122]. These nonlinearities have

different sources, including the thermal gradient, the phase change mechanism, geometrical restrictions, etc. They also proposed an analytical expression for amplitude of oscillation that is a function of a phase change coefficient. It is shown that the phase change coefficient is a bifurcation parameter that needs to be larger than a threshold to make the system unstable for startup. By further increasing of the phase change coefficient, the amplitude increases. Therefore, the phase change plays a key role in the oscillation startup and the amplitude growth which in turn decreases thermal resistance in PHPs [123] and increases output power in SOFHEs [115].

This phase change is generally produced from a thin liquid film left behind the oscillating meniscus that deeply penetrates inside the evaporator [38,40–44]. For the meniscus penetration, it is required to find the correct combination of reservoir pressure (external pressure), evaporator temperature and condenser temperature. Rao et al. [124] successfully obtained oscillations for FC72 and pentane while with de-ionized water and ethanol, they were unable to find any combination of reservoir pressure (0.2 to 1 bar), evaporator temperature (-10 to 120°C) and condenser temperature (-10 to 120°C) to make oscillations start. It has been also reported that start up is difficult to achieve with water and ethanol even in multi-branch PHPs [20–22]. To facilitate startup or intensify the phase change in PHPs, surface modifications have been proposed, including reentrant cavities [123], coating the inner tube wall with micro particles [127], adding wicking structures like micro grooves [82] and ultra-sharp grooves [83]. To justify the effect of these modifications, only thermal resistance of PHPs was evaluated. However, there is no measurement to justify how these modifications affect the phase change or a method to evaluate the effectiveness of the phase change mechanism.

In this paper, we study how surface modifications and choice of the working fluid impact the phase-change, which in turn affects the oscillation amplitude. Firstly, phase change rate (the rate of change of mass of vapor) is experimentally measured in a thermally self-sustained oscillatory flow with two different phase change mechanisms and working fluids (water and ethanol). The first mechanism is the phase change from a thin film left behind the oscillating meniscus and the second mechanism is using a wicking fiber. Secondly, a method is proposed to study the effectiveness of the phase change from both mechanisms and compare it for the two working fluids. The method is based on characterizing the phase angle between the phase change rate and displacement that consequently defines the phase angle between the phase change force and velocity. We show that the work done by the phase change is maximized when the phase change force is in phase with velocity. Therefore, it is suggested that not only the magnitude of phase change rate is relevant, but also its phasing with the meniscus motion. Finally, to evaluate the effectiveness of the phase change profile, a dimensionless number called Phase Change Effectiveness (PCE) is introduced that equals the ratio of the work done by the phase change to the maximum work where the force is perfectly in phase with velocity.

## 4.2 Methodology

### 4.2.1 Experimental set-up

The experimental setup used to measure the rate of change of mass of vapor (phase change rate) in an oscillatory plug flow is shown in Figure 4-2. As shown in the exploded view (Figure 4-2a), a hot block (heated with a cartridge heater) and a cold block (cooled by a thermostatic bath) in aluminum are designed to form the evaporator and condenser, respectively. A glass capillary tube ( $D_{in}=2$  mm,  $D_{out}=4$  mm) is  $O_2$  plasma treated for cleaning and hydrophilicity at a power

100W for 2 min. Tube supports with a semi-circular groove are designed to hold the glass tube. The tube supports are clamped to the blocks using an L-shape clamp and thermal paste. We then place the glass tube inside the groove, with a layer of conductive thermal paste to reduce the contact thermal resistance. The tube is then filled with a working fluid (deionized water or ethanol) and fixed using Peek clamps. The degassing of the water is through one-step boiling of deionized water and a syringe is used to directly take the boiling water from the beaker. To fill the glass tube, the syringe is then connected to the tube using a plastic connection. The blocks (evaporator and condenser) are separated by a small distance (4mm) creating a so-called adiabatic section. A small hole is designed in the tube supports to embed thermocouples to control the evaporator ( $T_H$ ) and condenser temperature ( $T_C$ ). The length of evaporator ( $L_v$ ) and condenser ( $L_l$ ) can be adjusted between 1 and 10cm using different combinations of tube supports. The heated end of the tube is closed with a pressure sensor (PX26, OMEGA Engineering) to measure pressure change in the vapor bubble ( $P_v$ ) and the cooled end is open to the ambient air (external pressure,  $P_{v0}=101.3$  kPa). A high-speed camera (PCO. 1200 hs) is used to record the position ( $x$ ) of the oscillating meniscus for volume measurement ( $V_v$ ). The pressure and position measurements are synchronized using a data acquisition board USB-1608GX. To play with the phase change, a polyimide coated glass fiber (capillary with closed ends, Polymicro, external diameter of 350 $\mu$ m) is inserted inside the tube from condenser side (open end) all the way into the evaporator zone. The fiber forms capillary corners with the glass tube and pumps liquid from the liquid plug towards the evaporator zone [120] (see appendix A for more details).

To conduct a test, the condenser temperature is set at 20 $^{\circ}$ C and the heating process starts. A vapor bubble forms and grows lengthwise until the liquid meniscus reaches an equilibrium point that is usually located in the adiabatic zone. By increasing the heater temperature further, the system becomes unstable and oscillations start. The phase change, that is the change of mass of vapor ( $m_v$ ) due to evaporation-condensation, is calculated using the ideal gas law [120].

$$m_v = \frac{P_v V_v}{RT_v} = \frac{P_v (x + L_{v0}) A}{RT_v} \quad (4-1)$$

Where  $R$  is the specific gas constant,  $L_{v0}$  is the length of vapor bubble at equilibrium,  $A$  is the cross-section area of the tube, and  $T_v$  is the vapor temperature, which is assumed to be constant and equal to the evaporator wall temperature ( $T_H$ ). This assumption is valid since it is shown by Gully et al. [100] that the vapor is superheated and its temperature fluctuates  $\pm 1$   $^{\circ}$ C from the wall temperature. Besides, as shown by Rao et al. [40], even if the vapor temperature deviates  $\pm 10$   $^{\circ}$ C from the wall temperature, this leads to only  $\pm 3\%$  error in the mass of vapor which means the calculated mass of vapor is still valid. For the following test, we adjust  $L_v$  and  $L_l$  at 6cm and 8cm, respectively.

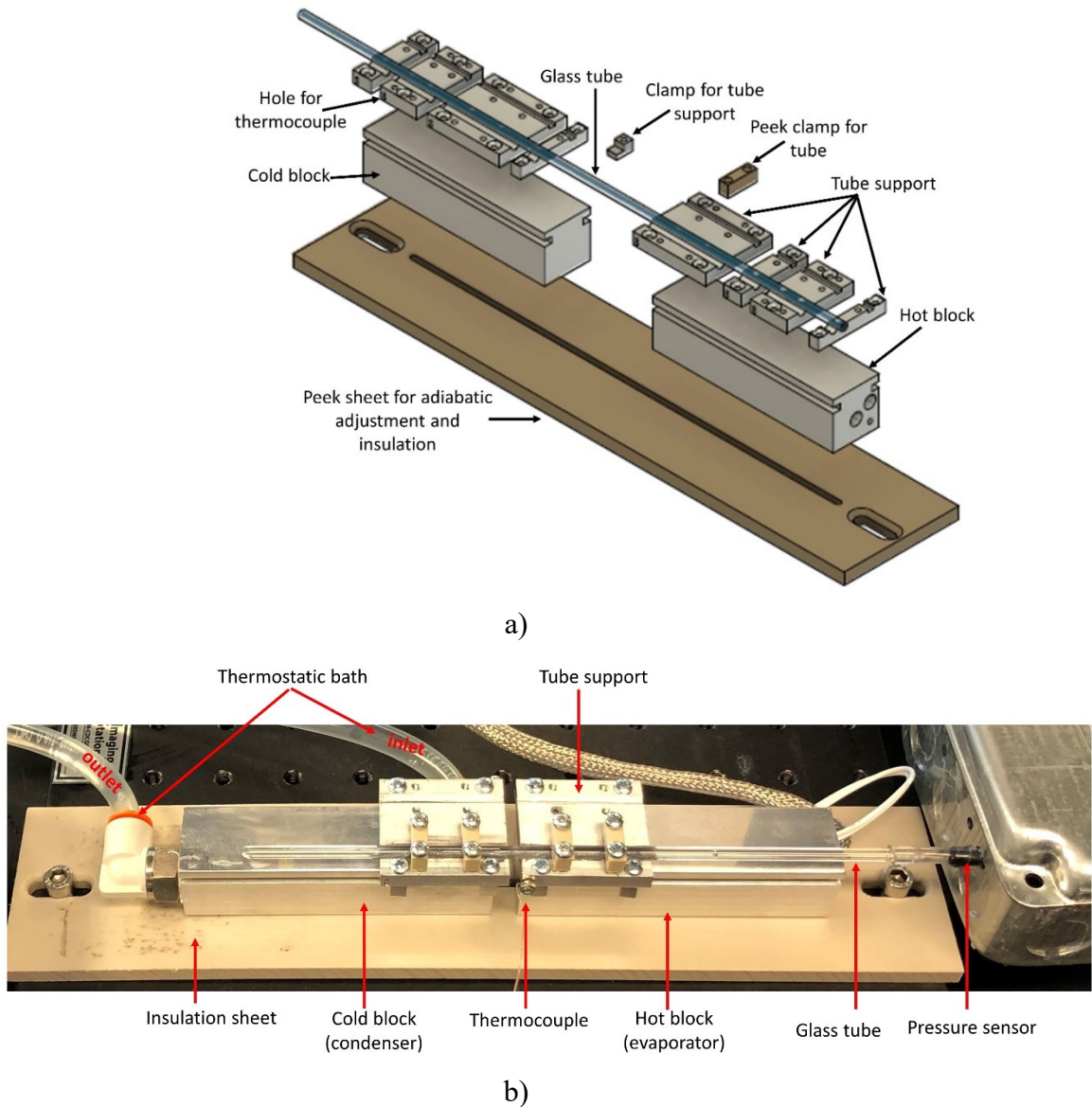


Figure 4-2 The test setup to measure phase change rate (evaporation-condensation) in a thermally self-induced oscillatory flow inside a capillary tube: a) exploded view, b) real top view.

## 4.3 Results

### 4.3.1 Thin film phase change: beating oscillations

Figure 4-3 shows the measured meniscus displacement and phase change rate as a function of time for water. Regarding the blue curve for meniscus displacement, negative and positive values mean positions near the evaporator and condenser, respectively. The phase change rate (green curve) is the net evaporation-condensation rate. It should be noted that both evaporation and condensation can occur simultaneously at different locations within the vapor bubble since it spans zones with different wall temperatures. A negative value means net condensation (more condensation than evaporation) and a positive value means net evaporation. One can observe oscillations with a periodic sudden increase in amplitude followed by a slow decay. The recorded video during oscillations shows a thin film that is left behind the meniscus. It was

observed that the oscillations last as long as there is the thin film to feed the evaporation. When the thin film disappears, the oscillations stop and the meniscus starts penetrating inside the evaporator. This coincides with the negative phase change rate shown in the green curve. When the meniscus sweeps a certain length in the evaporator, the evaporation rate exceeds the condensation rate, the meniscus starts to move towards the condenser and the cycle repeats. The liquid film strongly contributes to the evaporation since it is thin with a low thermal resistance. We could not observe any startup for ethanol as the working fluid.

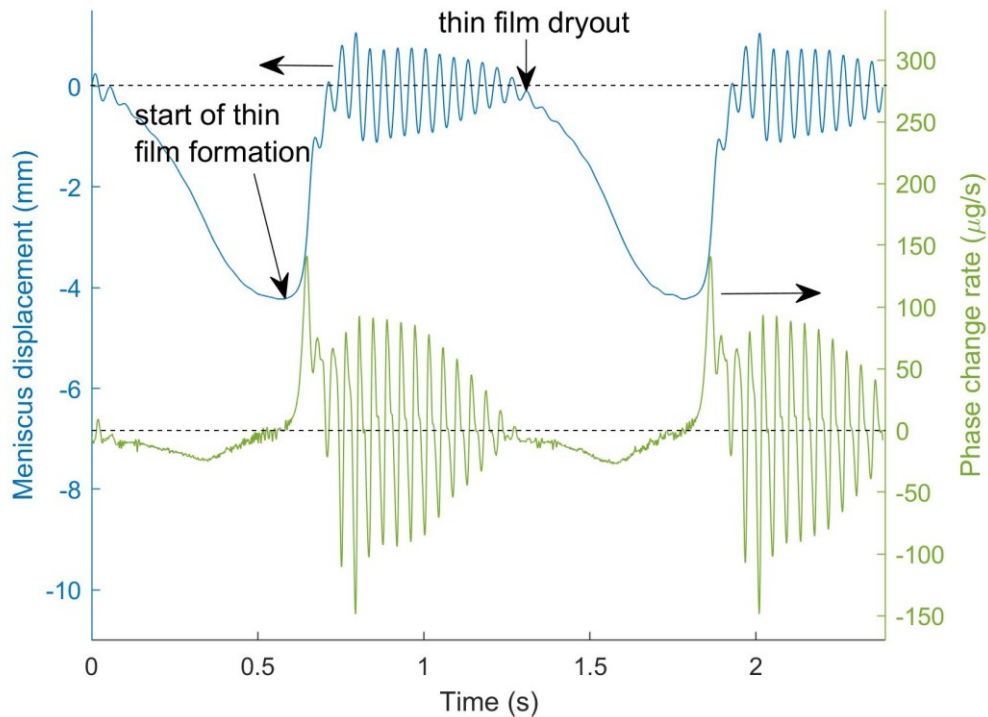


Figure 4-3 Meniscus displacement and phase change rate for water showing periodic oscillations resulting from dryout of the thin liquid film left behind the meniscus.

The depth of meniscus penetration inside the evaporator is a function of evaporator temperature. As the pressure signal shows in Figure 4-4<sup>1</sup>, at lower evaporator temperature (110 °C), oscillations have higher amplitude and last longer compared to the higher temperature (140 °C). This is because the meniscus sweeps a longer distance of the evaporator and hence, it leaves a longer film in the evaporator while receding. As the evaporator temperature increases, the meniscus penetrates less and less inside the evaporator, which means leaving a shorter thin film and consequently less evaporation, so shorter periods.

<sup>1</sup> The reason why the pressure signal is used instead of the position is that the meniscus displacement is beyond the camera access at lower temperature. The periodic patterns for the position and pressure signal are identical.

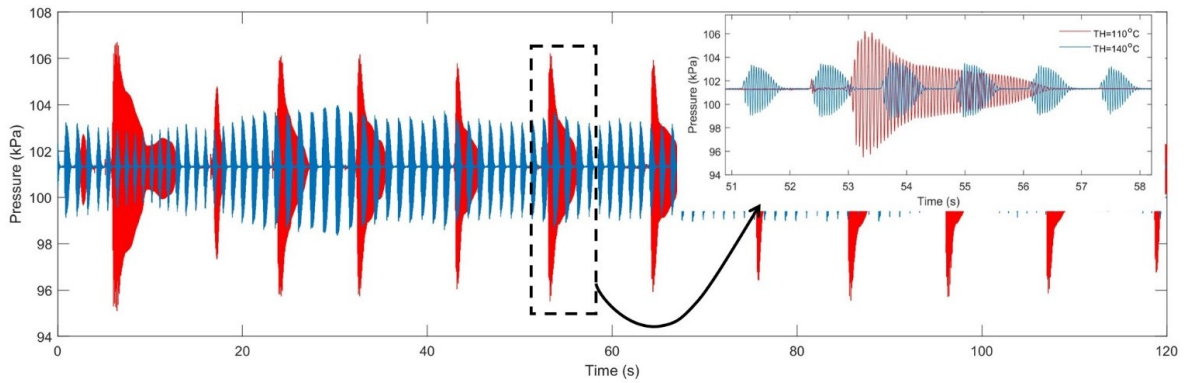


Figure 4-4 The measured pressure at two different evaporator temperatures, with a magnified inset showing higher pressure amplitude at lower temperature resulting from longer depth of meniscus penetration inside the evaporator.

### 4.3.2 Modified phase change by wicking fiber: a method for stable oscillations

To enhance the phase change, a wicking fiber is inserted inside the tube, extending from the condenser zone into the evaporator zone. The fiber forms corners with the inner wall of the glass tube and is in contact with the liquid plug so it can pump liquid towards the evaporator zone. This increases the thin film length for evaporation and also makes the length of the film independent of the oscillation amplitude. As shown in Figure 4-5, this capillary action forms a thin liquid film around the fiber with a long triple point line and interfacial surface area that are favorable for evaporation. The effect of adding fiber is explained more in details in our previous study [120]. In the presence of the wicking fiber, the meniscus barely touches the evaporator. It mostly oscillates in the adiabatic zone and the condenser. This suggests that the thin film formed through capillary action mainly contributes the evaporation.

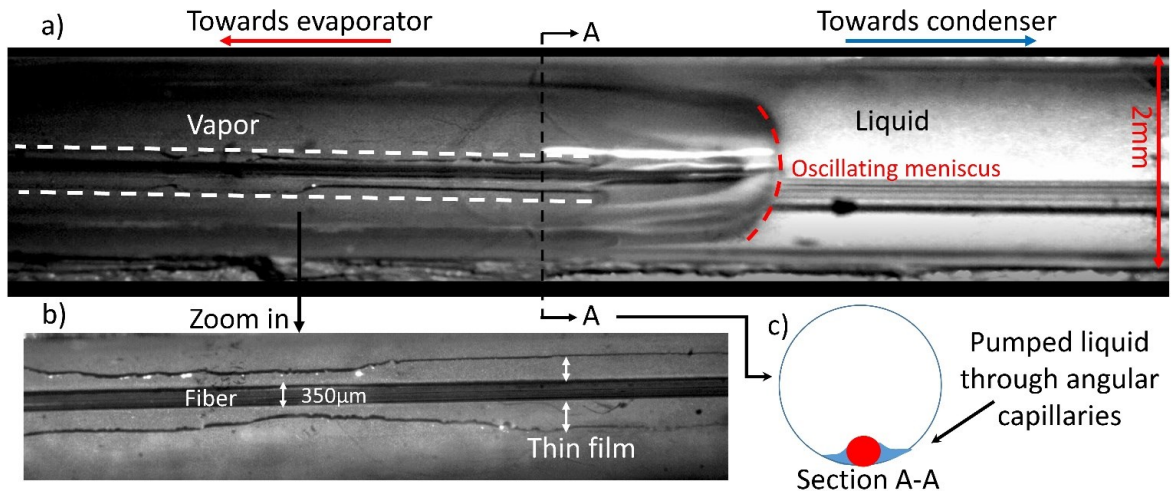
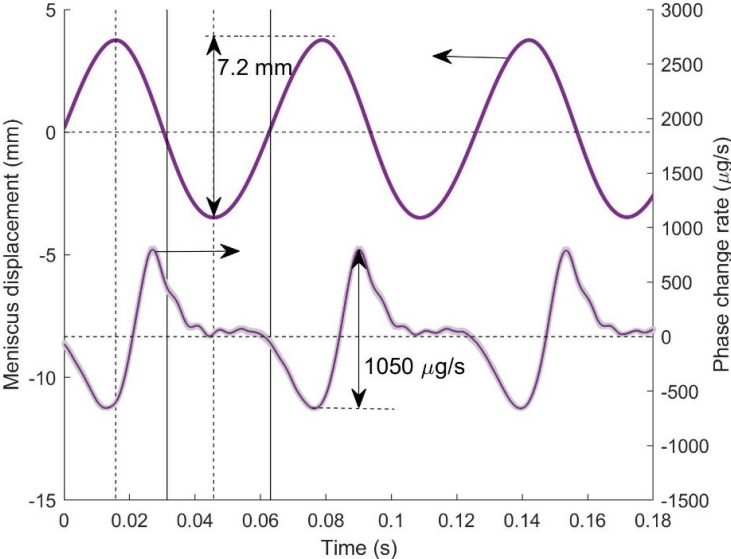


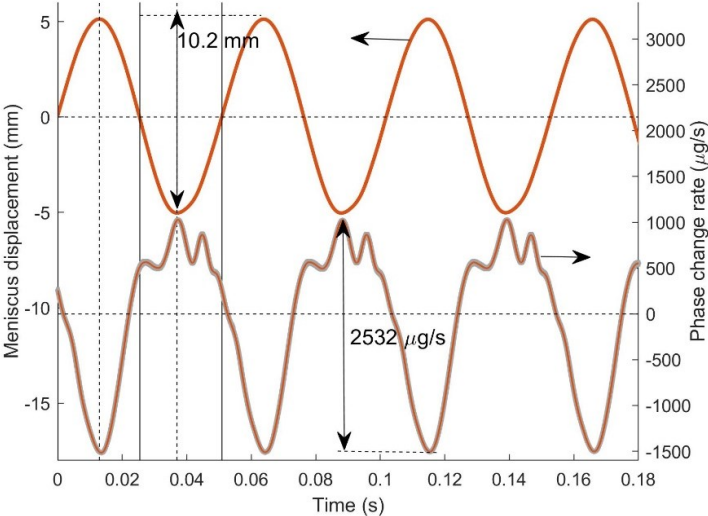
Figure 4-5 A frame of the recorded video during oscillations presenting: a) top view of the vapor, liquid, oscillating meniscus, fiber, and the thin film b) magnification of the thin liquid film around the fiber (the zone specified with white dashed lines) c) the cross-section schematic of the thin film formed by capillary action through the corners between the inner wall of the glass tube and the fiber.

Figure 4-6 a presents the measured meniscus displacement and phase change rate for water in the presence of the wicking fiber. Adding the fiber significantly changes the stability of the

oscillations and yields stable oscillations with a constant amplitude and unique frequency compared to the system without a fiber shown in Figure 4-3. The amplitude of the phase change rate significantly increased from around 200  $\mu\text{g/s}$  without the wicking fiber to 1050  $\mu\text{g/s}$  with the wicking fiber. The capillary action through the formed corners between the fiber and the tube inner wall constantly pumps liquid towards the evaporator and prevents the oscillations from decaying. The thin film does not dryout as the capillary pumping is able to replenish the evaporated liquid. Figure 4-6 b is for ethanol that did not show any start up without the fiber but now does with the fiber. In the presence of the fiber, the mean position of the meniscus is completely pushed into the condenser while with water it is placed in the adiabatic zone.



a) Water



b) Ethanol

Figure 4-6 Meniscus displacement and phase change rate as a function of time in the presence of the wicking fiber for a) water b) ethanol.

### 4.3.3 Phase change profile

This section is to better show the difference in phase change profiles for different mechanisms and working fluids and to compare the profiles with an ideal theoretical one that will be discussed in section 4.4.2. The phase change profile is the graph of net evaporation-condensation rate as a function of displacement. The phase change profile for water (without the fiber) showing beating oscillations is presented in Figure 4-7 with an inset showing the cycles of the corresponding profiles. As the phase change rate decreases due to the thin film dryout, the oscillation amplitude decreases, which corresponds to shrinking phase change profiles. The phase change profiles for stable oscillations in the presence of the wicking fiber for water and ethanol is plotted in Figure 4-8. The two working fluids show different phase change profiles. This could be explained by the fact that for ethanol, the thin film left behind the meniscus experiences a more uniform temperature profile since the mean position of the meniscus is in the condenser where we have a fixed temperature boundary condition. However, the thin film for water is more affected by the temperature fluctuations since the mean position of the meniscus is placed in the adiabatic section that could lead to a higher hysteresis in the phase change profile.

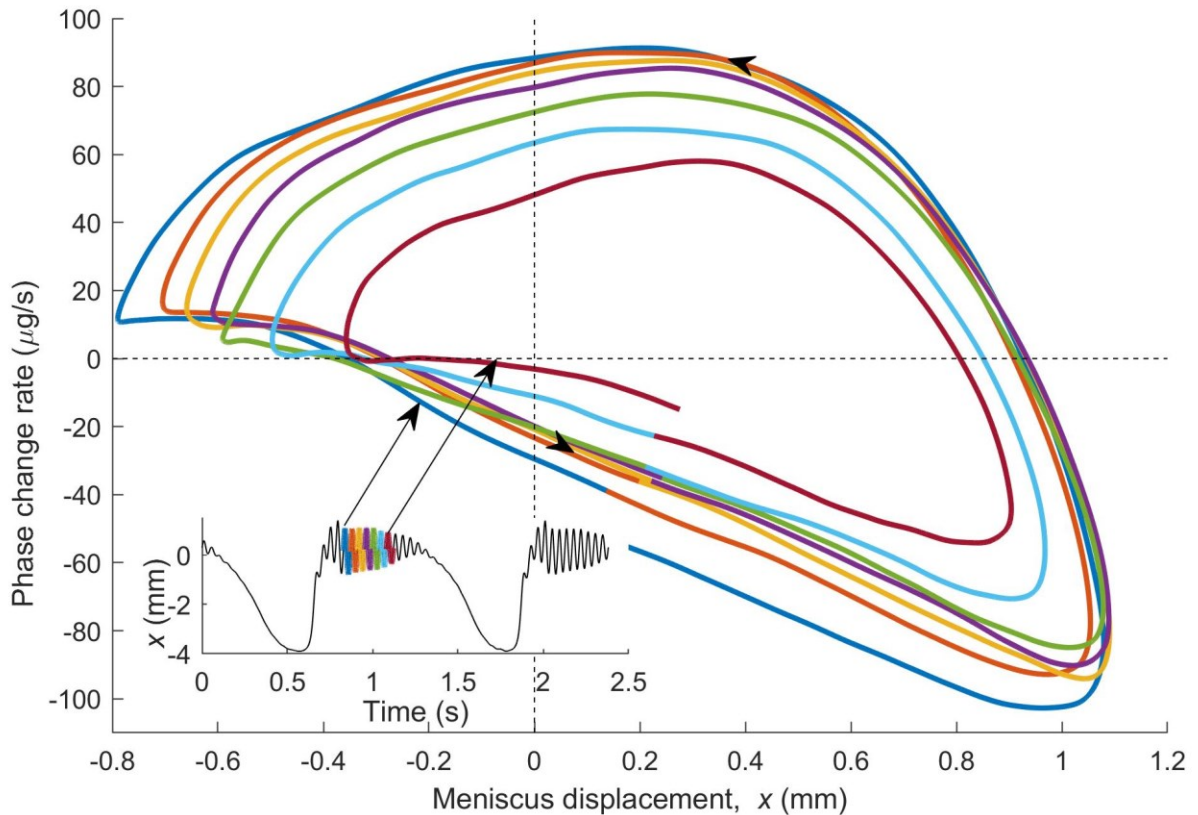


Figure 4-7 The phase change profile (evaporation-condensation rate as a function of displacement) with an inset indicating the corresponding cycles for beating oscillations with water.

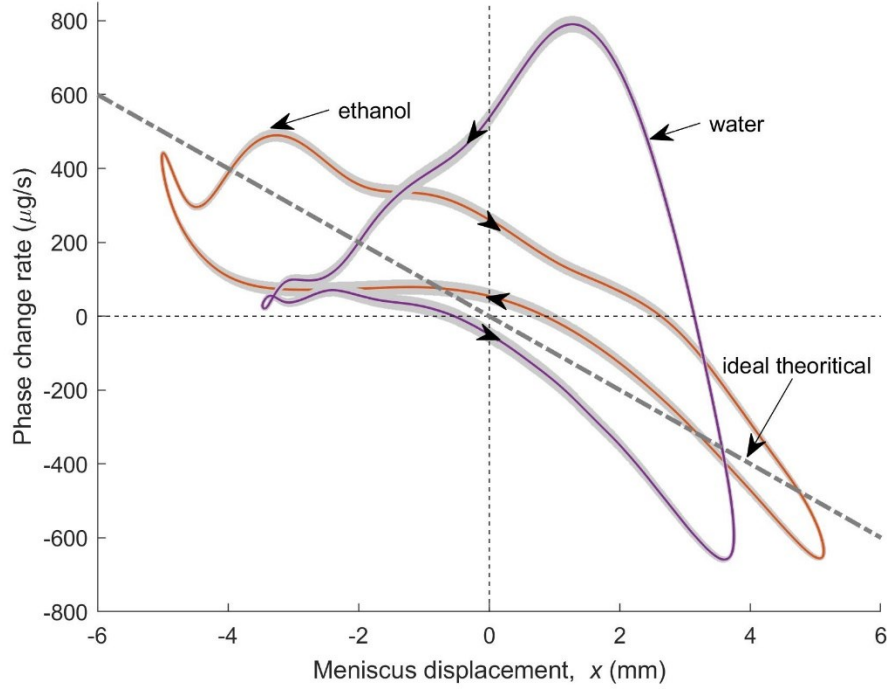


Figure 4-8 The phase change profile in the presence of the fiber for water and ethanol. The gray bands represent the measurement uncertainty.

## 4.4 Discussion

### 4.4.1 Phase change force and work

To evaluate how effective the phase change profiles are, we propose a method that is based on analyzing the phase angle between the phase change force and velocity. To do so, we first need to deduce the force (Eqn 2a) generated by the phase change ( $F_m$ ) using a momentum balance on the liquid plug (Figure 4-9):

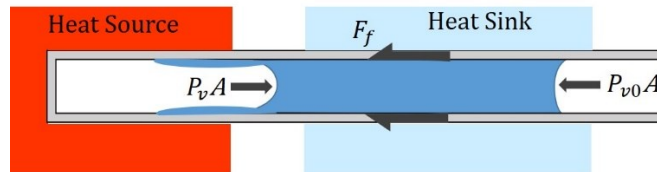


Figure 4-9 Applied forces on the liquid plug.

$$m_l \ddot{x} = (P_v - P_{v0})A - F_f \quad (4-2a)$$

where  $m_l$  is the mass of liquid plug,  $F_f$  is friction force, and  $\ddot{x}$  is the acceleration of the oscillating meniscus. Surface tension has been found to be negligible in this case [42,118,128]. Now, the vapor bubble pressure ( $P_v$ ) can be described with the ideal gas law as follows:

$$m \ddot{x} = \left( \frac{m_v RT_v}{A(L_{v0} + x)} - \frac{m_{v0} RT_v}{AL_{v0}} \right) A - F_f \quad (4-2b)$$

where  $m_{v0}$  is the mass of vapor at equilibrium. By replacing  $m_v = \Delta m_v + m_{v0}$ ,  $\tilde{x} = x/L_{v0}$ , and

$\widetilde{\Delta m_v} = \Delta m_v / m_{v0}$  in equation (4-2b) and reorganizing the terms, equation (4-2c) is formulated to more clearly define the involved forces in the momentum balance:

$$m\ddot{x} = \underbrace{\frac{P_{v0}A}{(1 + \tilde{x})} \widetilde{\Delta m_v}}_{F_m} - \underbrace{\frac{P_{v0}A}{(1 + \tilde{x})} \tilde{x}}_{F_v} - F_f \quad (4-2c)$$

Equation (2c) states that the change of momentum is due to the force produced by phase change (change of vapor mass,  $F_m$ ), spring force ( $F_v$ ) generated by the expansion-compression, and friction force ( $F_f$ ). The spring force is conservative and does not affect the growth or decay of the oscillation amplitude. However, the competition between the injected energy from the phase change force and the dissipation through friction controls the growth or decay of the amplitude for this spring-mass system. Knowing the force, the work done by phase change can be calculated using:

$$W_m = \oint F_m \dot{x} dt \quad (4-3)$$

where  $W_m$  and  $\dot{x}$  are work done by the phase change force and velocity of the oscillating meniscus, respectively. The calculated work will be used to show the effect of phase angle (section 4.4.2.) and to define a dimensionless number (section 4.4.3.) by which the effectiveness of the phase change is evaluated.

#### 4.4.2 Ideal phasing

To maximize the work done by the phase change force, which in turn maximizes the amplitude of oscillations, the force has to be in phase with velocity. In Figure 4-10a, we can observe that the force and velocity are not perfectly in phase for water (with the fiber). The power (Figure 4-10b) is therefore positive in some parts of the cycle (green zones) but negative in others (red zones). This effectively reduces the effectiveness of phase change in sustaining the oscillations. To find an ideal phasing, we propose theoretically shift ( $\Delta\theta$ ) the measured force and velocity and integrate their product at each phase shift to find maximum work. For water, we have found the maximum work at a phase shift of  $\Delta\theta = 52^\circ$ . Figure 4-10c and d show the shifted force and velocity, along with the power for this ideal phasing. The height increase of the green area and shifting from red zone (negative work) to the green zone (positive work, which injects energy into the oscillator increasing the amplitude) is the result of having ideal phase angle between phase change force and velocity.

The plotted graphs for ethanol show that the phase angle between the force and the velocity is naturally ideal, since the maximum work is at  $\Delta\theta = 0^\circ$  and as shown the resulting product of the two is all in the green area (Figure 4-11).

The maximum amplitude of oscillation with water is 7.2 mm for phase change work of 51  $\mu\text{J}/\text{cycle}$ . From the above study, an improved phasing could increase the work to 112  $\mu\text{J}/\text{cycle}$ , suggesting even higher amplitude. With ethanol, the amplitude of oscillations is 10.2mm with the phase change work of 94  $\mu\text{J}/\text{cycle}$  (lower maximum work compared to water). This comparison reveals that if the phase angle between the phase change force and velocity is improved for water, the oscillation amplitude should be more than with ethanol.

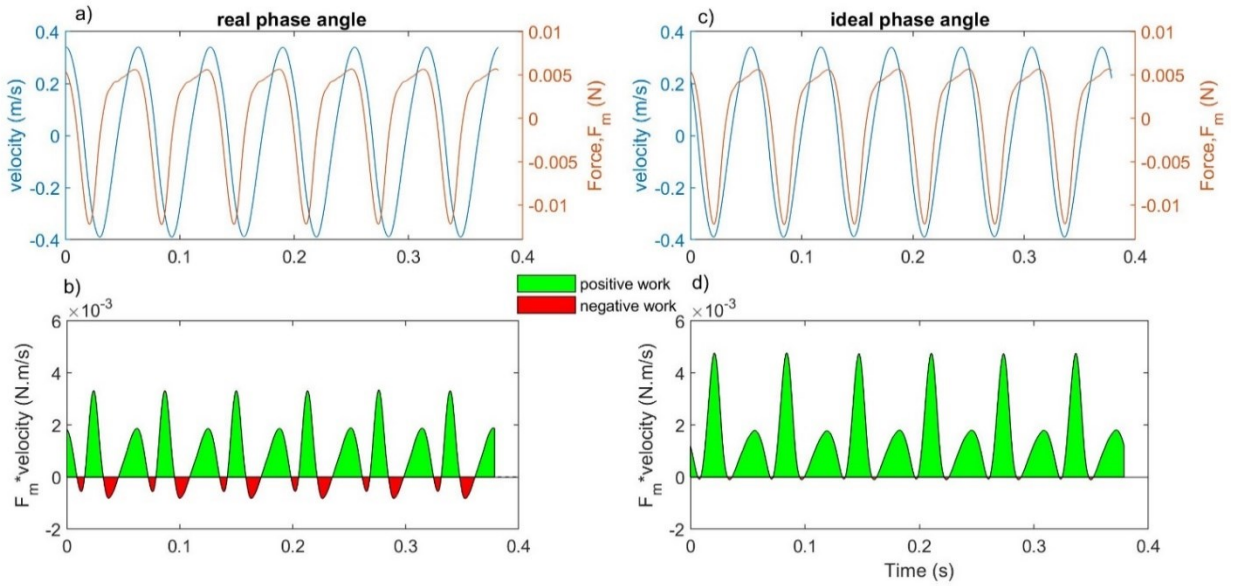


Figure 4-10 The velocity and phase change force (top) and their product (bottom) as a function of time with a,b) for the real phase angle, and c,d) for the ideal phase. Water in the presence of the fiber.

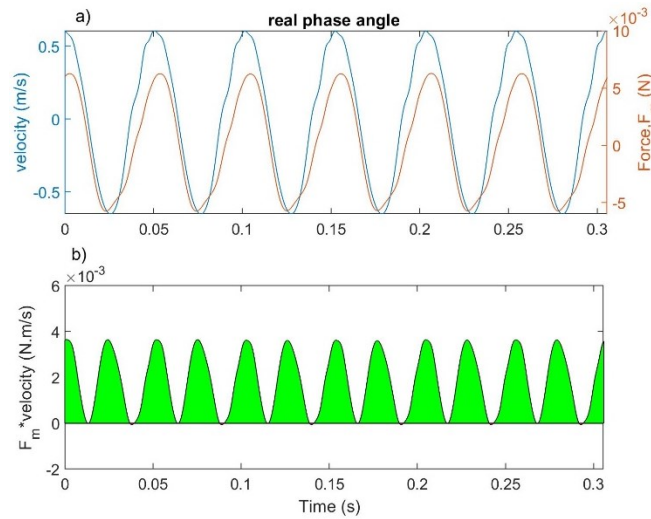


Figure 4-11 The velocity and phase change force (a) and their product (b) as a function of time showing an ideal phase angle between phase change force and the velocity. Ethanol in the presence of the fiber.

As a frame of reference, a linear phase change profile (see Figure 4-8) is an example of profile with ideal phase angle between the phase change force and velocity [48]. The linear phase change profile generates a force that is optimally in phase with velocity, which means all the work done by this force contributes to the increase of amplitude. However, the phase change profiles presented hereby (Figure 4-8) show hysteresis, particularly with water while with the profile with ethanol is closer to the ideal linear profile.

#### 4.4.3 Effectiveness of phase change

In this section, a dimensionless number called Phase Change Effectiveness (PCE) is introduced to evaluate the effectiveness of a phase change profile. The  $\varphi$  number equals the ratio of the

work done by the phase change ( $W_m$ ) to the maximum work ( $W_{m,max}$ ) assuming an ideal phase angle between the force and velocity (Eqn 4).

$$\phi = \frac{W_m}{W_{m,max}} \quad (4-4)$$

When  $\phi$  is one, there is no loss of generated energy by phase change since the phase change force is in phase with velocity during the complete cycle. The phase change effectiveness  $\phi = 0.5$  with water reveals that there is still room to increase the phase change work by improving the phase angle between the phase change force and velocity which would in turn lead to higher amplitude and performance. However, with ethanol the  $\phi = 0.99$ , which is coherent with the ideal phase angle between the phase change force and velocity observed above. Figure 4-12 better shows how the  $\phi$  number changes as a function of the phase shift between the phase change force and velocity for both water and ethanol. The  $\phi$  value at  $\Delta\theta = 0$  corresponds to the real phase angle between the measured phase change force and velocity, while the maximum value is  $\Delta\theta = 52^\circ$  for water, confirming that the force and the velocity are partially out of phase. The  $\phi$  number for ethanol at  $\Delta\theta = 0$  coincides with the maximum, showing the force and velocity are well in phase. Apart from different equilibrium position of the meniscus with water and ethanol, this difference can be also attributed to the difference in their latent heat. As shown in Figure 4-10a, the phase change force with water lags behind the velocity indicating more required time (due to higher latent heat) for the same amount of mass to be evaporated compared to ethanol. However, viscosity and surface tension are less likely to affect the phase change timing as their main contribution is to the formation of the thin. In a general case, ethanol with lower surface tension and higher viscosity compared to water is more favorable for the formation of the thin film but in the presence of the fiber, it was observed that the same length of the thin film were formed with water and ethanol. To see the effect of having different lengths of thin film and its effect on the phasing, we changed the length of the fiber and noticed that it does not affect the phasing [120].

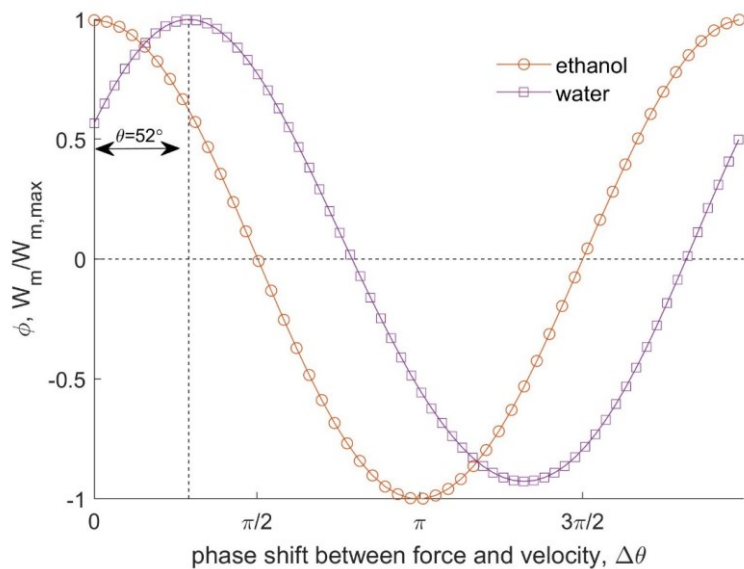


Figure 4-12 The phase change effectiveness,  $\phi$ , as a function of phase shift between the phase change force and the velocity for water and ethanol. An ideal phase corresponds to  $\phi = 1$ .

## 4.5 Conclusion

This paper proposes a method to analyze the effect of phasing and amplitude of phase change (evaporation-condensation) on the amplitude and stability of the oscillations in a thermally self-sustained oscillatory plug flow for two different working fluids: water and ethanol. The recorded pattern for water shows an increasing and decaying oscillating regime (beating phenomena) due to the shortage of the thin liquid film feeding the phase change. A wicking fiber is then inserted into the evaporator zone to play with the phase change mechanism. This approach significantly increases the amplitude of phase change yielding stable oscillations by providing enough thin film through capillary action. The startup did not happen for ethanol without the wicking fiber while the fiber initiates oscillations with a very different phase change profile from the one observed for water. To maximize the amplitude of oscillations, the work generated by the force from phase change should be maximized. To do so, the force should be in phase with velocity during a cycle. To validate the effectiveness of the discussed phase change profiles, we introduce a dimensionless number called Phase Change Effectiveness ( $\varphi$ ) that is the ratio of the work done by phase change to the maximum work (where the force and velocity are perfectly in phase). With water in the presence of the fiber, the  $\varphi$  number is at 0.56 meaning that around half of the energy from the phase change does not contribute to increase the oscillation amplitude. However, this number is at 0.99 with ethanol in the presence of the fiber, revealing that the phasing is essentially ideal for ethanol. The approach we propose allows to evaluate different phase change mechanisms in a self-sustained oscillatory flow that can be engineered by different techniques, from surface treatment to surface tailored structures. We expect that this approach can allow the optimization of the oscillation amplitude of PHP and SOFHE devices and therefore guide the future development of these applications.

### Acknowledgements

We acknowledge financial support from NSERC through the Scholarship and Discovery Programs (Canada). LN2 is a joint International Research Laboratory (IRL 3463) funded and co-operated in Canada by Université de Sherbrooke (UdeS) and in France by CNRS as well as ECL, INSA Lyon, and Université Grenoble Alpes (UGA). It is also supported by the Fonds de Recherche du Québec Nature et Technologie (FRQNT).



# Chapter 5

## How to improve design of the SOFHE?

**Authors and affiliation:** Nooshin Karami<sup>1,2</sup>, Albert Tessier-Poirier<sup>1,2</sup>, Amrid Annache<sup>1,2</sup>, Etienne Léveillé<sup>1,2</sup>, Luc G. Fréchette<sup>1,2</sup>

<sup>1</sup>Institut Interdisciplinaire d'Innovation Technologique (3IT), Université de Sherbrooke, Sherbrooke, QC, Canada

<sup>2</sup>Laboratoire Nanotechnologies Nanosystèmes (LN2), CNRS UMI-3463, Université de Sherbrooke, Canada

**Submission date:** 04-05-2023.

**Acceptance date:** 17-08-2023.

**Publication date:** 29-08-2023.

**Status:** published.

**Journal:** Journal of Micromechanics and Microengineering.

**Reference:** N. Karami, A. Tessier-Poirier, É. Leveille, A. Annache, L.G. Fréchette, Capillary enhanced phase change in a microfabricated self-oscillating fluidic heat engine (SOFHE), *J. Micromechanics Microengineering*. 33 (2023). doi:10.1088/1361-6439/acf13b.

**Title:** Capillary Enhanced Phase Change in a Microfabricated Self-Oscillating Fluidic Heat Engine (SOFHE).

**Titre français:** Changement de phase amélioré par capillarité dans un moteur thermique fluide auto-oscillant microfabriqué.

**Contribution statement:** I carried out all the experimental and theoretical work presented in this article. Amrid Annache was involved in the microfabrication process for training and supervision. The co-authors provided advice, suggestions, and revision during the research and writing process.

**Abstract:** This paper reports the design, fabrication, and characterization of a miniaturized version of a self-oscillating fluidic heat engine (SOFHE) for thermal energy harvesting. This new design includes capillary corners of a square cross-section, as well as an etched capillary path on the bottom wall that improves the performance in terms of stability and mechanical power owing to the enhanced phase change. The engine consists of a vapor bubble trapped in a microchannel by an oscillating liquid plug (acting as a piston) set in motion by periodic evaporation and condensation in the vapor bubble. The underlying physics of the oscillations is similar to those of a single-branch pulsating heat pipe. The channel is microfabricated by anodically bonding a grooved glass wafer (top and sidewalls) to a silicon wafer (bottom wall). To further increase the phase change, two more channels are fabricated with an etched capillary path on the bottom wall at two different widths of 25 and 50  $\mu\text{m}$  and a depth of 100  $\mu\text{m}$ . This is

the first miniaturized SOFHE that generates a reliable amplitude in the millimeter range. By measuring the change in the volume of the vapor bubble and the frequency, we calculated the change in pressure using the momentum balance on the liquid plug, and then calculated the work, mechanical power, and power density. We observed that the addition of the etched capillary path at a width of 50  $\mu\text{m}$  led to a twofold increase in the amplitude (from 1.6 to 4 mm) and consequently a fivefold increase in the generated power (from 7 to 39  $\mu\text{W}$ ). This study opens a new path towards designing different wicking structures to maximize the amplitude and power density of SOFHE, making it a promising thermal energy harvester to power wireless sensors.

**Keywords:** Micro heat engine, thermal harvesting, self-oscillation, phase change, capillary, single-branch pulsating heat pipe.

**Résumé français:** Cet article présente la conception, la fabrication et la caractérisation d'une version miniaturisée d'un moteur thermique fluide auto-oscillant (SOFHE) pour la collecte d'énergie thermique. Cette nouvelle conception améliore les performances en termes de stabilité et de puissance mécanique grâce à l'amélioration du changement de phase à travers les coins capillaires de la section carrée, ainsi qu'à un chemin capillaire gravé sur la paroi inférieure. Le moteur consiste en une bulle de vapeur piégée dans un microcanal par un bouchon liquide oscillant (agissant comme un piston) mis en mouvement par l'évaporation et la condensation périodiques dans la bulle de vapeur. La physique sous-jacente des oscillations est similaire à celle d'un caloduc pulsant à une seule branche. Le canal est microfabriqué par collage anodique d'une plaquette de verre rainurée (dessus et parois latérales) à une plaquette de silicium (paroi inférieure). Pour augmenter encore le changement de phase, deux autres canaux sont fabriqués avec un chemin capillaire gravé sur la paroi inférieure à deux largeurs différentes de 25 et 50  $\mu\text{m}$  et à une profondeur de 100  $\mu\text{m}$ . Il s'agit du premier SOFHE miniaturisé qui génère une amplitude fiable de l'ordre du millimètre. En mesurant le changement de volume de la bulle de vapeur et la fréquence, nous avons calculé le changement de pression en utilisant le bilan de quantité de mouvement sur le bouchon liquide, puis nous avons calculé le travail, la puissance mécanique et la densité de puissance. Nous avons observé que l'ajout du chemin capillaire gravé d'une largeur de 50  $\mu\text{m}$  conduisait à une multiplication par deux de l'amplitude (de 1,6 à 4 mm) et par conséquent à une multiplication par cinq de la puissance générée (de 7 à 39  $\mu\text{W}$ ). Cette étude ouvre une nouvelle voie vers la conception de différentes structures de mèches pour maximiser l'amplitude et la densité de puissance de la SOFHE, ce qui en fait un collecteur d'énergie thermique prometteur pour alimenter des capteurs sans fil.

**Mots clés:** Micro-moteur thermique, récolte thermique, auto-oscillation, changement de phase, capillaire, caloduc pulsé à une seule branche.

## 5.1 Introduction

The move of our society towards an increasingly smart world has led to the emergence of the “Internet of Things (IoT),” which consists of objects with embedded sensors that capture data and exchange it with other devices over the Internet [96]. For example, smart cities take advantage of IoT for sustainable development practices, including transportation networks and waste management. To do so, a massive network of wireless sensors is implemented; thus, there is a need for durable and autonomous means to power them [97]. To address this increasing demand, energy harvesting, which generates electricity from ambient energy sources, has come into perspective. Thermal energy harvesters (TEH) are promising candidates for applications

where waste heat is available. TEHs can convert thermal energy into electricity directly using thermoelectric generators (TEGs) or indirectly (thermal-to-mechanical-to-electrical) using heat engines coupled with transducers. The performance of TEGs, which is based on the Seebeck effect [5], is limited by the figure-of-merit of the materials. The advantage of the latter is their flexibility in terms of design and room for optimization. The self-oscillating fluidic heat engine (SOFHE) is a novel micro heat engine first introduced and studied by the same research group [48,105,106,115,116,120,122,129]. The SOFHE was proposed to power wireless sensors when coupled with an electromechanical transducer [105] as a thermal energy harvester. As shown in Figure 5-1, the SOFHE harvests waste heat and converts it into mechanical energy, which, in turn, is converted into electrical energy by a transducer. It has a mechanical power density in the range of fractions of milliwatts/cm<sup>3</sup> [115], which can be used for many wireless sensors with an average power requirement of microwatts. The SOFHE can provide the benefit of being maintenance-free, which is particularly valuable when accessibility is limited. As the SOFHE does not have moving parts that can wear out or consume materials like batteries, it is expected to continue functioning if the device is perfectly sealed to maintain hermeticity and retain the fluid inside. SOFHE's mechanical power could also be directly used for pumping when combined with appropriate valves [117], for cooling electronics, lab-on-chip, or other microfluidic applications.

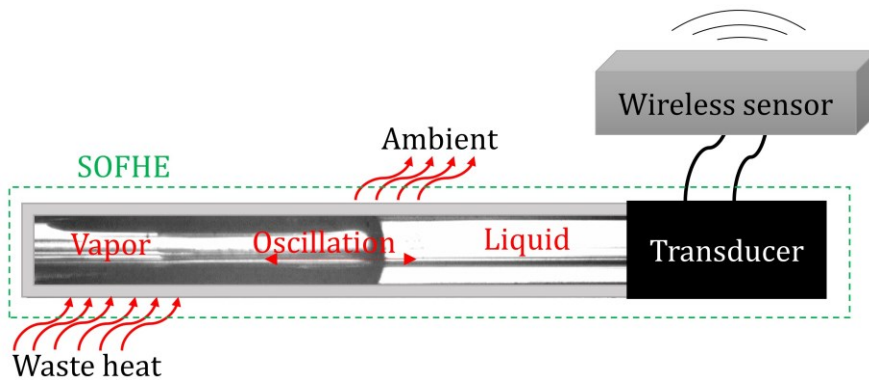


Figure 5-1 SOFHE application, harvesting waste heat to power wireless sensors [116].

The working principle of the SOFHE is similar to that of a single-branch pulsating heat pipe [38]. The SOFHE is a channel filled with working fluid, with one heated closed end (evaporator) and one cooled open end (condenser). When the closed end is heated, a vapor bubble forms and expands until it reaches an equilibrium point. Once the vapor is established, it will remain trapped by an oscillating liquid plug that acts as a piston (Figure 5-2). The piston provides mechanical work through a unique oval-shaped phase change thermodynamic cycle [115]. There are other examples of micro heat engines, including micro gas turbines [19,130] and micro steam turbines [23][24][22], which demonstrate traditional Brayton and Rankine thermodynamic cycles, respectively. They offer high power (watt-scale), but have the complexity of high-speed rotating parts. The simple design of an SOFHE with no moving parts gives it an advantage over microturbines for applications with lower power requirements. Compared to other phase-change micro heat engines, including the so-called P3 engine (peak power at 0.8  $\mu\text{W}$ ) [8] and bi-stable membrane (mechanical power at 1.3  $\mu\text{W}$ ) [17,18], SOFHE offers a mechanical power that is 100X greater. It should be mentioned that unlike some other micro heat engines, the mechanical power density of the SOFHE has not yet been optimized, and there is room for further improvement. For example, in a mesoscale SOFHE, it was shown that both the mechanical

power and power density increased as the length of the liquid plug decreased [115]. This is a promising outcome for the miniaturization of SOFHE. Besides, it was observed that varying the phase change rate (evaporation-condensation) significantly boosts the power density [115].

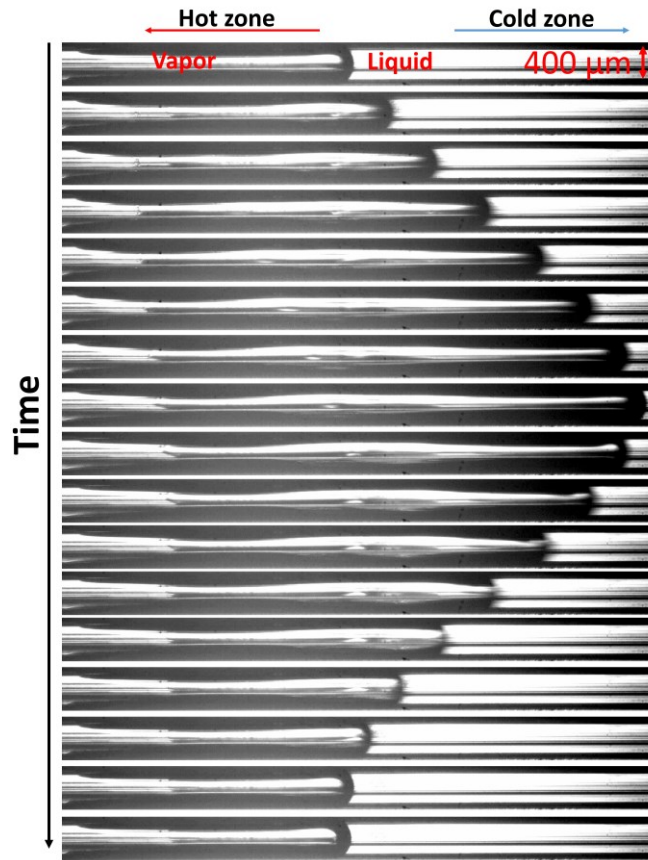


Figure 5-2 The complete expansion-compression cycle of the vapor bubble for producing work (real cycle) [116].

The self-sustained oscillatory flow in the SOFHE is modeled as a damped spring-mass system, where the vapor bubble acts as the restoring force, the friction of the liquid plugs induces damping, and its mass provides inertia [43,57,108,121]. The force that sustains the oscillations in this system is the pressure generated by the change in the mass of the vapor due to cyclic evaporation and condensation. To perturb the equilibrium of this spring-mass system for oscillation start-up, the force generated by the phase change must be greater than the counteracting viscous force [48]. During start-up, the amplitude gradually increases until it saturates, owing to the nonlinearities that exist in the system. These nonlinearities might originate from different sources, such as phase change limitations or geometrical restrictions, which are discussed in detail by Tessier-Poirier [122]. It has been shown that the SOFHE power increases with the amplitude of the oscillation when the evaporation-condensation rate is enhanced (for a constant frequency) [115]. The common mechanism for the phase change (evaporation-condensation) in this thermally induced self-oscillatory flow is a thin film that is left behind the moving meniscus [40]. This makes the motion dependent on oscillation amplitude. To overcome this problem, liquid must be introduced into the evaporator to form a thin film that feeds the phase change and facilitates the start-up. Adding wicking structures such as capillary grooves [82,83], corners [25,26], and wicking fibers [120,129] are promising

solutions. In a mesoscale version of the SOFHE, which is a tube with a millimeter-scale inner diameter, the mechanical power of the SOFHE showed a significant increase (thirtyfold) by boosting the phase-change rate in the presence of a wicking fiber [115]. The wicking fiber forms capillary corners with the tube, pumps liquid from the liquid plug towards the evaporator, and intensifies the net evaporation rate. In the first microfabricated demonstration of SOFHE [106], which was fabricated by bonding two glass wafers that were wet-etched to form a microchannel, very small-amplitude vibrations (10  $\mu\text{m}$ ) were observed. To address the issue of a small amplitude in micro SOFHE and to establish a reliable start-up mechanism, we aim to increase the net evaporation rate. This was first performed by forming a square cross-section microchannel with sharp corners to imitate the role of the fiber observed in the mesoscale SOFHE. The initial results of this approach were presented at the PowerMEMS 2022 conference [116]. The current study extends this work by adding etched capillary paths to enhance wicking behavior. To evaluate the effect of the phase-change enhancement with these features, the amplitude and frequency were experimentally measured and compared for three different micro SOFHEs, including one with no etched capillary path and two with etched capillary paths of 25 and 50  $\mu\text{m}$  in width. To further understand the impact of phase-change enhancement in micro SOFHE, a discussion on the forces, thermodynamic work per cycle, power, and power density is also presented.

## 5.2 Methodology

### 5.2.1 Device

The engine is a microfabricated square channel that benefits from its corners acting as a capillary path. The channel was formed by anodically bonding silicon (thickness 500  $\mu\text{m}$ ) to a glass wafer (borofloat33, thickness 600  $\mu\text{m}$ ) to provide visual access inside the device and better thermal insulation. Before bonding, the channel was grooved on a glass wafer using a dicing machine (Disco DAD-320) with a hydraulic diameter ( $D_h$ ) of 375  $\mu\text{m}$ . In some configurations, an additional capillary path was added by etching a trench in Si along the channel length. Figure 5-3 shows the cross section of the fabricated device, with a dashed trench representing the etched capillary path on the bottom wall. To create the trench, a two-level masking process is followed, as shown in Figure 5-4. The first level involves creating alignment marks on both Si (lithography and RIE) and glass wafers (lithography and hydrofluoric acid (HF) wet etching). Second-level masking involves creating a capillary path on a Si wafer by deep reactive ion etching (DRIE). The wafers were cleaned using solvent and Piranha. Before bonding, diluted HF was used to remove native oxide on the Si wafer. For the capillary trench, we considered two different widths ( $W$ ) of 25  $\mu\text{m}$  and 50  $\mu\text{m}$ , with a depth ( $H$ ) of 100  $\mu\text{m}$  and a length of 20 mm. The total length of the device is  $L_T=8.5$  cm, the thickness is  $H_T=1.1$  mm, and the width is  $W_T=3$  mm. The volume of micro SOFHE is therefore  $V_{SOFHE} = L_T * A = 0.26$   $\text{cm}^3$ , where  $A = H_T * W_T$ . The heated end of the device was closed with glue, whereas the cooled end was open.

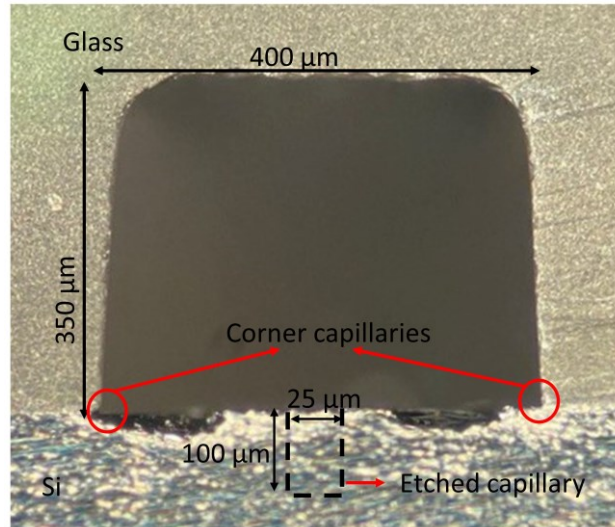


Figure 5-3 Cross-section of the microfabricated channel using anodic bonding of Si and grooved glass wafers, shown from the open end. The dashed line is the representative of the etched capillary trench included in some configurations [116].

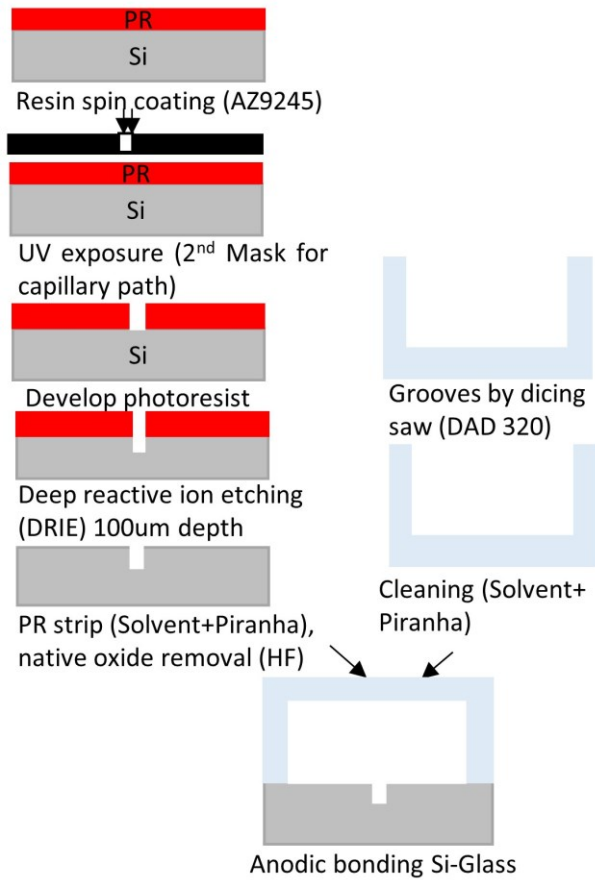


Figure 5-4 Microfabrication process flow.

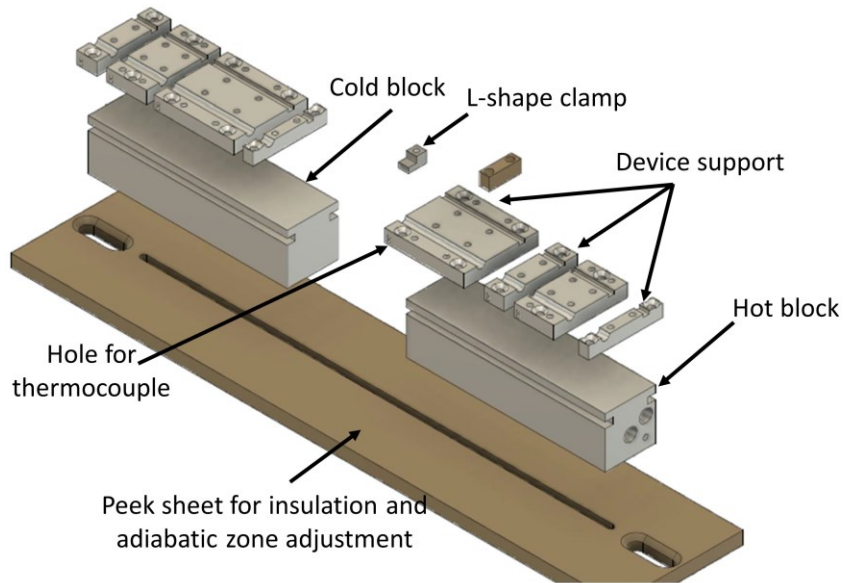
### 5.2.2 Test setup

Figure 5-5a shows a disassembled view of the experimental test rig designed to characterize the micro SOFHE. The main components are two aluminium blocks: one is heated by a cartridge heater, and the other is cooled by cold water from a thermostatic bath. The blocks were mounted on an insulating Peek sheet with a slot to adjust the distance between them. This distance, the so-called adiabatic zone, allows for a thermal gradient over the device, which was set to 2 mm. The device supports were designed to adjust the length of the device in contact with the hot and cold blocks. An L-shaped clamp was used to clamp the device support onto the blocks. A conductive thermal paste (TG-7) was used to reduce the contact thermal resistance between the device and device support. Thermocouples were integrated into the device supports to control the temperature of the hot ( $T_H$ ) and cold ( $T_C$ ) zones.

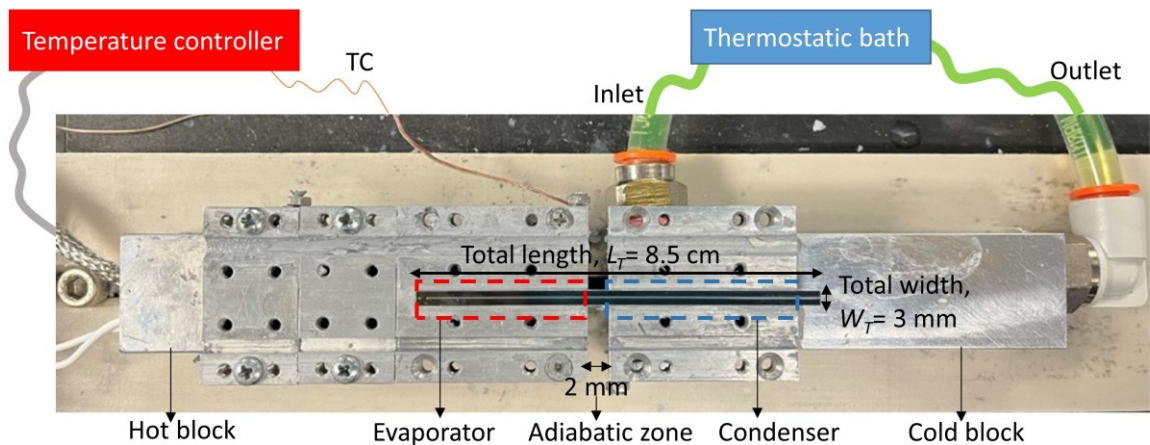
### 5.2.3 Test procedure

To start the test, the device was treated with oxygen plasma to clean and ensure hydrophilicity of the inner channel surfaces (at 100 W for 1 min). The device was filled with deionized water and mounted on blocks using a thermal paste. Figure 5-5b shows an image of the setup with the device mounted on the top. Regarding the working fluid, it can be changed based on the available thermal gradient. The lengths of the device in contact with the hot and cold blocks form the evaporator and condenser sections, respectively. Herein, the length is set at 3.5 and 4 cm for the evaporator and condenser, respectively. These specific lengths are chosen to simplify the handling and testing of the device. However, they will require optimization in future steps. The condenser temperature was set to 15 °C, and the heating process was initiated. A vapor bubble (occupying the cross section) forms in the evaporator and grows lengthwise until it reaches equilibrium. The equilibrium point was in the adiabatic zone. We then continued to increase the evaporator temperature until oscillations started at 120 °C. A high-speed camera mounted on a stereoscope recorded the position of the oscillating meniscus as a function of time in order to measure the amplitude and frequency of the oscillations. An image-processing MATLAB code was used to extract the positions from the recorded video. The uncertainty of the amplitude measurement is  $\pm 4\%$ , which comes from the calibration to convert pixels into micrometers.

The device without an etched capillary path was characterized at four different evaporator temperatures ( $T_H$ ). The tests were performed for two more devices with one capillary path etched on the bottom wall at widths of 25 and 50  $\mu\text{m}$ .



a)



b)

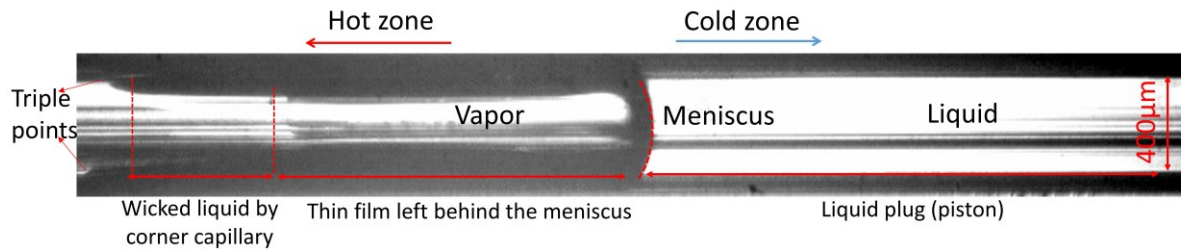
Figure 5-5 The experimental test rig to measure the oscillation amplitude and to visualize the oscillating meniscus a) schematic exploded view, b) real setup with the device on top [116].

### 5.3 Results

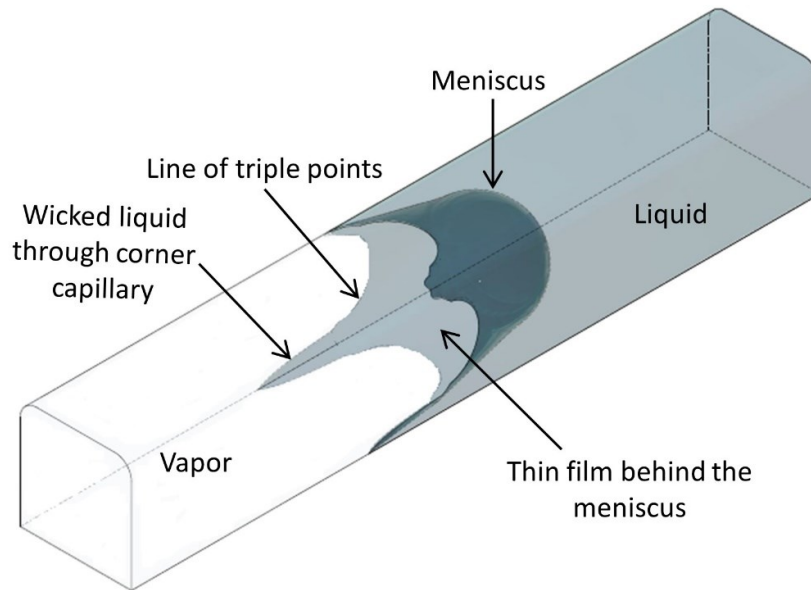
The new design of micro SOFHE takes advantage of the sharp capillary corners of a square cross section to pump liquid into the evaporator. Figure 5-6a (a frame from a recorded video during oscillations) shows the wicked liquid in the corners that ends at a triple point (interface of solid-liquid-vapor). It also shows a thin film behind the oscillating meniscus, which is distinguished by a moving shadow on the top wall. To better visualize the different parts, a 3-D schematic of the oscillating meniscus is presented in Figure 5-6b. The line of triple points (formed by the thin film behind the meniscus) and the liquid wicked along the corner capillaries are the main contributors to the phase change because of their low thermal resistance [44].

Figure 5-7 shows the amplitude of the oscillations at start-up temperature (120 °C). Positive and

negative values indicate moving towards the condenser and evaporator, respectively. The measured peak-to-peak amplitude is 1 mm and the frequency of the oscillations is 36 Hz. The oscillations are sustained for hours with a constant amplitude, demonstrating highly reliable and repeatable behavior. This design also guarantees the start-up of oscillations without the need to insert an additional wicking structure, as is required for the mesoscale SOFHE [105,115,120,129]. Therefore, the start-up and sustainability of the micro SOFHE are achieved by increasing the rate of net evaporation-condensation through the corner capillary.



a)



b)

Figure 5-6 a) 2-D top view recorded by high-speed camera showing the oscillating meniscus that leaves a thin film behind (the shadow covering the top wall) as well as the wicked liquid through corner capillaries (the dark edges ending with triple points) [116], b) 3-D schematic to better show the lines of triple points that have main contribution to the evaporation due to their low thermal resistance.

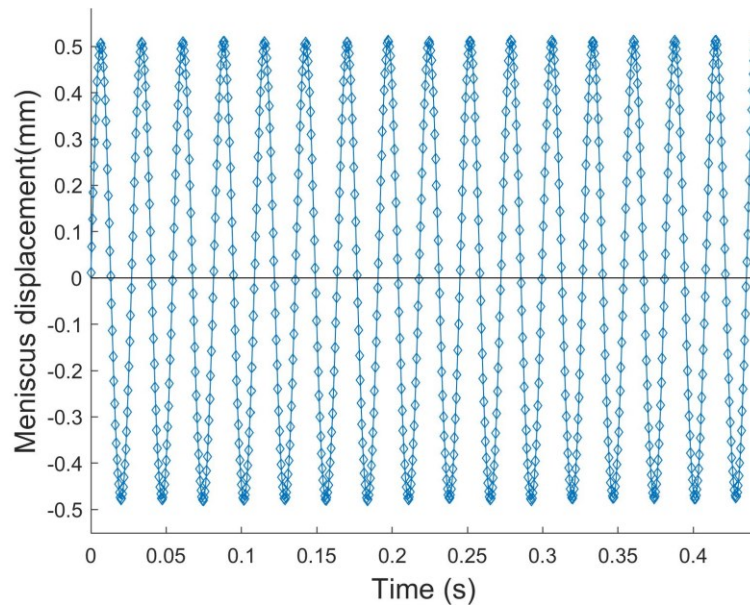


Figure 5-7 Meniscus displacement as a function of time at evaporator temperature of 120 °C for the device without an etched capillary path [116].

As discussed in our previous study [115] on characterizing mesoscale SOFHE, enhancing the phase change by increasing the evaporator temperature ( $T_H$ ) significantly increases the phase-change rate, which in turn increases the oscillation amplitude. Figure 5-8 shows the evolution of the meniscus position as a function of time as the evaporator temperature increased. The expected trend is observed in micro SOFHE, where the amplitude of the oscillations increases from 1 mm to 1.6 mm by increasing  $T_H$  from 120 °C to 150 °C.

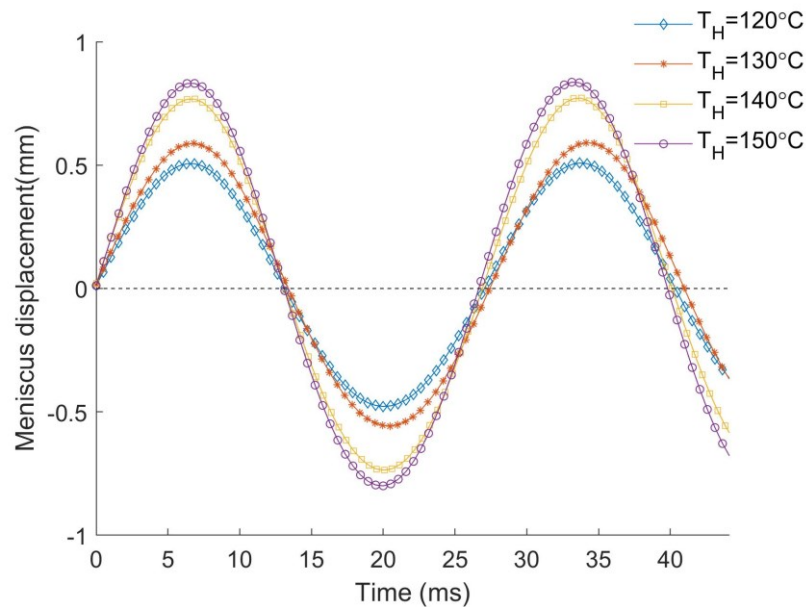


Figure 5-8 Meniscus displacement as a function of time at four different evaporator temperatures for the device without an etched capillary path [116].

Observing the positive effect of the capillary pumping of the liquid through sharp corners drove the new design of the micro SOFHE, in which a capillary path is etched on the bottom wall. Thus, more liquid can be pumped towards the evaporator to intensify the net evaporation rate, leading to an increase in the amplitude. As shown in Figure 5-9, the peak-to-peak amplitude increases from 1.6 mm to 2.6 mm by adding a capillary path with a width of 25  $\mu\text{m}$  and even up to 4 mm for a trench width of 50  $\mu\text{m}$ . The results showed better performance with an increase in the width of the capillary path.

This can be explained by analyzing the capillary flow dynamics inside the capillary path. It can be considered a closed channel (with the free surface acting as the fourth wall) if the aspect ratio ( $\lambda=H/W$ ) of the channel is sufficiently large ( $\lambda > 1$ ) [131], which is valid in our study ( $\lambda=2$  and 4). The volumetric flow in the capillary path is a function of the length of liquid penetration along the capillary and the cross-sectional area. The length of liquid penetration along the capillary ( $L$ ) is determined by the surface tension and friction forces, leading to Washburn's equation [132].

$$L^2 = \frac{\sigma \cos \theta}{2\mu} rt \quad (5-1)$$

where  $\sigma$  is the surface tension,  $\theta$  is the contact angle,  $\mu$  is the viscosity,  $r$  is the capillary radius, and  $t$  is the time. As the width of the capillary path increased, the length of the liquid penetration increased, and the cross-sectional area led to an increase in the capillary-pumped volumetric flow. A higher amount of pumped liquid intensifies the net evaporation rate, resulting in an increase in the oscillation amplitude.

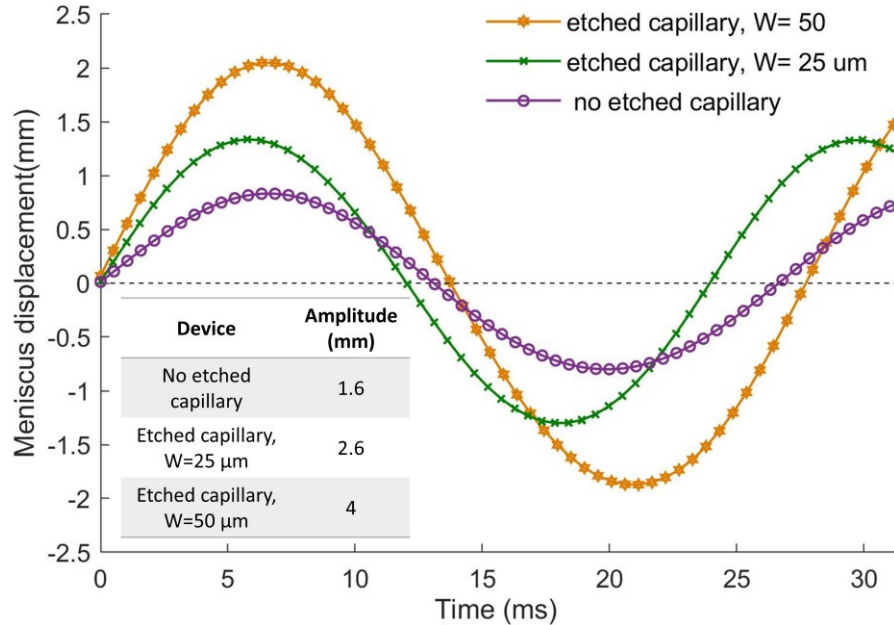


Figure 5-9 Increase of the oscillation amplitude because of amplifying wicking action by adding an etched capillary path on the bottom wall with the depth of 100  $\mu\text{m}$  at two different widths of 25  $\mu\text{m}$  and 50  $\mu\text{m}$  at evaporator temperature of 150  $^{\circ}\text{C}$ .

## 5.4 Discussion

In this section, the micro SOFHE is characterized in terms of the mechanical power density to better understand the effect of this increase in amplitude on the SOFHE power. First, it is necessary to calculate the applied pressure on the liquid plug owing to the expansion, compression, and phase change. To do so, momentum balance is performed (equation 2) on the control volume defined over the liquid plug, as shown in Figure 5-10.

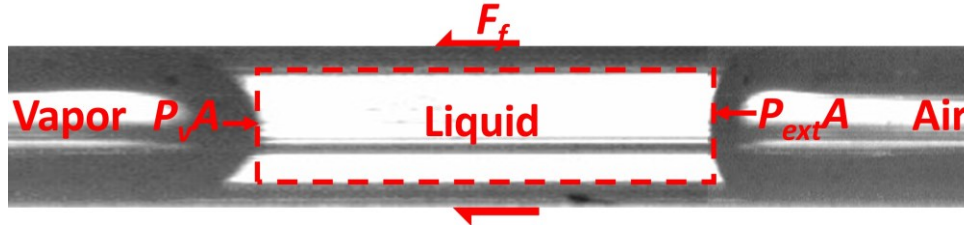


Figure 5-10 The forces applied on the liquid plug.

$$\underbrace{m_l \ddot{x}}_{F_m} = \underbrace{(P_v - P_{ext})A}_{F_p} - F_f \quad (5-2)$$

where  $m_l$  is the mass of the liquid plug (assumed to be constant),  $F_m$  is the inertial force,  $A$  is the channel cross-sectional area,  $P_{ext}$  is the external pressure (open end at atmospheric pressure),  $F_p$  is the pressure force,  $F_f$  is the friction force, and  $\ddot{x}$  is the acceleration of the oscillating meniscus. The friction force experienced by the liquid plug along the wall depended on the velocity profile, which was defined based on the kinematic Reynolds number ( $Re_\omega \equiv \omega R^2/\nu$ ). The velocity profile in a pulsatile flow can be considered a quasi-static Poiseuille profile for  $Re_\omega < 10$  [111]. For the SOFHE filled with water with a hydraulic diameter of 375  $\mu\text{m}$  and frequency of 36 Hz,  $Re_\omega = 8$ . Therefore, the friction force is well described by the Poiseuille flow [133]:

$$F_f = -8\pi\mu L_l \dot{x} \quad (5-3)$$

where  $L_l$  is the length of the liquid plug and  $\dot{x}$  is the velocity of the oscillating meniscus. The forces applied to the liquid plug, including inertia, friction, and pressure, as a function of time are plotted in Figure 5-11. Forces are intermediate variables used to calculate the work.

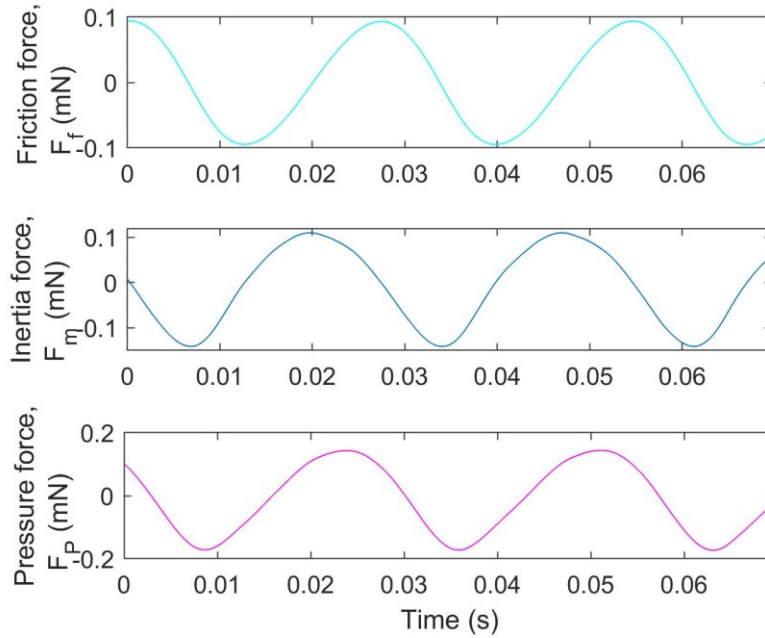


Figure 5-11 The applied forces on the liquid plug, including friction, inertia, and pressure force as a function of time for the device with no etched capillary path at evaporator temperature 120°C.

Calculating the pressure and measuring the change in the volume of the vapor bubble enables us to plot the thermodynamic cycle (P-V) of the SOFHE, as shown in Figure 5-12, at four different evaporator temperatures for the device with no etched capillary path. Integrating the area of the P-V cycles (equation 4) yields the work performed in each cycle. As shown, increasing the oscillation amplitude created a larger P-V cycle that is capable of generating more work. A portion of this work is dissipated through the friction of the liquid plug. In the mesoscale version of SOFHE, it was shown that at an optimum load, half of the cycle work is consumed to overcome friction [115]. This means that the net available work per cycle that the SOFHE can provide to a transducer is half the cycle work ( $W_{net}=W_{cycle}/2$ ).

$$W_{cycle} = \oint P_v dV_v \quad (5-4)$$

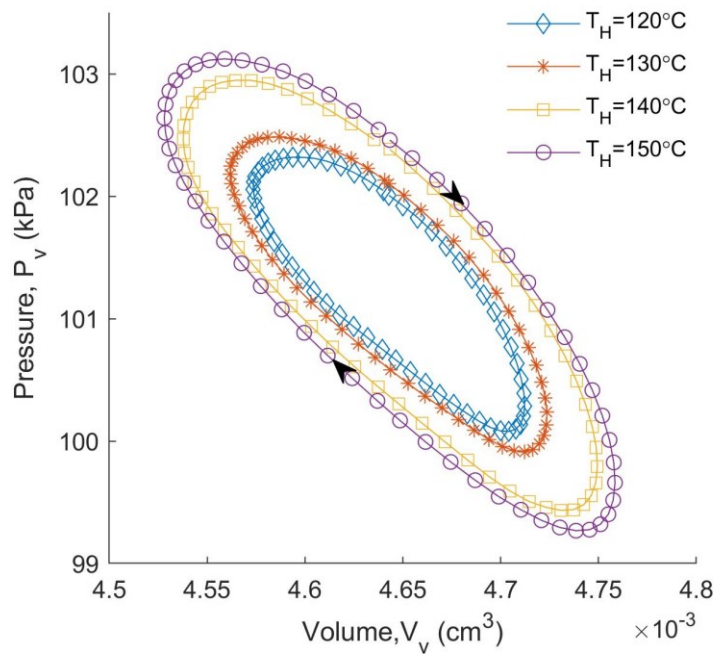


Figure 5-12 Thermodynamic (P-V) cycle of micro SOFHE at four different evaporator temperatures.

Knowing the available net work per cycle and frequency of the SOFHE, the power ( $P=W_{net}*f$ ) and power density ( $P_d=P/V_{SOFHE}$ ) can be calculated. Figure 5-13 shows the power as a function of the evaporator temperature at both the micro (solid line) and meso (dashed line) [115] scales. The power values are normalized by the maximum power at the highest temperature to better compare trends. The results show that the increasing trend of power as a function of the evaporator temperature at the microscale is similar to that observed for mesoscale SOFHE. This suggests that the miniaturization of the SOFHE does not affect the dependency of the power on the evaporator temperature.

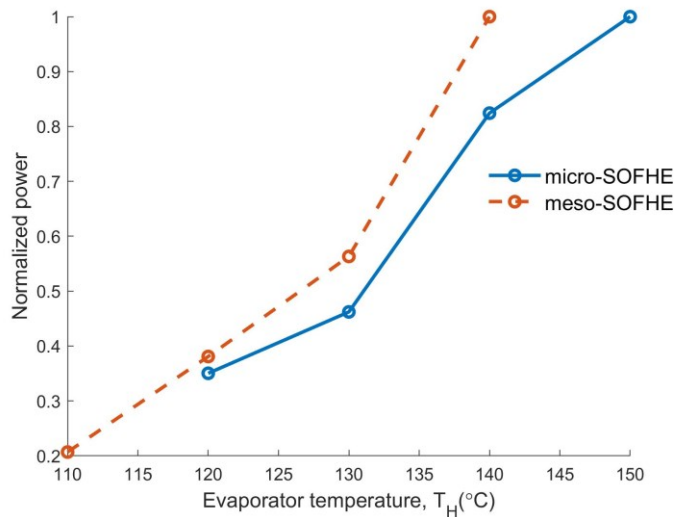


Figure 5-13 The normalized power as a function of evaporator temperature at micro and mesoscale SOFHE showing an increasing trend for both.

The power and power densities of the three devices are listed in Table 5-1 along with the values for mesoscale SOFHE [115]. A comparison of the power reveals a five-fold increase (from 8  $\mu\text{W}$  to 40  $\mu\text{W}$ ) by adding a capillary path with a width of 50  $\mu\text{m}$ . The significant increase in power by intensifying the phase change through capillary pumping is a key outcome of this study, which opens a new path towards designing different wicking structures and optimizing them to maximize the amplitude of the oscillation, which enhances the power of the SOFHE, as well as the heat transfer of pulsating heat pipes.

Table 5-1 The power, and power density of the three tested microscale SOFHEs and the mesoscale SOFHE showing an increase by adding a capillary path.

	Device	Power ( $\mu\text{W}$ )	Power density ( $\mu\text{W}/\text{cm}^3$ )
microscale	no etched capillary	8	29
	etched capillary, $W= 25 \mu\text{m}$	25	95
	etched capillary, $W= 50 \mu\text{m}$	40	150
mesoscale [115]	glass tube with wick fiber	1827	609

## 5.6 Conclusion

In this study, the performance of a microfabricated self-oscillating fluidic heat engine (SOFHE) is enhanced by boosting the phase change through corner capillaries as well as etched capillary paths. The engine was microfabricated by anodic bonding of a Si wafer and grooved glass wafer to form a square cross-sectional microchannel with a hydraulic diameter of 375  $\mu\text{m}$ . The sharp corners in the square channel act as capillary paths, pumping liquid from the liquid plug towards the evaporator. This intensifies the phase-change rate, which in turn increases the oscillation amplitude (a key parameter for increasing the SOFHE output power). This design yields a start-up and sustainability of oscillations with an amplitude in the range of millimeters and a frequency of 37 Hz. To further increase the phase change, capillary paths were etched on the bottom Si wall of the device using DRIE. This modification led to a two-fold increase in the amplitude, which in turn increased the mechanical power five-fold. In future work, different wicking structures can be added to SOFHE to engineer phase change. Thus, we can enhance the performance of SOFHE to become a promising power supply for wireless sensors when coupled with an electromechanical transducer. This strategy also promises to enhance the performance of pulsating heat pipes, which are being increasingly considered for the thermal management of electronics.

### Acknowledgements

We acknowledge financial support from the NSERC through the Scholarship and Discovery Programs (Canada). LN2 is a joint International Research Laboratory (IRL 3463) funded and cooperated in Canada by the Université de Sherbrooke (UdeS), and in France by CNRS, ECL, INSA Lyon, and Université Grenoble Alpes (UGA). This is also supported by Fonds de Recherche du Québec Nature et Technologie (FRQNT). The authors declare that they have no competing interests.



# Chapter 6

## Discussion

### 6.1 SOFHE vs TEGs and micro heat engines

The measurement of mechanical power and efficiency of the SOFHE (chapter 3) provides a basis for comparison with other competing technologies, including TEGs and other micro heat engines discussed in the state-of-the-art (chapter 2). To facilitate this comparison, Figure 6-1 illustrates the theoretical second law efficiency of TEGs (calculated using Eqn 2-1) alongside the experimentally measured efficiency of the SOFHE. In the context of the SOFHE, two efficiency metrics can be defined, which represent upper and lower bounds. In Chapter 3, the efficiency calculation considers the saturation temperature corresponding to the highest and lowest pressure points of the cycle (upper bound). This temperature difference represents the minimum requirement for the SOFHE to function effectively. However, due to the system's limitations in efficiently transferring heat, the practical temperature gradient is higher than the aforementioned requirement (lower bound).

Figure 6-1 provides a comparison for the worst-case scenario, where we contrast the lower bound efficiency of the SOFHE with the theoretical efficiency of Thermoelectric Generators (TEGs). It can be seen that the current stage of the SOFHE, which has not been fully optimized, demonstrates that it falls short in competing with TEGs in terms of efficiency. It is important to acknowledge that practical efficiency of TEGs is typically lower than their theoretical efficiency. Additionally, achieving the theoretical efficiency of TEGs requires the utilization of bulky heat sinks, which adversely affects their power density. Power density serves as a more relevant metric for evaluating the effectiveness of thermal energy harvesters since the heat source is typically not limiting, whereas size and cost are more significant constraints for harvesting applications.

By presenting these findings, it becomes apparent that further research and optimization are necessary to enhance the efficiency of the SOFHE and bring it closer to competing with TEGs. Moreover, the focus should be on improving the power density of the SOFHE, as this metric provides a more comprehensive evaluation of its performance as a thermal energy harvester. These insights contribute to the ongoing development and refinement of the SOFHE technology, paving the way for its potential integration into various applications in the IoT.

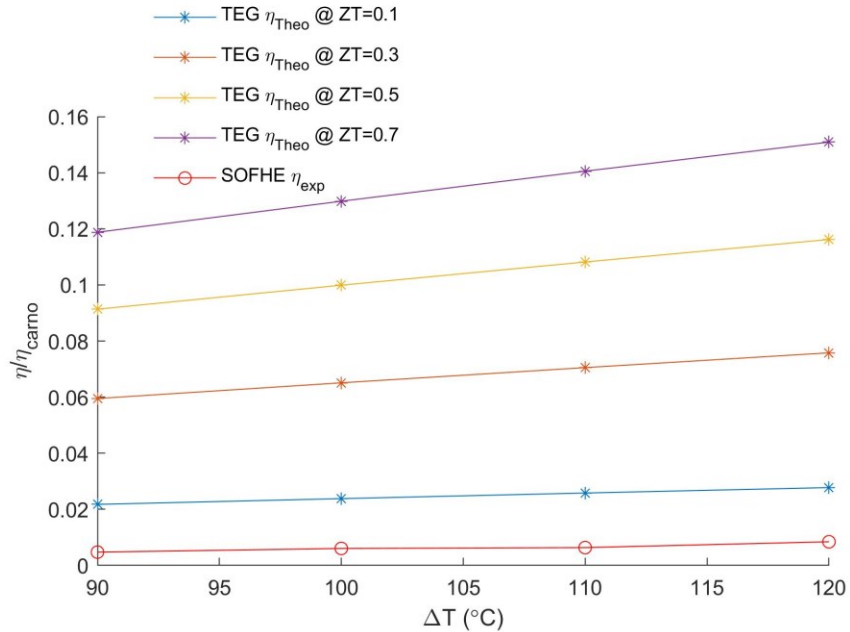


Figure 6-1 The second law efficiency of TEGs (theoretical) at different effective figure-of-merit ( $zT$ ) compared to that of the SOFHE (experimental).

In Table 6-1, a comparison of mechanical power density data from the literature is provided for various counterparts of the SOFHE. It is important to highlight that the reported power density for the SOFHE is not yet optimized and has potential for improvement. As discussed in Section 3.3.4, the power density of the SOFHE can be significantly enhanced by considering the effect of operating and design parameters. Therefore, it is essential to recognize that the power density figure presented for the SOFHE in Table 6-1 is just a starting point, and with further optimization and refinement, this technology holds great potential for achieving even higher power densities.

Table 6-1 Comparison of mechanical power density of the SOFHE with the literature.

micro heat engine	mechanical power density (mW/cm <sup>2</sup> )
P3 external combustion [7] [8]	10
phase change cavity by IMTEK [17][18]	0.016
bimetal strip HEATec [26][27][28]	2.7
SOFHE	0.05

## 6.2 How to design a better SOFHE

To achieve maximum mechanical power density with the SOFHE, it has been demonstrated that both the amplitude and frequency of the oscillations need to increase. The amplitude can be effectively enhanced by focusing on phase change enhancement, which can be achieved through the incorporation of wicking structures or by increasing the operating temperature. It is worth noting that, in addition to the intensity of the phase change rate, improving its phasing in relation to the position also contributes to enhancing the overall efficiency of the SOFHE (refer to Appendix B for more details on this aspect).

On the other hand, to increase the frequency of the oscillations (while maintaining the amplitude), the liquid length needs to be reduced. This reduction in the liquid length enables the

SOFHE to attain higher oscillation frequencies, thereby optimizing the overall performance of the system. Besides, shorter liquid length decreases friction that is favorable for efficiency.

### 6.3 Potential of the SOFHE for electrical power generation

To show the potential of the SOFHE in terms of generating electrical power, an example of coupling the SOFHE with an electromagnetic transducer is carried out hereby. The practice is for an idealized electromagnetic transducer that is impedance matched (real part) with the SOFHE. The effectiveness of electromagnetic vibration transducers hinges on the intricate design of electromagnetic coupling. Elements such as magnet size, material properties, and the geometric arrangement of the magnet, coil, and magnetic circuit are pivotal in the design phase. Faraday's law of induction underpins the transduction mechanism in these devices. According to this principle, altering magnetic flux ( $\phi_m$ ) through a conductive wire loop induces voltage in that loop. The induced voltage is the so-called electromotive force ( $\varepsilon$ ) which is given by [134]:

$$\varepsilon = - \frac{d\phi_m}{dt} \quad (6-1)$$

If we substitute the magnetic flux, then the induced voltage becomes:

$$\varepsilon = - \left( \frac{dA}{dt} B + \frac{dB}{dt} A \right) \quad (6-2)$$

This equation highlights a crucial point: in electromagnetic induction, the alteration of a magnetic field ( $B$ ) within a constant area ( $A$ ) or the change in area within a constant magnetic field yields the same result. Two basic arrangements are shown in Figure 6-2 [134].

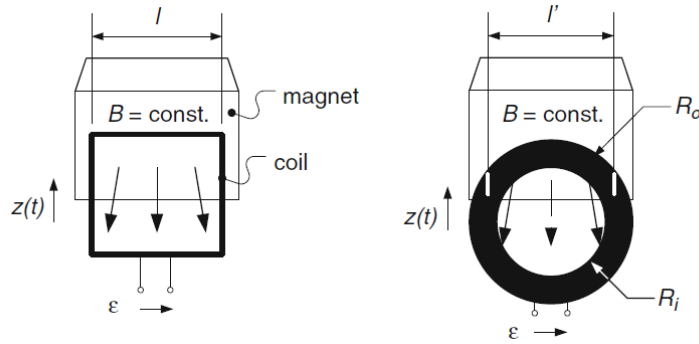


Figure 6-2 Two different shapes of coils moving towards a constant magnetic field [134].

For coils with  $N$  windings and rectangular cross section, the change of overlapping area is:

$$N \frac{dA}{dt} = Nl \frac{dz}{dt} = Nl\dot{z} \quad (6-3)$$

Thus, the *emf* voltage becomes:

$$\varepsilon = - NBl\dot{z} \quad (6-4)$$

Now Faraday's law can be extended using the chain rule:

$$\varepsilon = - \frac{d\phi_m}{dz} \cdot \frac{dz}{dt} = k_t \cdot \dot{z} \quad (6-5)$$

where  $k_t$  is the transduction factor or coupling coefficient:

$$k_t = NlB \quad (6-6)$$

The electrical circuit of the inductor can be presented as Figure 6-3. The ohmic loss of the load is typically represented by a resistor ( $R_{load}$ ) in series with the coil resistance ( $R_{coil}$ ) and coil inductance ( $L_{coil}$ ). For simplicity, the inductance of the coil is considered negligible which is valid for low frequency harvesters.

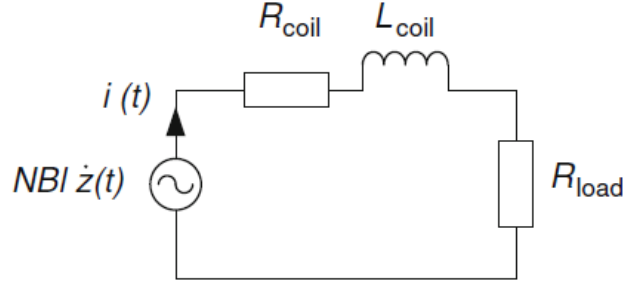


Figure 6-3 Electrical representation of the electromagnetic transducer [134].

The transduction factor ( $k_t$ ) relates the mechanical domain (input force and relative velocity of the mass) and the electromagnetic domain ( $emf$  and induced current). For closed circuit condition, the  $emf$  voltage will cause a current to flow. This current creates a magnetic field, which opposes the cause according to Lenz's law. The feedback electromechanical force is given by:

$$F_d = k_t i \quad (6-7)$$

or together with Faraday's law and Ohm's law:

$$F_d = \frac{k_t^2}{R_{coil} + R_{load}} \dot{z} \quad (6-8)$$

Hence, the dissipative feedback electromechanical force due to the transducer can be represented by a velocity proportional viscous damping element with the damping coefficient:

$$c_e = \frac{k_t^2}{R_{coil} + R_{load}} = \frac{(NlB)^2}{R_{coil} + R_{load}} \quad (6-9)$$

For the maximum power transfer between the SOFHE and the transducer, the electromechanical damping force coefficient must be matched with the optimum load coefficient for the SOFHE ( $c_{SOFHE}$ ).

$$c_{SOFHE} = c_e = \frac{k_t^2}{R_{coil} + R_{load}} = \frac{(NlB)^2}{R_{coil} + R_{load}} \quad (6-10)$$

The power can be now calculated:

$$Power = \frac{\varepsilon}{(R_{coil} + R_{load})^2} = \frac{k_t \dot{z}}{\left(\frac{k_t^2}{c_{SOFHE}}\right)^2} = \frac{(c_{SOFHE})^2 \dot{z}}{k_t^3} \quad (6-11)$$

The power is presented at different transduction factors as shown in Figure 6-4. The practice is carried out for the optimum load coefficient of the SOFHE at 10 g/s (experimentally measured

as presented in Figure 3-8). The velocity ( $\dot{z}$ ) at optimum load is 0.1 m/s (from experimental measurement of the amplitude and frequency for data points in Figure 3-8). As shown, lower transduction factor (0.2-0.3 T.m) yields higher electrical power while lower voltage. This practice can be carried out for electrostatic and piezoelectric transducers to compare their potential in terms of the electrical power generation.

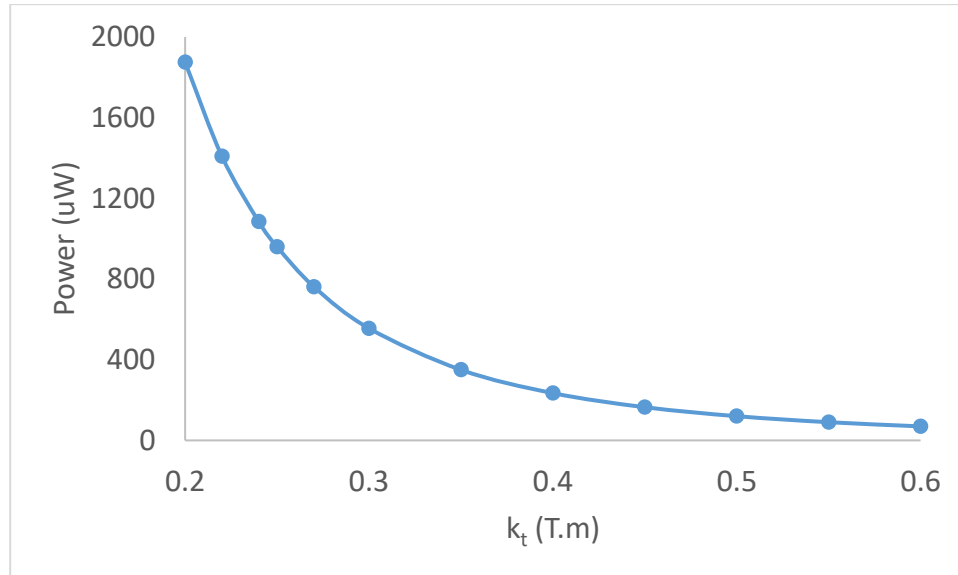


Figure 6-4 Electrical power as a function of the electromagnetic transduction factor ( $k_t=NBl$ ). The power is calculated by matching the real impedance of the SOFHE with an idealized electromagnetic transducer.

## 6.4 Impedance matching: coupling SOFHE

As emphasized in section 2.7, achieving impedance matching is crucial for maximizing power transfer from the SOFHE to the transducer. To facilitate this process, it is important to understand the forces and parameters that affect the impedance of the SOFHE, as outlined in Table 2-4. In Table 6-2, the impact of each force and parameter on the performance of the SOFHE is presented, providing valuable insights to guide future endeavors aimed at coupling the SOFHE with a selected transducer.

By referring to Table 6-2, researchers can gain a comprehensive understanding of how each force and parameter influences the performance of the SOFHE. This information serves as an operational guideline, enabling informed decision-making when it comes to selecting and optimizing the coupling between the SOFHE and a specific transducer. By considering these factors, researchers can enhance the impedance matching process, thus ensuring efficient power transfer and maximizing the overall performance of the system.

Table 6-2 Summarized effects of the parameters on the SOFHE performance to be used as a baseline for impedance matching.

Parameters of mechanical impedance		studied effect on SOFHE performance
	Heat source temperature (increase)	increase amplitude, increase friction, increase net work, increase power (section 3.3.4.1)
Evaporation-condensation rate	Fluid (latent heat, viscosity, surface tension, wettability)	more effective phase change profile with lower latent heat leading to higher power (see section 4.4.2 and 4.4.3) and higher efficiency (appendix B)
	Surface potential (hydrophilicity, surface tailored)	adding wicking fiber (section 3.3.4.2) and etched capillary path (section 5.3 and 5.4) increased amplitude and power
	adiabatic zone (increase length)	the phasing of the evaporation-condensation varies while amplitude remained almost constant (appendix C)
	Heat sink temperature	future work
Inertia	Liquid length (decrease) Diameter	amplitude constant, friction decrease, frequency increase, power density increase (section 3.3.4.3)
spring force	vapor length (decrease)	amplitude decrease, frequency increase, power decrease (appendix D)
Friction force	angular frequency (vapor length, liquid length, liquid density) fluid Diameter	Future work

## 6.5 Miniaturization of the SOFHE

The comparison of the mechanical power density between micro and meso scale SOFHEs, as presented in Table 5-1, reveals a decrease of approximately one order of magnitude in the micro scale. However, the significant fivefold increase in mechanical power achieved in the micro SOFHE through the enhancement of phase change by incorporating capillary paths is a promising outcome that can compensate for the negative effect of downsizing.

Optimizing the micro SOFHE design in terms of vapor bubble and liquid plug length presents an opportunity to further increase power density. The meso-scale experiments demonstrated that decreasing the liquid length leads to an increase in power density (as discussed in Section 3.3.4.3), while reducing the vapor length (as discussed in Appendix D) results in a decrease in power density (which can be mitigated by improving the phase change process).

In summary, while the mechanical power density of micro SOFHEs initially exhibits a decrease compared to meso-scale counterparts, the incorporation of capillary paths to enhance phase change demonstrates a remarkable fivefold increase in mechanical power. Further optimization can be achieved by improving the phase change process, for example, through surface tailoring, and by reducing the liquid length. These measures collectively contribute to the continuous improvement and augmentation of power density in micro SOFHEs.

## 6.6 SOFHE for pumping application

The mechanical power generated by the SOFHE can be effectively harnessed for applications requiring mechanical power, such as microfluidic pumping. Previous studies in the literature [51][117] have proposed the use of thermally-induced oscillatory flow for pumping applications. However, these studies utilized check valves, which resulted in a significant reduction in mechanical efficiency (by 50%). This reduction in efficiency stems from the check valves impeding the generated pressure.

To overcome this limitation and enhance the mechanical efficiency of the SOFHE, a valveless mechanism, such as an ejector or tesla valve, can be employed. In Figure 6-5, a proposed cross-sectional view of an ejector coupled with the SOFHE is depicted. This design can be 3D printed for practical implementation. The ejector consists of a nozzle that accelerates the flow, creating a jet directed towards the diffuser. In the diffuser, the inertia of the flow is maintained, and the diverging section of the diffuser converts the velocity of the flow into pressure.

It is important to note that a valveless mechanism introduces the challenge of backflow throughout the entire cycle. Therefore, in the design process, it is crucial to consider the lowest resistance in forward flow while ensuring the highest resistance in backward flow to minimize the impact of backflow. Parameters such as the length and diameter of the nozzle and diffuser, as well as the length of the diverging part of the diffuser, need to be optimized to achieve optimal performance.

By implementing a valveless mechanism, such as the proposed ejector, in conjunction with the SOFHE, the mechanical power output can be effectively utilized for microfluidic pumping applications. This approach offers the advantage of maintaining the generated pressure without the need for check valves, thereby enhancing the overall mechanical efficiency of the system.

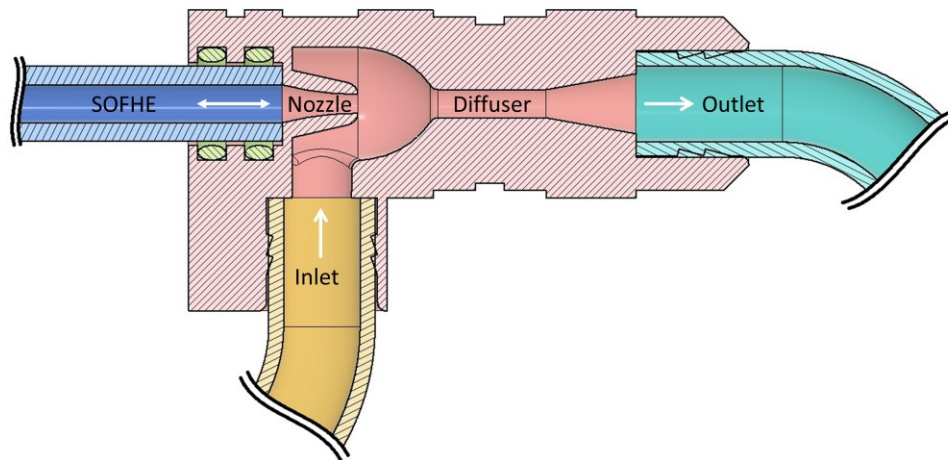


Figure 6-5 Cross-section view of the proposed ejector for the SOFHE for pumping application.



# Chapter 7

## Conclusion

### 7.1. Contributions

In summary, my Ph.D. research aims to advance the understanding and design of the Self-Oscillating Fluidic micro Heat Engine (SOFHE) for thermal energy harvesting. By analyzing the thermodynamic cycle and phase change mechanism, I have identified key parameters influencing the generated mechanical power. These findings provide valuable insights for optimizing the SOFHE performance and its potential application in powering low-power wireless sensors for the Internet of Things.

The primary objective of my research is to develop an optimized design for the SOFHE and investigate the influence of various parameters that play a crucial role in its performance. This investigation is vital as it sets the foundation for the subsequent step of integrating the SOFHE with a transducer. By comprehending the thermodynamic cycle (P-V diagram) of the SOFHE, I aim to shed light on how the unique oscillating vapor bubble-liquid plug behaves under mechanical loads and identify the impact of design parameters on the generated mechanical power.

To address these research questions, I introduced a variable mechanical load to the SOFHE, simulating the dissipative mechanical force encountered by the transducer. Through a comprehensive analysis of the thermodynamic cycle, considering the operating heat source temperature and two design parameters (namely the fiber length inside the evaporator, which enhances the phase-change mechanism, and the liquid plug length), I discovered several significant findings. Firstly, I observed a substantial improvement in mechanical power density by increasing the heat source temperature and enhancing the phase-change process, while decreasing the liquid length. These factors collectively contribute to enhancing the overall performance of the SOFHE.

The results demonstrate a remarkable achievement, highlighting a maximum mechanical power density of  $0.5 \text{ mW/cm}^3$  under an optimal load. Furthermore, the cycle efficiency ratio, relative to Carnot, was determined to be 30% (in an energy-efficient system). These outcomes illustrate the significant potential of the SOFHE as a promising technology for powering a wide range of low-power wireless sensors used in IoT applications. However, it is important to note that the successful implementation of this technology for IoT purposes hinges on ensuring appropriate electro-mechanical coupling in the design.

The phase change occurring within the SOFHE plays a crucial role in generating the driving force for the engine. This force arises from the change in mass of the vapor and is responsible for propelling the engine. In order to maximize the work done by the phase change force on the liquid plug, which in turn maximizes the oscillation amplitude, it is necessary for this force to be in phase with velocity. Ideally, a phase-change rate that is synchronized with the position would result in a force that is optimally in phase with velocity. However, analysis of the phase-change rate as a function of position for the SOFHE reveals that the force is actually out of phase with velocity.

To address this issue and explore potential solutions, I conducted a study involving two different phase change mechanisms: one without the fiber and another with the fiber. Additionally, two different working fluids, water and ethanol, were examined. The aim was to manipulate the phase angle between the phase-change force and velocity to achieve optimal performance. To evaluate this phase angle, I analyzed the product of the phase change force and velocity over a cycle at various phase angles. By calculating the maximum work at the ideal phase angle, I established a dimensionless number called  $\phi$  (phi), which represents the ratio of the phase change work to the maximum work.

The analysis of the phase change profiles revealed that water exhibited a  $\phi$  number of 0.56, indicating room for further improvement in its phase change profile. On the other hand, ethanol demonstrated a  $\phi$  number of 0.99, indicating a highly efficient phase change profile. The implementation of a more efficient phase change profile resulted in a 2.5% increase in the second law efficiency of the SOFHE. This study provides valuable insights into the engineering of the phase change process to optimize oscillation amplitude, power output, and overall efficiency.

By understanding the relationship between phase change and engine performance, this research opens up new path for improving the design and operation of the SOFHE. Future endeavors are focused on further enhancing the phase change profile, which will ultimately lead to improved performance in terms of oscillation amplitude, power generation, and overall efficiency. To enhance control over the phase change process in terms of amplitude and phasing, the implementation of tailored wicking structures proves to be a promising technique. In order to incorporate such structures into the SOFHE, a novel design is proposed, utilizing a standard microfabrication process to create various wicking microstructures.

The initial design of the microscale SOFHE involves a square cross-section microchannel, which serves to emulate the role of a wicking fiber through the inclusion of sharp corners. To achieve further improvements in phase change enhancement, capillary paths of different widths are etched into the design using a two-level masking microfabrication process. It was observed that the incorporation of these etched capillary paths resulted in a twofold increase in the oscillation amplitude and subsequently a fivefold increase in mechanical power output.

The findings of this research present us with a better-optimized design for the SOFHE by leveraging the inclusion of wicking structures, as well as increasing the operating temperature and decreasing the length of the liquid plug. By incorporating tailored wicking structures and optimizing its design parameters, the proposed approach offers greater control and improved performance in the phase change process of the SOFHE. The research outcomes contribute to the advancement of the field and provide a foundation for future investigations to unlock the full potential of the SOFHE technology.

## **7.2. Deliverables**

The preliminary results on the experimental approach to measure the thermodynamic cycle and the analytical method to calculate work and mechanical power out of the cycle were shared with the community as a conference paper presented in International Symposium on Oscillating/Pulsating Heat Pipes, Daejeon, South Korea, Sep 25-28, 2019. The complete characterization at different operating temperatures with varying design parameters are published as a journal paper titled “Experimental Characterization of the Thermodynamic Cycle

of Self-Oscillating Fluidic Heat Engine (SOFHE) for Thermal Energy Harvesting” in the journal of Energy Conversion and Management, 258 (2022) 115548.

The technique of using a wicking fiber to enhance phase change in an oscillatory two-phase plug flow is presented at the 28th International Workshop on Thermal Investigation of ICs and Systems (THERMINIC 2022), in Dublin, Ireland, September 2022. I was awarded as the best young presenter for this paper. The paper is published as a conference proceeding titled: “Time-Resolved Measurement of Enhanced Phase Change by a Fiber in an Oscillating Two-Phase Plug Flow”. The proposed method to evaluate the effectiveness of the phase change in such an oscillatory flow is published as a journal paper titled “Importance of Phase Change Timing in a Self-Sustained Oscillatory Flow” in the International Journal of Heat and Mass Transfer, 213 (2023) 124327.

The fabrication and testing of the new miniaturized phase change enhanced version of the SOFHE is shared with the community at the 21st International Conference on Micro and Nanotechnology for Power Generation and Energy Conversion Applications (POWERMEMS 2022), in Utah, USA, December 2022. The further phase change enhancement by adding capillary path to the design of the micro-SOFHE is submitted as an extension of the conference to a special issue offered by the POWERMEMS in the Journal of Micromechanics and Microengineering.

### **7.3. Other scientific contributions**

I also had the chance to contribute to other scientific publications, in collaboration with my colleague A. Nikkhah, that is on the numerical modeling of the friction force in the SOFHE [111] and deposition of the thin liquid film from an oscillating meniscus in a capillary tube [62].

### **7.4. Future research**

During my PhD research, I focused on understanding and characterizing the SOFHE. While I investigated several design and operating parameters, there are still a couple that remain to be explored. In the short term, it would be valuable to examine the effects of the following parameters on the performance of the SOFHE:

- Thermal conductivity of the wall: Analyzing how varying the thermal conductivity of the engine's wall affects its performance.
- Testing a wider range of working fluids: Investigating the influence of different working fluids on the efficiency and power output of the SOFHE.
- Effect of diameter: Exploring the impact of varying the diameter of the microchannel on the engine's performance.
- Friction reduction without decreasing amplitude (excluding the liquid length): Identifying techniques to reduce friction within the SOFHE without compromising the oscillation amplitude.

In the long term, I propose three promising research lines:

- Design and optimization of tailored wicking structures: Further enhancing control over the phase change process by developing and optimizing different types of tailored wicking structures for the SOFHE.

- Development of a compatible transducer: Building upon the knowledge gained about the SOFHE, focusing on designing a compatible transducer and establishing a strong coupling between the two components.
- Design and optimization of an ejector or Tesla valve: Exploring the potential of integrating an ejector or Tesla valve into the SOFHE, providing new avenues for applications such as microfluidic pumps.

By pursuing these long-term research lines, we can continue to advance the understanding and application of the SOFHE technology, optimizing its performance and exploring new possibilities for its use in various fields.



# Chapter 8

## Conclusion française

### 8.1. Contributions

En résumé, ma recherche de doctorat vise à faire progresser la compréhension et la conception du micro-moteur thermique fluide auto-oscillant (SOFHE en anglais) pour la récolte d'énergie thermique. En analysant le cycle thermodynamique et le mécanisme de changement de phase, j'ai identifié les paramètres clés qui influencent la puissance mécanique générée. Ces résultats fournissent des indications précieuses pour l'optimisation des performances du SOFHE et son application potentielle dans l'alimentation de capteurs sans fil de faible puissance pour l'Internet des objets.

L'objectif principal de ma recherche est de développer une conception optimisée pour le SOFHE et d'étudier l'influence de divers paramètres qui jouent un rôle crucial dans ses performances. Cette étude est essentielle car elle jette les bases de l'étape suivante, à savoir l'intégration de la SOFHE à un transducteur. En comprenant le cycle thermodynamique (diagramme P-V) de la SOFHE, je vise à mettre en lumière la façon dont la bulle de vapeur oscillante et le bouchon liquide se comportent sous des charges mécaniques et à identifier l'impact des paramètres de conception sur la puissance mécanique générée.

Pour répondre à ces questions de recherche, j'ai introduit une charge mécanique variable dans le SOFHE, simulant la force mécanique dissipative rencontrée par le transducteur. Grâce à une analyse complète du cycle thermodynamique, en tenant compte de la température de la source de chaleur et de deux paramètres de conception (à savoir la longueur de la fibre à l'intérieur de l'évaporateur, qui améliore le mécanisme de changement de phase, et la longueur du bouchon liquide), j'ai découvert plusieurs résultats significatifs. Tout d'abord, j'ai observé une amélioration substantielle de la densité de puissance mécanique en augmentant la température de la source de chaleur et en améliorant le processus de changement de phase, tout en diminuant la longueur du liquide. Ces facteurs contribuent collectivement à l'amélioration des performances globales de la technologie SOFHE.

Les résultats démontrent une réussite remarquable, mettant en évidence une densité de puissance mécanique maximale de  $0,5 \text{ mW/cm}^3$  sous une charge optimale. En outre, le taux d'efficacité du cycle, par rapport à Carnot, a été déterminé à 30 % (dans un système à haut rendement énergétique). Ces résultats illustrent le potentiel significatif du SOFHE en tant que technologie prometteuse pour l'alimentation d'une large gamme de capteurs sans fil à faible consommation utilisés dans les applications IoT. Cependant, il est important de noter que la mise en œuvre réussie de cette technologie à des fins d'IoT dépend de la garantie d'un couplage électromécanique approprié lors de la conception.

Le changement de phase qui se produit dans le SOFHE joue un rôle crucial dans la génération de la force motrice du moteur. Cette force provient du changement de masse de la vapeur et est responsable de la propulsion du moteur. Afin de maximiser le travail effectué par la force de changement de phase sur le bouchon liquide, ce qui maximise l'amplitude de l'oscillation, il est nécessaire que cette force soit en phase avec la vitesse. Idéalement, un taux de changement de

phase synchronisé avec la position se traduirait par une force en phase optimale avec la vitesse. Cependant, l'analyse du taux de changement de phase en fonction de la position pour le SOFHE révèle que la force est en fait déphasée par rapport à la vitesse.

Pour aborder cette question et explorer des solutions potentielles, j'ai mené une étude impliquant deux mécanismes de changement de phase différents : l'un sans la fibre et l'autre avec la fibre. En outre, deux fluides de travail différents, l'eau et l'éthanol, ont été examinés. L'objectif était de manipuler l'angle de phase entre la force de changement de phase et la vitesse afin d'obtenir des performances optimales. Pour évaluer cet angle de phase, j'ai analysé le produit de la force de changement de phase et de la vitesse sur un cycle à différents angles de phase. En calculant le travail maximal à l'angle de phase idéal, j'ai établi un nombre sans dimension appelé  $\phi$  (phi), qui représente le rapport entre le travail de changement de phase et le travail maximal.

L'analyse des profils de changement de phase a révélé que l'eau présentait un indice  $\phi$  de 0,56, ce qui indique que son profil de changement de phase peut encore être amélioré. En revanche, l'éthanol présentait un indice  $\phi$  de 0,99, ce qui indique un profil de changement de phase très efficace. La mise en œuvre d'un profil de changement de phase plus efficace a entraîné une augmentation de 2,5 % de l'efficacité de la deuxième loi de la SOFHE. Cette étude fournit des indications précieuses sur l'ingénierie du processus de changement de phase afin d'optimiser l'amplitude de l'oscillation, la puissance de sortie et l'efficacité globale.

En comprenant la relation entre le changement de phase et les performances du moteur, cette recherche ouvre une nouvelle voie pour améliorer la conception et le fonctionnement du SOFHE. Les efforts futurs se concentrent sur l'amélioration du profil de changement de phase, ce qui conduira finalement à une amélioration des performances en termes d'amplitude d'oscillation, de production d'énergie et d'efficacité globale. Pour améliorer le contrôle du processus de changement de phase en termes d'amplitude et de phasage, la mise en œuvre de structures de mèche sur mesure s'avère être une technique prometteuse. Afin d'incorporer de telles structures dans le SOFHE, une nouvelle conception est proposée, utilisant un processus de microfabrication standard pour créer diverses microstructures de mèche.

La conception initiale du SOFHE à l'échelle microscopique comprend un microcanal à section carrée, qui sert à émuler le rôle d'une fibre de mèche grâce à l'inclusion d'angles aigus. Pour améliorer encore le changement de phase, des chemins capillaires de différentes largeurs sont gravés dans la conception à l'aide d'un processus de microfabrication à deux niveaux de masquage. Il a été observé que l'incorporation de ces chemins capillaires gravés a permis de multiplier par deux l'amplitude de l'oscillation et, par la suite, de multiplier par cinq la puissance mécanique de sortie.

Les résultats de cette recherche nous présentent une conception mieux optimisée pour le SOFHE en tirant parti de l'inclusion de structures de mèche, ainsi qu'en augmentant la température de fonctionnement et en diminuant la longueur du bouchon liquide. En incorporant des structures de mèche sur mesure et en optimisant ses paramètres de conception, l'approche proposée offre un meilleur contrôle et de meilleures performances dans le processus de changement de phase du SOFHE. Les résultats de la recherche contribuent à l'avancement du domaine et fournissent une base pour les recherches futures afin de libérer tout le potentiel de la technologie SOFHE.

## 8.2. Deliverables

Les résultats préliminaires de l'approche expérimentale pour mesurer le cycle thermodynamique et la méthode analytique pour calculer le travail et la puissance mécanique du cycle ont été partagés avec la communauté sous la forme d'un article de conférence présenté lors du Symposium international sur les caloducs oscillants/pulsants, Daejeon, Corée du Sud, 25-28 septembre 2019. La caractérisation complète à différentes températures de fonctionnement avec des paramètres de conception variables est publiée dans un article de revue intitulé "Experimental Characterization of the Thermodynamic Cycle of Self-Oscillating Fluidic Heat Engine (SOFHE) for Thermal Energy Harvesting" dans le journal of Energy Conversion and Management, 258 (2022) 115548.

La technique d'utilisation d'une fibre mèche pour améliorer le changement de phase dans un écoulement oscillatoire à deux phases est présentée au 28<sup>e</sup> atelier international sur l'étude thermique des circuits intégrés et des systèmes (THERMINIC 2022), à Dublin, en Irlande, en septembre 2022. J'ai reçu le prix du meilleur jeune présentateur pour cet article. L'article est publié dans le cadre d'une conférence intitulée "Time-Resolved Measurement of Enhanced Phase Change by a Fiber in an Oscillating Two-Phase Plug Flow" (Mesure résolue dans le temps de l'amélioration du changement de phase par une fibre dans un écoulement oscillant à deux phases). La méthode proposée pour évaluer l'efficacité du changement de phase dans un tel écoulement oscillatoire est publiée dans un article de revue intitulé "Importance of Phase Change Timing in a Self-Sustained Oscillatory Flow" dans l'International Journal of Heat and Mass Transfer, 213 (2023) 124327.

La fabrication et les essais de la nouvelle version miniaturisée à changement de phase du SOFHE sont partagés avec la communauté lors de la 21<sup>e</sup> conférence internationale sur les micro et nanotechnologies pour la production d'énergie et les applications de conversion d'énergie (POWERMEMS 2022), dans l'Utah, aux États-Unis, en décembre 2022. L'amélioration du changement de phase par l'ajout d'un chemin capillaire à la conception de la micro-SOFHE est soumise comme extension de la conférence à un numéro spécial offert par le POWERMEMS dans le Journal of Micromechanics and Microengineering.

## 8.3. Autres contributions scientifiques

J'ai également eu la chance de contribuer à d'autres publications scientifiques, en collaboration avec mon collègue A. Nikkhah, sur la modélisation numérique de la force de frottement dans le SOFHE [111] et dépôt du film liquide mince à partir d'un ménisque oscillant dans un tube capillaire [62].

## 8.4. Recherches futures

Au cours de mes recherches doctorales, je me suis attaché à comprendre et à caractériser le SOFHE. Bien que j'aie étudié plusieurs paramètres de conception et de fonctionnement, il en reste encore quelques-uns à explorer. À court terme, il serait intéressant d'examiner les effets des paramètres suivants sur les performances de la SOFHE:

- Conductivité thermique de la paroi : Analyse de l'influence de la variation de la conductivité thermique de la paroi du moteur sur ses performances.

- Essai d'une plus large gamme de fluides de travail : étude de l'influence de différents fluides de travail sur l'efficacité et la puissance de la SOFHE.
- Effet du diamètre : Exploration de l'impact de la variation du diamètre du microcanal sur les performances du moteur.
- Réduction du frottement sans diminution de l'amplitude (à l'exclusion de la longueur du liquide) : Identifier les techniques permettant de réduire les frottements dans le SOFHE sans compromettre l'amplitude de l'oscillation.

À long terme, je propose trois axes de recherche prometteurs:

- Conception et optimisation de structures de mèche sur mesure : Améliorer encore le contrôle du processus de changement de phase en développant et en optimisant différents types de structures de mèche sur mesure pour le SOFHE.
- Développement d'un transducteur compatible : En s'appuyant sur les connaissances acquises sur le SOFHE, se concentrer sur la conception d'un transducteur compatible et établir un couplage fort entre les deux composants.
- Conception et optimisation d'un éjecteur ou d'une valve Tesla : Exploration du potentiel d'intégration d'un éjecteur ou d'une valve Tesla dans le SOFHE, offrant de nouvelles possibilités d'applications telles que les pompes microfluidiques.

En poursuivant ces lignes de recherche à long terme, nous pouvons continuer à faire progresser la compréhension et l'application de la technologie SOFHE, en optimisant ses performances et en explorant de nouvelles possibilités d'utilisation dans divers domaines.



# Appendix A

## A. Details on the role of the wicking fiber

To better understand the role of the wicking fiber, we conducted a series of tests to change the length of the fiber inside the evaporator. The setup shown in section 3.2.2 and the experimental protocol described in section 3.2.2 are followed for this set of tests. The amplitude and pressure were measured at each fiber length to calculate the phase change rate.

### A.1. Amplitude of the phase change rate

Figure A.1 shows the phase change rate and the displacement of the oscillations as a function of time for different lengths of fiber inside the evaporator at  $T_v = 110^\circ\text{C}$ . The measured frequency of the oscillations is at 16 Hz. We observed a remarkable eightfold increase in the phase change rate from  $95 \mu\text{g/s}$  to  $825 \mu\text{g/s}$  at the shortest (1.7cm) and the longest (5.5cm) fiber lengths, respectively. This is explained by the fact that the fiber creates two corners with the glass tube (section 4.3.2) acting as angular capillaries pumping liquid from the liquid plug towards the evaporator. Therefore, a long thin film with a low thermal resistance forms along the fiber that facilitates the evaporation rate. This initiates the start-up and yields stable oscillations with a constant amplitude. As we increase the length of the fiber, the phase change rate experiences a significant increase until the  $L_{fiber} = 3\text{cm}$ . From that length onwards, the amplitude of the phase change rate remains almost constant. This is because of the limited pumping capacity by wicking action. We verified that by measuring the length of the thin film that exists only 3-4 cm along the fiber even if the length of fiber in the evaporator is higher. We monitored the thin film around the fiber throughout the experiments and it never dries out.

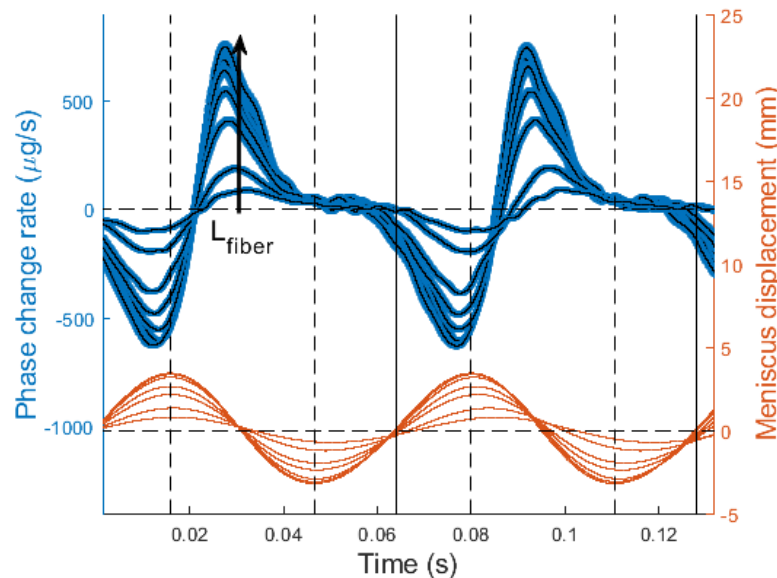


Figure A.1 Enhancement of the phase change rate and the displacement as a function of time at different  $L_{fiber}$ .

## A.2. Oscillation amplitude

Figure A.2 shows the oscillation amplitude as a function of the fiber length inside the evaporator. We observed a fourfold increase in the oscillation amplitude from 1.5mm to 6.6mm as a result of the phase change augmentation by the fiber. We can see that the slope is steeper at lower fiber length due to the higher sensitivity of the phase change rate. This curve is reminiscent of the theoretical bifurcation diagram showed in [59]. When there is no fiber, we have no start-up while it will start oscillating once the fiber is inserted for less than a few millimeters. However, the graph shows a plateau at higher fiber length that is attributed to the end of the thin film because of the limited wicking capacity.

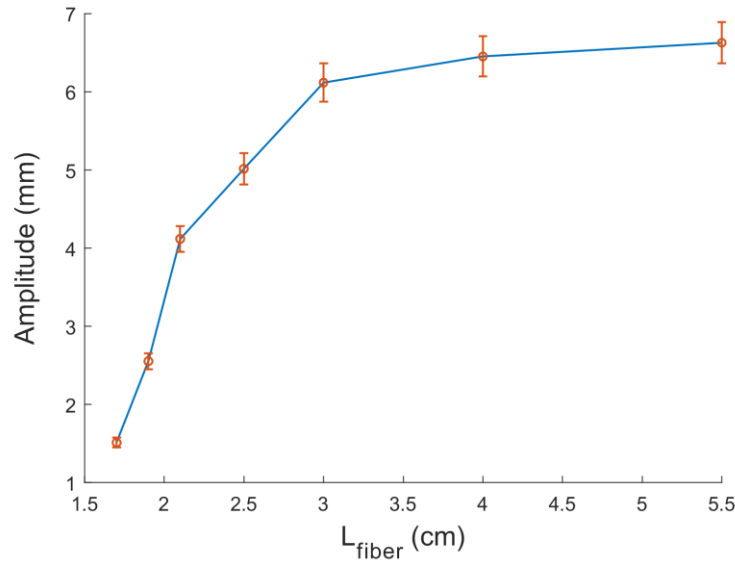
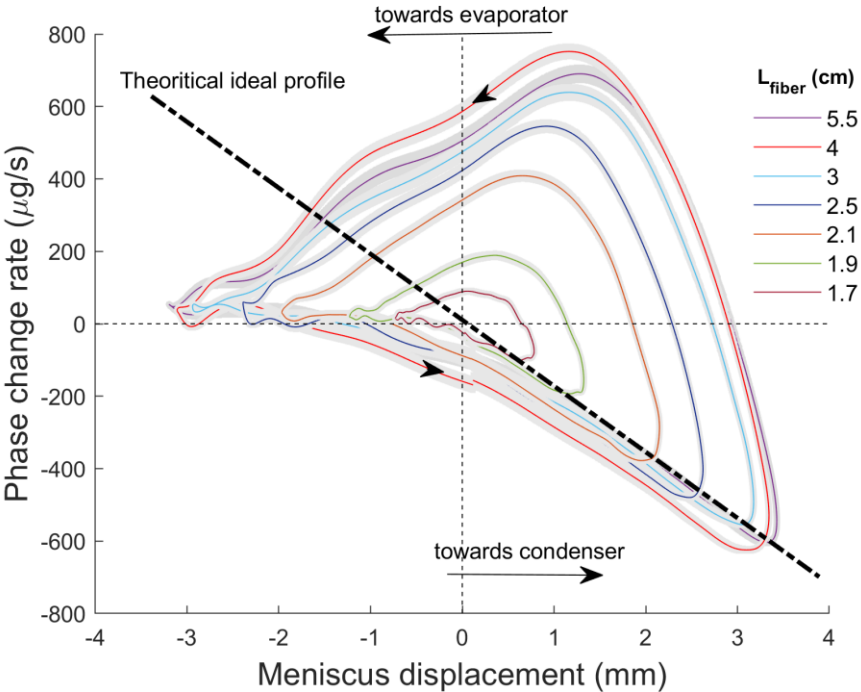


Figure A.2 Increase of the amplitude of oscillations by increasing the fiber length,  $L_{\text{fiber}}$ .

## A.3. Phasing of the phase change rate

As discussed by Tessier-Poirier *et al.* [48], a phase change profile that is completely out of phase with position produces a force in phase with velocity which in turn increases the amplitude of motion. One example of a phase change profile that yields such an ideal phasing is a linear one discussed in more details in Tessier-Poirier *et al.* [48]. In their model, the evaporation is considered only from the oscillating meniscus that is a function of the thermal resistance and the temperature difference between the wall and the saturation temperature at liquid-vapor interface. This simplified model can very well describe the effect of the phase change on the system's dynamics. They concluded that to keep the system unstable for self-oscillations, we need an oscillating net phase change that has to be out of phase with position (linear profile). The more the force is in phase with velocity, the more energy is injected into the system which in turn increases the amplitude of the oscillations. To see how the phase change profile evolves as the meniscus oscillates between the evaporator and the condenser; we plotted the phase change versus the meniscus displacement in Fig. A.3. As shown, the phase change profile in the presence of the fiber is far from a linear profile. Therefore, adding the fiber contributes to increasing the amplitude of the phase change profile by pumping liquid into the evaporator and having more evaporation while its phasing with motion still has room for further improvement.

This graph also shows that the fiber length does not affect the phasing of the phase change rate with respect to the position. The phase-change effectiveness number ( $\varphi$ ) varies between 0.4-0.5 for all the fiber length. Therefore, fiber length only changes the amplitude of the phase change rate not the its phasing with respect to the position.



A.3 The experimental measured phase change profile resulting from the evaporation-condensation, as a function of the displacement, at different  $L_{\text{fiber}}$  compared to the theoretical ideal profile discussed in [48].

# Appendix B

## B. Effect of phasing on SOFHE efficiency

A more effective phase change profile for ethanol compared to water (see section 4.3.2 and 4.3.3) leads to a 10% increase in the thermodynamic efficiency and 2.5% increase in the second law efficiency. The thermodynamic efficiency and second law efficiency of the SOFHE calculation is explained section 3.3.3.

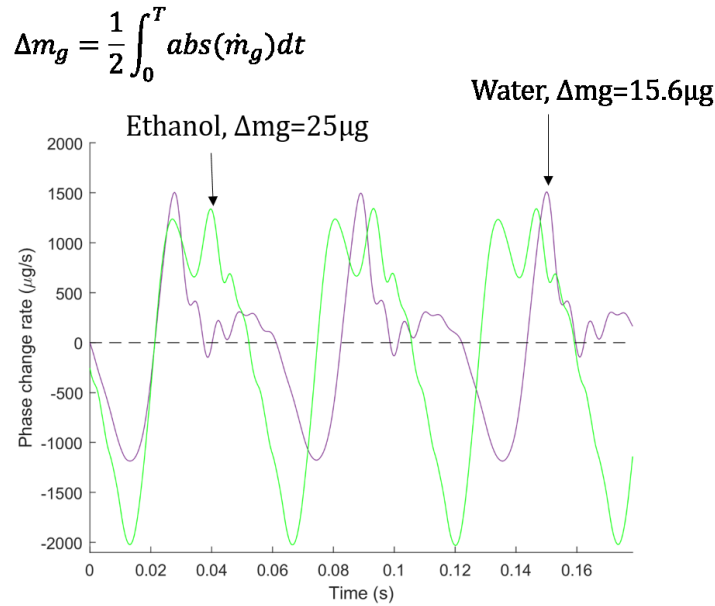


Figure B.1 The phase change rate as a function of time with water and ethanol as the working fluid.

Table B.1 Comparison of the thermodynamic and second law efficiency for water and ethanol with a more effective phase change profile.

	water	ethanol
$Q_{in,w} = m_g * h_{fg}$	$15.6(\mu\text{g}) * 2260(\text{J/g}) = 0.0353\text{J}$	$25(\mu\text{g}) * 846(\text{J/g}) = 0.0213\text{J}$
$W_{net}$	$0.245 * 10^{-3}$	$0.193 * 10^{-3}$
$\eta = \frac{W_{net}}{Q_{in}}$	0.69%	0.9%
$\eta_{Carnot}$	$\frac{140-20}{273+140} = 0.291 = 29.1\%$	$\frac{89-20}{273+89} = 0.191 = 19.1\%$
$\eta_{ratio}$	2.3 %	4.7 %

# Appendix C

## C. Effect of the adiabatic distance on phase change

This appendix is on the effect of the adiabatic length ( $L_{adb}$ ) on the SOFHE performance. The tests are carried out using the experimental setup described in section 4.2 with similar test procedure. To adjust the adiabatic distance, the bottom Peek insulating part with a slot is used. We tested two adiabatic distances at 1, and 10 mm at heat source temperatures  $T_H=140$  °C, liquid length 9 cm, and vapor length 6 cm. A small difference in the amplitude (from 11.9 to 12.2 mm) is recorded. The phase change profile and the phase-change effectiveness number ( $\phi$ ) are presented in Figure C.1. Varying the adiabatic length changes the shape of the phase change profile but the effectiveness number remains almost constant (0.9 for  $L_{adb}=2$  mm and 0.85 for  $L_{adb}=10$  mm). The amplitude of the phase change rate (the inset graph in Figure C.1) is at 4.9 and 5.2  $\mu\text{g/s}$ . The adiabatic length changes the temperature profile that is seen by the oscillating meniscus where mostly condensation happens. In the presence of the wicking fiber, the evaporation mostly happens from the thin film around the fiber in the hot zone that is less dependent on the temperature gradient at the adiabatic zone. For the shorter adiabatic length from A to B and vice versa, the rate of condensation is higher since the meniscus touches the tube wall that is in contact with the cold block. The higher condensation is not favorable for forward motion while it contributes to the backward motion. For the longer length, it is the exact opposite. Having less condensation during forward motion that is desirable while less condensation on backward motion that is not efficient.

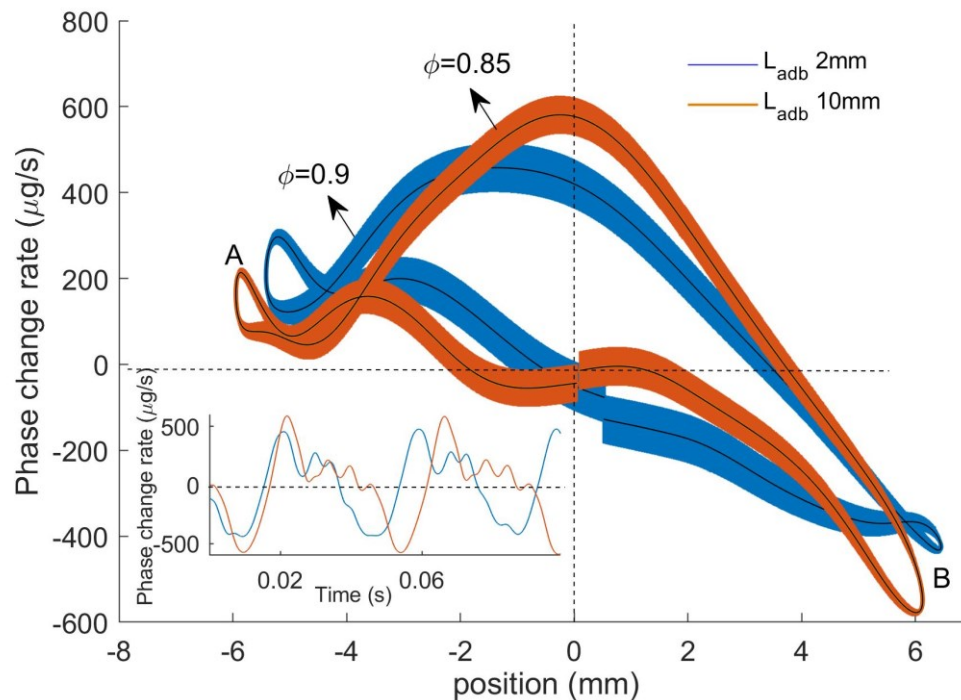


Figure C.1 Phase change rate as a function of position (and time as an inset) at two different adiabatic lengths 2 and 10 mm.

# Appendix D

## D. Effect of vapor length

Theoretically, the SOFHE power is proportional to the square of amplitude and frequency. However, it is not clear how amplitude and frequency, and consequently the power, is affected as we change the length of the heated zone (that mostly equals to the length of the vapor bubble). In this paper, the length of the heated zone is experimentally varied and the pressure, amplitude, and frequency measurements are carried out to evaluate the power of SOFHE.

### D.1. Experiments

To carry out the test, the experimental setup described in section 4.2 is used. To adjust the length of the heated zone that equals the vapor length, tube supports at different lengths are used. The test protocol described in section 4.2 is followed. The tests are carried out at four evaporator lengths ( $L_v$ ) of 7, 5, 3, and 1 cm while keeping the fiber length at 1 cm inside the evaporator, the heat source temperature at 120°C, the liquid length ( $L_l$ ) at 5.5 cm, and the adiabatic length at 4 mm. The total volume of the SOFHE equals the product of the cross-section area ( $A=\pi D_{out}^2/4$ ) and the total length ( $L_T=L_v+L_l$ ) that varies between 1.6 and 0.8 cm<sup>3</sup> depending the length of the evaporator.

### D.2. Results

#### D.2.1. Amplitude and Frequency

Figure D.1 shows that as the evaporator length decreases from 7 cm to 1 cm, the peak-to-peak amplitude of the oscillations decreases from 5.9 to 1.5 mm while the frequency increases from 27 to 52 Hz. The variation of frequency with evaporator length is in agreement with the natural frequency of the equivalent mass-spring system in which the frequency is inversely proportional to the square of vapor length [48]. To explain the decrease of the amplitude, we need to calculate the net evaporation rate on which the amplitude is highly dependent [115,120]. The net evaporation rate is discussed in section D.2.2.

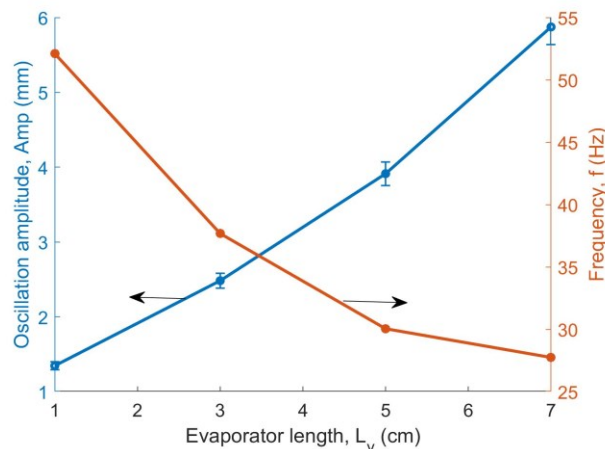


Figure D.1 The frequency and oscillation amplitude of the SOFHE as a function of the evaporator length.

### D.2.2. Net Evaporation Rate

The net evaporation rate (rate of change of vapor mass) is calculated using the ideal gas law ( $m_v = RT_v/P_v V_v$ ) and experimental data on pressure ( $P_v$ ), volume ( $V_v$ ), and temperature ( $T_v$ ) [120]. Figure D.2 shows the net evaporation rate as a function of time at four different evaporator lengths. The negative and positive values show net condensation and net evaporation, respectively. The results show the decrease of net evaporation rate (peak-to-peak amplitude decreases from 1027 to 242  $\mu\text{g/s}$ ) as the evaporator length decreases leading to the decrease of the amplitude.

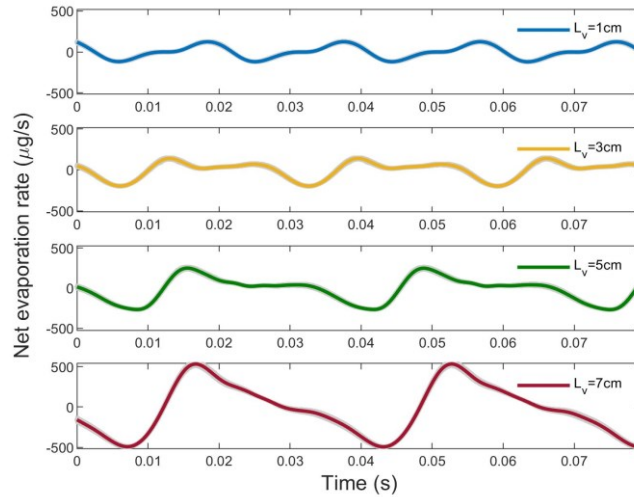


Figure D.2 The net evaporation rate as a function of time for four different evaporator lengths.

### D.2.3. Work and power

To evaluate how the variation of amplitude and frequency affect the power of SOFHE, the thermodynamic cycle ( $P_v$ - $V_v$ ) of SOFHE at different evaporator lengths are plotted in Figure D.3. The integration of the area in the  $P_v$ - $V_v$  curve yields the work done in each cycle. The cycles shrink as the evaporator length decreases leading to a decrease in the thermodynamic work per cycle. It is shown that for SOFHE at optimum load, nearly half of the thermodynamic work per cycle is used to overcome the viscous friction [115]. Therefore, the available net work per cycle that can be harvested by a transducer can be estimated as half of the thermodynamic cycle work. The power of SOFHE is the product of the net work per cycle and frequency. As Tessier-Poirier showed [48] [45], the generated power by SOFHE is from a velocity damped force ( $F_d = c\dot{x}$ ) created by the net evaporation rate (the change of mass of vapor). Theoretically, the power from this force in an oscillating motion ( $x = A \sin(\omega t)$ ) is proportional to the square of amplitude and frequency ( $\text{Power} = cA^2\omega^2/2$ ). Figure D.4 shows the power of SOFHE as a function of the evaporator length. A decreasing trend for power shows that the negative effect of decreasing evaporator length on the amplitude overcome the positive effect of frequency increase. However, at smaller evaporator length, the slope of the graph flattens implying the fact that the power is less and less dependent on the evaporator length.

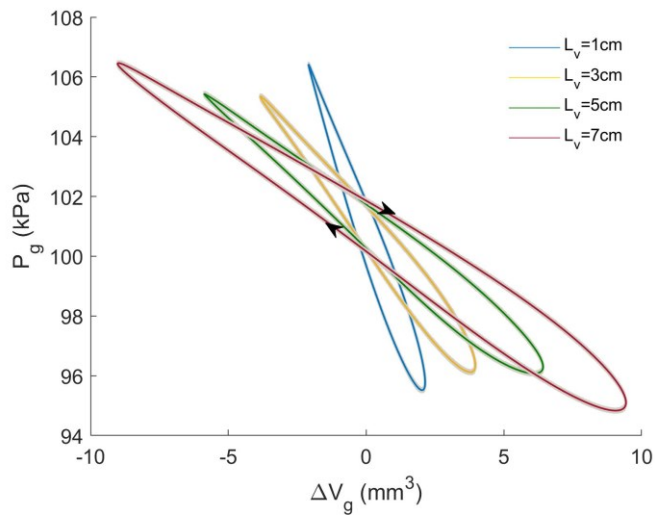


Figure D.3 Thermodynamic cycle ( $P_v$ - $V_v$ ) of SOFHE for four different evaporator lengths.

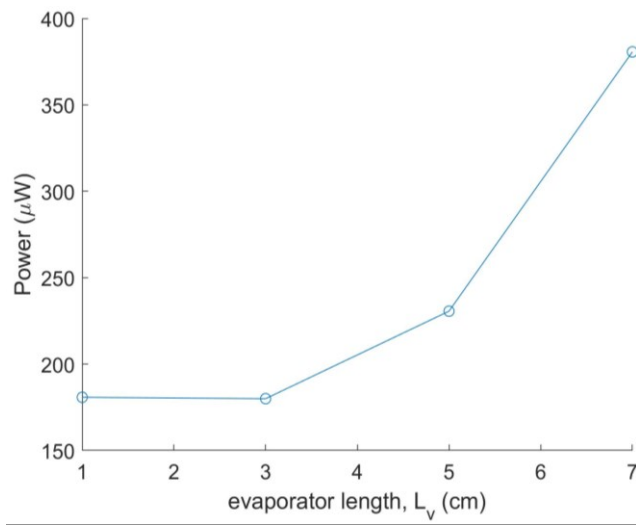


Figure D.4 Power of the SOFHE as a function of the evaporator length.



## References

- [1] Priya S, Inman DJ. Energy harvesting technologies. Springer US; 2009. <https://doi.org/10.1007/978-0-387-76464-1>.
- [2] Boisseau S, Despesse G, Ahmed B. Electrostatic Conversion for Vibration Energy Harvesting. Small-Scale Energy Harvest., InTech; 2012. <https://doi.org/10.5772/51360>.
- [3] Knight C, Davidson J. Thermal energy harvesting for wireless sensor nodes with case studies. Lect. Notes Electr. Eng., vol. 64 LNEE, Springer, Berlin, Heidelberg; 2010, p. 221–42. [https://doi.org/10.1007/978-3-642-12707-6\\_10](https://doi.org/10.1007/978-3-642-12707-6_10).
- [4] Monin T, Tessier-Poirier A, Léveillé E, Juneau-Fecteau A, Skotnicki T, Formosa F, et al. First experimental demonstration of a Self-Oscillating Fluidic Heat Engine (SOFHE) with piezoelectric power generation. J Phys Conf Ser 2016;773:12039. <https://doi.org/10.1088/1742-6596/773/1/012039>.
- [5] Snyder GJ, Toberer ES. Complex thermoelectric materials. Nat Mater 2008;7:101–10. [https://doi.org/10.1142/9789814317665\\_0016](https://doi.org/10.1142/9789814317665_0016).
- [6] Salamon N. Development of thermal energy harvesting systems. Université Grenoble Alpes, 2018. <https://doi.org/https://tel.archives-ouvertes.fr/tel-01797966>.
- [7] Xu C, Hall J, Richards C, Bahr D, Richards R. Design of a micro heat engine. ASME Int Mech Eng Congr Expo Proc 2000;2000-AB:261–7. <https://doi.org/10.1115/IMECE2000-1101>.
- [8] Whalen S, Thompson M, Bahr D, Richards C, Richards R. Design, fabrication and testing of the P3 micro heat engine. Sensors Actuators, A Phys 2003;104:290–8. [https://doi.org/10.1016/S0924-4247\(03\)00032-3](https://doi.org/10.1016/S0924-4247(03)00032-3).
- [9] Whalen SA, Won SY, Richards RF, Bahr DF, Richards CD. Characterization and modeling of a liquid-vapor phase change membrane actuator with an integrated SU-8 micro capillary wicking structure. Dig. Tech. Pap. - Int. Conf. Solid State Sensors Actuators Microsystems, TRANSDUCERS '05, vol. 1, 2005, p. 342–7. <https://doi.org/10.1109/SENSOR.2005.1496426>.
- [10] Whalen SA, Richards CD, Bahr DF, Richards RF. Characterization and modeling of a microcapillary driven liquid-vapor phase-change membrane actuator. Sensors Actuators, A Phys 2007;134:201–12. <https://doi.org/10.1016/j.sna.2006.04.038>.
- [11] Weiss LW, Cho JH, McNeil KE, Richards CD, Bahr DF, Richards RF. Characterization of a dynamic micro heat engine with integrated thermal switch. J Micromechanics Microengineering 2006;16. <https://doi.org/10.1088/0960-1317/16/9/S14>.
- [12] Cho JH, Weiss LW, Richards CD, Bahr DF, Richards RF. Power production by a dynamic micro heat engine with an integrated thermal switch. J Micromechanics Microengineering 2007;17. <https://doi.org/10.1088/0960-1317/17/9/S02>.
- [13] Cho J, Wiser T, Richards C, Bahr D, Richards R. Fabrication and characterization of a thermal switch. Sensors Actuators, A Phys 2007;133:55–63.

<https://doi.org/10.1016/j.sna.2006.03.033>.

- [14] Bardaweel HK, Anderson MJ, Richards RF, Richards CD. Optimization of the dynamic and thermal performance of a resonant micro heat engine. *J Micromechanics Microengineering* 2008;18. <https://doi.org/10.1088/0960-1317/18/10/104014>.
- [15] Bardaweel H, Richards R, Richards C, Anderson M. Characterization of the thermodynamic cycle of a MEMS-based external combustion resonant engine. *Microsyst Technol* 2012;18:693–701. <https://doi.org/10.1007/s00542-012-1496-y>.
- [16] Bardaweel H, Richards R, Anderson M, Richards C. Thermodynamic characterization & scaling of a MEMS heat engine. *PowerMEMS*, Washington DC, USA: 2009.
- [17] Huesgen T, Ruhhammer J, Biancuzzi G, Woias P. Detailed study of a micro heat engine for thermal energy harvesting. *J Micromechanics Microengineering* 2010;20:9. <https://doi.org/10.1088/0960-1317/20/10/104004>.
- [18] Huesgen T, Woias P. A novel self-starting MEMS-heat engine for thermal energy harvesting. *Proc. IEEE Int. Conf. Micro Electro Mech. Syst.*, 2010, p. 1179–82. <https://doi.org/10.1109/MEMSYS.2010.5442422>.
- [19] Epstein AH, Epstein AH, Jacobson SA, Protz JM, Fr chet te LG. Shirtbutton-sized gas turbines: the engineering challenges of micro high speed rotating machinery. *PROCEEDINGS, 8TH INT'L Symp Transp Phenom Dyn ROTATING Mach* 2000.
- [20] Epstein AH. Millimeter-scale, MEMS gas turbine engines. *Am. Soc. Mech. Eng. Int. Gas Turbine Institute, Turbo Expo IGTI*, vol. 4, 2003, p. 669–96. <https://doi.org/10.1115/GT2003-38866>.
- [21] Savoulides N, Jacobson SA, Li H, Ho L, Khanna R, Teo CJ, et al. Fabrication and testing of a high-speed microscale turbocharger. *J Microelectromechanical Syst* 2008;17:1270–82. <https://doi.org/10.1109/JMEMS.2008.924257>.
- [22] Fr chet te LG, Lee C, Arslan S, Liu YC. Design of a microfabricated rankine cycle steam turbine for power generation. *Am. Soc. Mech. Eng. Micro-Electromechanical Syst. Div. Publ.*, vol. 5, American Society of Mechanical Engineers; 2003, p. 335–44. <https://doi.org/10.1115/imece2003-42082>.
- [23] Annache A, Liamini M, Gauthier F, Beauchesne-Martel P, Omri M, Fr chet te LG. A MEMS Turbopump for High Temperature Rankine Micro Heat Engines - Part I: Design and Fabrication. *J Microelectromechanical Syst* 2020;29:1278–92. <https://doi.org/10.1109/JMEMS.2020.3008665>.
- [24] Annache A, Liamini M, Gauthier F, Beauchesne-Martel P, Omri M, Fr chet te LG. A MEMS Turbopump for High-Temperature Rankine Micro Heat Engines - Part II: Experimental Demonstration. *J Microelectromechanical Syst* 2020;29:1293–303. <https://doi.org/10.1109/JMEMS.2020.3008625>.
- [25] M ller N, Fr chet te LG. Performance analysis of Brayton and Rankine cycle microsystems for portable power generation. *ASME Int. Mech. Eng. Congr. Expo. Proc.*, New Orleans, USA,; 2002, p. 513–22. <https://doi.org/10.1115/IMECE2002-39628>.

- [26] Boughaleb J, Arnaud A, Guiffard B, Guyomar D, Seveno R, Monfray S, et al. Coupling of PZT thin films with bimetallic strip heat engines for thermal energy harvesting. *Sensors (Switzerland)* 2018;18:1–12. <https://doi.org/10.3390/s18061859>.
- [27] Boughaleb J, Arnaud A, Monfray S, Cottinet PJ, Quenard S, Boeuf F, et al. Coupling of a bimetallic strip heat engine with a piezoelectric transducer for thermal energy harvesting. *Mol Cryst Liq Cryst* 2016;628:15–22. <https://doi.org/10.1080/15421406.2015.1137390>.
- [28] Puscasu O, Monfray S, Savelli G, Maitre C, Pemeant JP, Coronel P, et al. An innovative heat harvesting technology (HEATec) for above-Seebeck performance. *Tech Dig - Int Electron Devices Meet IEDM* 2012:291–4. <https://doi.org/10.1109/IEDM.2012.6479031>.
- [29] Ravindran SKT, Kroener M, Shabaniyan A, Goldschmidtboeing F, Woias P. Analysis of a bimetallic micro heat engine for energy harvesting. *Smart Mater Struct* 2014;23. <https://doi.org/10.1088/0964-1726/23/3/035011>.
- [30] Karanilam S, Ravindran T, Kroener M, Woias P. A bimetallic micro heat engine for pyroelectric energy conversion. *Procedia Eng* 2012;47:33–6. <https://doi.org/10.1016/j.proeng.2012.09.077>.
- [31] Ravindran SKT, Nilkund P, Kroener M, Woias P. Thermal energy harvesting using an electrostatic generator. 2013 IEEE 26th Int. Conf. Micro Electro Mech. Syst., IEEE; 2013, p. 801–4. <https://doi.org/10.1109/MEMSYS.2013.6474364>.
- [32] Monroe JG, Bhandari M, Fairley J, Myers OJ, Shamsaei N, Thompson SM. Energy harvesting via thermo-piezoelectric transduction within a heated capillary. *Appl Phys Lett* 2017;111:043902. <https://doi.org/10.1063/1.4996235>.
- [33] Monroe JG, Vasquez ES, Aspin ZS, Walters KB, Berg MJ, Thompson SM. Electromagnetic induction by ferrofluid in an oscillating heat pipe. *Appl Phys Lett* 2015;106:263901. <https://doi.org/10.1063/1.4923400>.
- [34] Monroe JG, Ibrahim OT, Thompson SM, Shamsaei N. Energy harvesting via fluidic agitation of a magnet within an oscillating heat pipe. *Appl Therm Eng* 2018;129:884–92. <https://doi.org/10.1016/j.applthermaleng.2017.10.076>.
- [35] Shen Q, Chang C, Tao P, Ning Z, Rong S, Liu Y, et al. Waste heat recovery in an oscillating heat pipe using interfacial electrical double layers. *Appl Phys Lett* 2018;112. <https://doi.org/10.1063/1.5033347>.
- [36] Zabek D, Taylor J, Ayel V, Bertin Y, Romestant C, Bowen CR. A novel pyroelectric generator utilising naturally driven temperature fluctuations from oscillating heat pipes for waste heat recovery and thermal energy harvesting. *J Appl Phys* 2016;120:024505. <https://doi.org/10.1063/1.4958338>.
- [37] Zhang Y, Faghri A. Advances and unsolved issues in pulsating heat pipes. *Heat Transf Eng* 2008;29:20–44. <https://doi.org/10.1080/01457630701677114>.
- [38] Nikolayev VS. Physical principles and state-of-the-art of modeling of the pulsating heat pipe: A review. *Appl Therm Eng* 2021;195:117111.

<https://doi.org/10.1016/j.applthermaleng.2021.117111>.

- [39] Zhang Y, Faghri A. Heat transfer in a pulsating heat pipe with open end. *Int J Heat Mass Transf* 2001;45:755–64. [https://doi.org/10.1016/S0017-9310\(01\)00203-4](https://doi.org/10.1016/S0017-9310(01)00203-4).
- [40] Rao M, Lefèvre F, Khandekar S, Bonjour J. Heat and mass transfer mechanisms of a self-sustained thermally driven oscillating liquid-vapour meniscus. *Int J Heat Mass Transf* 2015;86:519–30. <https://doi.org/10.1016/j.ijheatmasstransfer.2015.03.015>.
- [41] Rao M, Lefèvre F, Khandekar S, Bonjour J. Understanding transport mechanism of a self-sustained thermally driven oscillating two-phase system in a capillary tube. *Int J Heat Mass Transf* 2013;65:451–9. <https://doi.org/10.1016/j.ijheatmasstransfer.2013.05.067>.
- [42] Rao M, Lefèvre F, Czujko PC, Khandekar S, Bonjour J. Numerical and experimental investigations of thermally induced oscillating flow inside a capillary tube. *Int J Therm Sci* 2017;115:29–42. <https://doi.org/10.1016/j.ijthermalsci.2017.01.009>.
- [43] Das SP, Nikolayev VS, Lefevre F, Pottier B, Khandekar S, Bonjour J. Thermally induced two-phase oscillating flow inside a capillary tube. *Int J Heat Mass Transf* 2010;53:3905–13. <https://doi.org/10.1016/j.ijheatmasstransfer.2010.05.009>.
- [44] Fourgeaud L, Nikolayev VS, Ercolani E, Duplat J, Gully P. In situ investigation of liquid films in pulsating heat pipe. *Appl Therm Eng* 2017;126:1023–8. <https://doi.org/10.1016/j.applthermaleng.2017.01.064>.
- [45] Tessier-Poirier A. Comprendre les auto-oscillations dans le caloduc pulsé mono-branche. Université de Sherbrooke, 2022.
- [46] Ma H. *Oscillating heat pipes*. Springer New York; 2015. <https://doi.org/10.1007/978-1-4939-2504-9/COVER>.
- [47] Ma HB, Hanlon MA, Chen CL. An investigation of oscillating motions in a miniature pulsating heat pipe. *Microfluid Nanofluidics* 2006;2:171–9. <https://doi.org/10.1007/S10404-005-0061-8/FIGURES/10>.
- [48] Tessier-Poirier A, Monin T, Léveillé É, Monfray S, Formosa F, Fréchette LG. How evaporation and condensation lead to self-oscillations in the single-branch pulsating heat pipe. *Phys Rev Fluids* 2019;4:103901. <https://doi.org/10.1103/PhysRevFluids.4.103901>.
- [49] Zuo ZJ, North MT, Ray L. Combined Pulsating and Capillary Heat Pipe Mechanism for Cooling of High Heat Flux Electronics. *ASME Int Mech Eng Congr Expo Proc* 2021;1999-R:237–43. <https://doi.org/10.1115/IMECE1999-1124>.
- [50] Dobson RT. Theoretical and experimental modelling of an open oscillatory heat pipe including gravity. *Int J Therm Sci* 2004;43:113–9. <https://doi.org/10.1016/j.ijthermalsci.2003.05.003>.
- [51] Dobson RT. An open oscillatory heat pipe water pump. *Appl Therm Eng* 2005;25:603–21. <https://doi.org/10.1016/j.applthermaleng.2004.07.005>.
- [52] Das SP, Nikolayev VS, Lefevre F, Pottier B, Khandekar S, Bonjour J. Thermally induced two-phase oscillating flow inside a capillary tube. *Int J Heat Mass Transf* 2010;53:3905–13. <https://doi.org/10.1016/j.ijheatmasstransfer.2010.05.009>.

- [53] Nikolayev VS. Oscillatory instability of the gas-liquid meniscus in a capillary under the imposed temperature difference. *Int J Heat Mass Transf* 2013;64:313–21. <https://doi.org/10.1016/j.ijheatmasstransfer.2013.04.043>.
- [54] Nikolayev VS. Effect of tube heat conduction on the single branch pulsating heat pipe start-up. *Int J Heat Mass Transf* 2016;95:477–87. <https://doi.org/10.1016/j.ijheatmasstransfer.2015.12.016>.
- [55] Nikolayev VS, Marengo M. Pulsating Heat Pipes: Basics of Functioning and Modeling. In: Thome JR, editor. *Encycl. Two-Phase Heat Transf. Flow IV*, World Scientific Publishing Company; 2018, p. 63–139. [https://doi.org/10.1142/9789813234406\\_0002](https://doi.org/10.1142/9789813234406_0002).
- [56] White F. *Viscous Fluid Flow*. 3rd ed. Mc Graw Hill; 2006.
- [57] Ma HB, Hanlon MA, Chen CL. An investigation of oscillating motions in a miniature pulsating heat pipe. *Microfluid Nanofluidics* 2006;2:171–9. <https://doi.org/10.1007/s10404-005-0061-8>.
- [58] Monin T, Tessier-Poirier A, Léveillé É, Juneau-Fecteau A, Formosa F, Monfray S, et al. Validation expérimental du comportement d’un caloduc élémentaire décrit comme un résonateur excité par la thermique.”. CIFQ , Sherbrooke, 2015.
- [59] Tessier-Poirier A, Rand RH, Fréchette LG. What limits the oscillations’ amplitude in the single-branch pulsating heat pipe. *Nonlinear Dyn* 2022;108:27–59. <https://doi.org/10.1007/S11071-021-07188-3/FIGURES/14>.
- [60] Bretherton FP. The motion of long bubbles in tubes. *J Fluid Mech* 1961;10:166–88. <https://doi.org/10.1017/S0022112061000160>.
- [61] Landau L, Levich B. Dragging of a Liquid by a Moving Plate. *Dyn Curved Front* 1988:141–53. <https://doi.org/10.1016/B978-0-08-092523-3.50016-2>.
- [62] Nikkhah A, Karami N, Tessier-Poirier A, Abouali O, Fréchette LG. CFD Modelling Of Film Deposition from a Receding Meniscus in a Capillary Tube Using the Approach of Overset Grid Technique. *Proc. 9th Int. Conf. Fluid Flow, Heat Mass Transf., Niagara Falls, Canada: 2022*. <https://doi.org/10.11159/ffhmt22.211>.
- [63] Plawsky JL, Fedorov AG, Garimella S V, Ma HB, Maroo SC, Chen L, et al. Nano- and Microstructures for Thin-Film Evaporation—A Review. *Nanoscale Microscale Thermophys Eng* 2014;18:251–69. <https://doi.org/10.1080/15567265.2013.878419>.
- [64] Ibrahim K, Abd Rabbo MF, Gambaryan-Roisman T, Stephan P. Experimental investigation of evaporative heat transfer characteristics at the 3-phase contact line. *Exp Therm Fluid Sci* 2010;34:1036–41. <https://doi.org/https://doi.org/10.1016/j.expthermflusci.2010.02.014>.
- [65] Sefiane K, Ward CA. Recent advances on thermocapillary flows and interfacial conditions during the evaporation of liquids. *Adv Colloid Interface Sci* 2007;134–135:201–23. <https://doi.org/https://doi.org/10.1016/j.cis.2007.04.020>.
- [66] Migliaccio CP, Dhavaleswarapu HK, Garimella S V. Temperature measurements near the contact line of an evaporating meniscus V-groove. *Int J Heat Mass Transf*

2011;54:1520–6.

<https://doi.org/https://doi.org/10.1016/j.ijheatmasstransfer.2010.11.040>.

- [67] Yan C, Ma HB. Analytical Solutions of Heat Transfer and Film Thickness in Thin-Film Evaporation. *J Heat Transfer* 2013;135:31501–6. <https://doi.org/http://dx.doi.org/10.1115/1.4007856>.
- [68] Dhavaleswarapu HK, Murthy JY, Garimella S V. Numerical investigation of an evaporating meniscus in a channel. *Int J Heat Mass Transf* 2012;55:915–24. <https://doi.org/https://doi.org/10.1016/j.ijheatmasstransfer.2011.10.017>.
- [69] Nagayama G, Kawagoe M, Tokunaga A, Tsuruta T. On the evaporation rate of ultra-thin liquid film at the nanostructured surface: A molecular dynamics study. *Int J Therm Sci* 2010;49:59–66. <https://doi.org/https://doi.org/10.1016/j.ijthermalsci.2009.06.001>.
- [70] de Menezes Atayde C, Doi I. Highly stable hydrophilic surfaces of PDMS thin layer obtained by UV radiation and oxygen plasma treatments. *Phys Status Solidi C* 2010;7:189–92. <https://doi.org/10.1002/pssc.200982419>.
- [71] Plawsky JL, Fedorov AG, Garimella S V, Ma HB, Maroo SC, Chen L, et al. Nano-and microstructures for thin-film evaporation-A review. *Nanoscale Microscale Thermophys Eng* 2014;18:251–69. <https://doi.org/10.1080/15567265.2013.878419>.
- [72] Kim H-Y, Kang BH. Effects of hydrophilic surface treatment on evaporation heat transfer at the outside wall of horizontal tubes. *Appl Therm Eng* 2003;23:449–58. [https://doi.org/https://doi.org/10.1016/S1359-4311\(02\)00211-9](https://doi.org/https://doi.org/10.1016/S1359-4311(02)00211-9).
- [73] Leu T-S, Wu C-H. Experimental studies of surface modified oscillating heat pipes. *Heat Mass Transf* 2017;53:3329–40. <https://doi.org/10.1007/s00231-017-2051-2>.
- [74] Plawsky JL, Ojha M, Chatterjee A, Jr PCW. Review of the Effects of Surface Topography , Surface Chemistry , and Fluid Physics on Evaporation at the Contact Line. *Chem Eng Commun* 2008;196:658–696. <https://doi.org/10.1080/00986440802569679>.
- [75] Bigham S, Fazeli A, Moghaddam S. Physics of microstructures enhancement of thin film evaporation heat transfer in microchannels flow boiling. *Sci Rep* 2017;7:1–11. <https://doi.org/10.1038/srep44745>.
- [76] Liu W, Li Y, Cai Y, Sekulic DP. Capillary Rise of Liquids over a Microstructured Solid Surface. *Langmuir* 2011;27:14260–6. <https://doi.org/10.1021/la2033884>.
- [77] Xiao R, Wang EN. Microengineered surfaces for thin film evaporation for enhanced heat dissipation. *ASME Int. Mech. Eng. Congr. Expo. Proc.*, vol. 9, American Society of Mechanical Engineers (ASME); 2010, p. 1463–7. <https://doi.org/10.1115/IMECE2009-13033>.
- [78] Xiao R, Chu K-H, Wang EN. High-Flux Thin Film Evaporation on Nanostructured Surfaces. *14th Int. Heat Transf. Conf.*, 2010, p. 853–60. <https://doi.org/https://doi.org/10.1115/IHTC14-22905>.
- [79] Farokhnia N, Irajizad P, Sajadi SM, Ghasemi H. Rational Micro/Nanostructuring for Thin-Film Evaporation. *J Phys Chem C* 2016;120:8742–50.

<https://doi.org/10.1021/acs.jpcc.6b01362>.

- [80] Bico J, Quéré D. Rise of liquids and bubbles in angular capillary tubes. *J Colloid Interface Sci* 2002;247:162–6. <https://doi.org/10.1006/jcis.2001.8106>.
- [81] Chauvet F, Duru P, Prat M. Depinning of evaporating liquid films in square capillary tubes: Influence of corners' roundedness. *Phys Fluids* 2010;22. <https://doi.org/10.1063/1.3503925>.
- [82] Qu J, Li X, Wang Q, Liu F, Guo H. Heat transfer characteristics of micro-grooved oscillating heat pipes. *Exp Therm Fluid Sci* 2017;85:75–84. <https://doi.org/10.1016/J.EXPTHERMFLUSCI.2017.02.022>.
- [83] Krambeck L, Domiciano KG, Betancur-Arboleda LA, Mantelli MBH. Novel flat plate pulsating heat pipe with ultra sharp grooves. *Appl Therm Eng* 2022;211:118509. <https://doi.org/10.1016/j.applthermaleng.2022.118509>.
- [84] Mitcheson PD, Yeatman EM, Rao GK, Holmes AS, Green TC. Energy Harvesting From Human and Machine Motion for Wireless Electronic Devices. *Proc IEEE* 2008;96:1457–86. <https://doi.org/10.1109/JPROC.2008.927494>.
- [85] Li WJ, Ho TCH, Chan GMH, Leong PHW, Wong HY. Infrared signal transmission by a laser-micromachined, vibration-induced power generator. *Proc. 43rd IEEE Midwest Symp. Circuits Syst.*, vol. 1, 2000, p. 236–9. <https://doi.org/10.1109/MWSCAS.2000.951628>.
- [86] Glynne-Jones P, Tudor MJ, Beeby SP, White NM. An electromagnetic, vibration-powered generator for intelligent sensor systems. *Sensors Actuators A Phys* 2004;110:344–9. <https://doi.org/https://doi.org/10.1016/j.sna.2003.09.045>.
- [87] El-hami M, Glynne-Jones P, White NM, Hill M, Beeby S, James E, et al. Design and fabrication of a new vibration-based electromechanical power generator. *Sensors Actuators A Phys* 2001;92:335–42. [https://doi.org/https://doi.org/10.1016/S0924-4247\(01\)00569-6](https://doi.org/https://doi.org/10.1016/S0924-4247(01)00569-6).
- [88] Lee JMH, Yuen SCL, Li WJ, Leong PHW. Development of an AA size energy transducer with micro resonators. *Proc. 2003 Int. Symp. Circuits Syst. 2003. ISCAS '03.*, vol. 4, 2003, p. IV–IV. <https://doi.org/10.1109/ISCAS.2003.1206360>.
- [89] Beeby SP, Tudor MJ, Torah RN, Koukharenko E, Roberts S, O'Donnell T, et al. Macro and micro scale electromagnetic kinetic energy harvesting generators. *DTIP MEMS MOEMS*, Stresa, Italy: 2006. <https://doi.org/https://doi.org/10.48550/arXiv.0711.3314>.
- [90] Tashiro R, Kabei N, Katayama K, Ishizuka Y, Tsuboi F, Tsuchiya K. Development of an Electrostatic Generator that Harnesses the Motion of a Living Body : Use of a Resonant Phenomenon. *JSME Int J Ser C* 2000;43:916–22. <https://doi.org/10.1299/jsmec.43.916>.
- [91] Despesse G, Chaillout JJ, Jager T, Léger JM, Vassilev A, Basrou S, et al. High damping electrostatic system for vibration energy scavenging. *Proc. 2005 Jt. Conf. Smart objects Ambient Intell.*, Grenoble: 2005. <https://doi.org/http://doi.acm.org/10.1145/1107548.1107617>.

- [92] Mitcheson P, Holmes A, Yeatman E, Green T, Miao P. Micro-Machined Variable Capacitors for Power Generation. *Electrost Inst Phys Conf Ser* 2003;178:53–8. <https://doi.org/10.1201/9781420034387.ch8>.
- [93] Jean-Mistral C, Basrour S, Chaillout J-J. Comparison of electroactive polymers for energy scavenging applications. *Smart Mater Struct* 2010;19:085012. <https://doi.org/10.1088/0964-1726/19/8/085012>.
- [94] H.W. Jackson. *Introduction to Electric Circuits*. Prentice-Hall; 1959.
- [95] Mitcheson PD, Green TC, Yeatman EM, Holmes AS. Architectures for Vibration-Driven Micropower Generators. *J Microelectromechanical Syst* 2004;13:429–40. <https://doi.org/10.1109/JMEMS.2004.830151>.
- [96] Alioto M. *Enabling the Internet of Things From Integrated Circuits to Integrated Systems*. Springer; 2016. <https://doi.org/10.1007/978-3-319-51482-6>.
- [97] Roundy S, Steingart D, Frechette L, Wright P, Rabaey J. Power Sources for Wireless Sensor Networks. *Lect Notes Comput Sci (Including Subser Lect Notes Artif Intell Lect Notes Bioinformatics)* 2004;2920:1–17. [https://doi.org/10.1007/978-3-540-24606-0\\_1](https://doi.org/10.1007/978-3-540-24606-0_1).
- [98] Francoeur M. *Thermal Fundamentals. Micro Energy Harvest.*, Wiley; 2015, p. 61–84. <https://doi.org/10.1002/9783527672943.ch4>.
- [99] Léveillé É, Mirshekari G, Monfray S, Skotnicki T, Fréchet LG. A microfluidic heat engine based on explosive evaporation. *PowerMEMS*, Atlanta, GA, USA,; 2012.
- [100] Gully P, Bonnet F, Nikolayev VS, Luchier N, Tran TQ. Evaluation of the Vapor Thermodynamic State in PHP. *17th Int. heat Pipe Conf.*, Kanpur, India: 2013. <https://doi.org/10.1615/heatpipescitech.v5.i1-4.410>.
- [101] Noh HY, Kim SJ. Numerical simulation of pulsating heat pipes: Parametric investigation and thermal optimization. *Energy Convers Manag* 2020;v 203. <https://doi.org/10.1016/j.enconman.2019.112237>.
- [102] Bae J, Lee SY, Kim SJ. Numerical investigation of effect of film dynamics on fluid motion and thermal performance in pulsating heat pipes. *Energy Convers Manag* 2017;v 151:p 296-310. <https://doi.org/10.1016/j.enconman.2017.08.086>.
- [103] Jo J, Kim J, Kim SJ. Experimental investigations of heat transfer mechanisms of a pulsating heat pipe. *Energy Convers Manag* 2019;v 181:p 331-341. <https://doi.org/10.1016/j.enconman.2018.12.027>.
- [104] Yoon A, Kim SJ. Experimental and theoretical studies on oscillation frequencies of liquid slugs in micro pulsating heat pipes. *Energy Convers Manag* 2019;v 181:p 48-58. <https://doi.org/10.1016/j.enconman.2018.11.060>.
- [105] Monin T, Tessier-Poirier A, Léveillé E, Juneau-Fecteau A, Skotnicki T, Formosa F, et al. First experimental demonstration of a Self-Oscillating Fluidic Heat Engine (SOFHE) with piezoelectric power generation. *J Phys Conf Ser* 2016;773:12039. <https://doi.org/10.1088/1742-6596/773/1/012039>.
- [106] Monin T, Tessier-Poirier A, Amnache A, Skotnicki T, Monfray S, Formosa F, et al.

- Demonstration of a microfabricated self-oscillating fluidic heat engine (SOFHE). 2018 Solid-State Sensors, Actuators Microsystems Work Hilt Head 2018 2018:368–9. <https://doi.org/10.31438/trf.hh2018.104>.
- [107] Das SP, Nikolayev VS, Lefevre F, Pottier B, Khandekar S, Bonjour J. Thermally induced two-phase oscillating flow inside a capillary tube 2010;53:3905–13. <https://doi.org/10.1016/j.ijheatmasstransfer.2010.05.009>.
- [108] Spinato G, Borhani N, Thome JR. Understanding the self-sustained oscillating two-phase flow motion in a closed loop pulsating heat pipe. *Energy* 2015;90:889–99. <https://doi.org/10.1016/j.energy.2015.07.119>.
- [109] Karami N, Tessier-Poirier A, Léveillé E, Monin T, Formosa F, Fréchette L. Thermodynamic Cycle of a Self-Oscillating Fluidic Heat Engine (SOFHE) for Thermal Energy Harvesting. *Int. Symp. Oscil. Heat Pipes (ISOPHP 2019 )* Daejeon, Korea, n.d.
- [110] Hao T, Ma X, Lan Z. Effects of Hydrophilic and Hydrophobic Surfaces on Start-Up Performance of an Oscillating Heat Pipe. *J Heat Transfer* 2018;140. <https://doi.org/10.1115/1.4037341>.
- [111] Nikkhah A, Tessier-Poirier A, Karami N, Abouali O, Frechette LG. Investigation of the Liquid Plug Friction Force in the Self-Oscillating Fluidic Heat Engine (SOFHE), *Institute of Electrical and Electronics Engineers (IEEE)*; 2020, p. 1–7. <https://doi.org/10.1109/powermems49317.2019.92321106939>.
- [112] Tessier-poirier A, Karami N, Rand RH, Frechette LG. Harvesting energy with the Self-Oscillating-Fluidic-Heat-Engine ( SOFHE ) - Basic principles. *Under Publ Process* n.d.
- [113] Alhuyi Nazari M, Ahmadi MH, Ghasempour R, Shafii MB, Mahian O, Kalogirou S, et al. A review on pulsating heat pipes: From solar to cryogenic applications. *Appl Energy* 2018;222:475–84. <https://doi.org/10.1016/j.apenergy.2018.04.020>.
- [114] Bastakoti D, Zhang H, Li D, Cai W, Li F. An overview on the developing trend of pulsating heat pipe and its performance. *Appl Therm Eng* 2018;141:305–32. <https://doi.org/10.1016/J.APPLTHERMALENG.2018.05.121>.
- [115] Karami N, Tessier-Poirier A, Nikkhah A, Léveillé E, Monin T, Formosa F, et al. Experimental characterization of the thermodynamic cycle of a self-oscillating fluidic heat engine (SOFHE) for thermal energy harvesting. *Energy Convers Manag* 2022;258:115548. <https://doi.org/10.1016/J.ENCONMAN.2022.115548>.
- [116] Karami N, Tessier-Poirier A, Nikkhah A, Leveille E, Amnache A, Frechette LG. Microfabricated Self-Oscillating Fluidic Heat Engine (SOFHE) With Enhanced Phase Change Through Corner Capillaries. *21st Int. Conf. Micro Nanotechnol. Power Gener. Energy Convers. Appl. PowerMEMS, IEEE*; 2022, p. 117–20. <https://doi.org/10.1109/PowerMEMS56853.2022.10007564>.
- [117] Zwier MP, Gerner HJ van, Wits WW. Modelling and experimental investigation of a thermally driven self-oscillating pump. *Appl Therm Eng* 2017;v 126:1126–33. <https://doi.org/10.1016/j.applthermaleng.2017.02.063>.
- [118] Zhang Y, Faghri A. Heat transfer in a pulsating heat pipe with open end. *Int J Heat Mass*

- Transf 2001;45:755–64. [https://doi.org/10.1016/S0017-9310\(01\)00203-4](https://doi.org/10.1016/S0017-9310(01)00203-4).
- [119] Zhang Y, Faghri A, Shafii MB. Analysis of liquid-vapor pulsating flow in a U-shaped miniature tube. *Int J Heat Mass Transf* 2002;45:2501–8. [https://doi.org/10.1016/S0017-9310\(01\)00348-9](https://doi.org/10.1016/S0017-9310(01)00348-9).
- [120] Karami N, Tessier-Poirier A, Nikkhah A, Leveille E, Frechette LG. Time-Resolved Measurement of Enhanced Phase Change by a Fiber in an Oscillating Two-Phase Plug Flow. *28th Int Work Therm Investig ICs Syst* 2022:1–5. <https://doi.org/10.1109/THERMINIC57263.2022.9950692>.
- [121] Jun S, Kim SJ. Experimental study on a criterion for normal operation of pulsating heat pipes in a horizontal orientation. *Int J Heat Mass Transf* 2019;137:1064–75. <https://doi.org/10.1016/j.ijheatmasstransfer.2019.03.163>.
- [122] Tessier-Poirier A, Rand RH, Fréchet LG. What limits the oscillations' amplitude in the single-branch pulsating heat pipe. *Nonlinear Dyn* 2022;108:27–59. <https://doi.org/10.1007/s11071-021-07188-3>.
- [123] Kim W, Kim SJ. Effect of reentrant cavities on the thermal performance of a pulsating heat pipe. *Appl Therm Eng* 2018;133:61–9. <https://doi.org/10.1016/J.APPLTHERMALENG.2018.01.027>.
- [124] Rao M. Thermo-hydrodynamics of an extended meniscus as unit-cell approach of pulsating heat pipe. INSA de Lyon, 2015. <https://doi.org/https://tel.archives-ouvertes.fr/tel-01247470>.
- [125] Qu J, Wu H, Cheng P. Start-up, heat transfer and flow characteristics of silicon-based micro pulsating heat pipes. *Int J Heat Mass Transf* 2012;55:6109–20. <https://doi.org/10.1016/j.ijheatmasstransfer.2012.06.024>.
- [126] Patel VM, Gaurav, Mehta HB. Influence of working fluids on startup mechanism and thermal performance of a closed loop pulsating heat pipe. *Appl Therm Eng* 2017;110:1568–77. <https://doi.org/10.1016/J.APPLTHERMALENG.2016.09.017>.
- [127] Qu W, Ma HB. Theoretical analysis of startup of a pulsating heat pipe. *Int J Heat Mass Transf* 2007;50:2309–16. <https://doi.org/10.1016/j.ijheatmasstransfer.2006.10.043>.
- [128] Dobson, R.T., Harms TM. Lumped parameter analysis of closed and open oscillatory heat pipes. *Proc. 11th Int. Heat Pipe Conf., Tokyo, Japan: 1999*, p. 137±142.
- [129] Karami N, Tessier-Poirier A, Léveillé E, Fréchet LG. Importance of phase change timing in a self-sustained oscillatory flow. *Int J Heat Mass Transf* 2023;213:124327. <https://doi.org/10.1016/j.ijheatmasstransfer.2023.124327>.
- [130] Epstein AH. Millimeter-Scale, Micro-Electro-Mechanical Systems Gas Turbine Engines. *J Eng Gas Turbines Power* 2004;126:205. <https://doi.org/10.1115/1.1739245>.
- [131] Kolliopoulos P, Jochem KS, Johnson D, Suszynski WJ, Francis LF, Kumar S. Capillary-flow dynamics in open rectangular microchannels. *J Fluid Mech* 2021;911:A32. <https://doi.org/10.1017/JFM.2020.986>.
- [132] Washburn E. The dynamics of capillary flow. *Phys Rev* 1921;17:273–83.

<https://doi.org/https://doi.org/10.1103/PhysRev.17.273>.

[133] White FM. Fluid Mechanics. 8th ed. McGraw Hill; 2016.

[134] Spreemann D, Manoli Y. Electromagnetic Vibration Energy Harvesting Devices. vol. 35. Dordrecht: Springer Netherlands; 2012. <https://doi.org/10.1007/978-94-007-2944-5>.